

Investigation of the effect of chitin
nanowhiskers distribution on structural and
physical properties of high impact
polypropylene/chitin nanocomposites

by

Alicia Nel



*Thesis presented in partial fulfilment of the requirements for
the degree of Master of Science in the Faculty of Science at
Stellenbosch University*

Department of Chemistry and Polymer Science,
Stellenbosch University,
Private Bag X1, Matieland 7602, South Africa.

Supervisor: Dr. Marietjie Lutz

December 2014

Acknowledgments

I thank God for all the strength He gave me to stay positive and keep on going through disappointments and stressful situations to come out on the other side and finally reach my goals. I also thank my friends and colleagues for all their advice and help during my studies. Thank you for making this experience a fun and memorable one.

I give thanks to my promoter and study leader, Dr Marietjie Lutz, for her support, financially and academically. I appreciate all your help and advice and it was an honor working with you and learning from you.

Many thanks to my parents. Without them none of this would have been possible. I appreciate all your sacrifices and the love you show me.

I would also like to thank the following people, for their contributions:

1. The Olefins research group.
2. Madeleine Frazenburg (SEM and TEM analysis, Geology Department).
3. Divann Robertson for helping me with all the heavy lifting and dirty work.
4. Prof Albert Van Reenen for giving me great advice.
5. Dr M. Brand (for her electronic assistance).
6. Technical Assistants and Financial Staff at the Polymer Science Division.
7. Bursary funding from the NRF.
8. Roediger Agencies (Thank you Illana for TGA analysis and Andy for allowing me access to tensile testing.)
9. Dr. M. J. Hurndall (student liaison officer).
10. Shaheen Daniels for his assistance in the lab while I was finishing writing this thesis.
11. Dewald Botes for his constant support and patience.

Declaration

"I, the undersigned, hereby declare that the work contained in this thesis is my own original work unless indicated otherwise."

Signature:

A. Nel

Date:

Copyright © 2014 Stellenbosch University
All rights reserved

Abstract

Polymer composites have been gaining more importance in our daily lives because of the favorable properties that can be provided by these types of material. A polymer composite consists of improved properties when compared to the individual polymers that it is compiled of. The reason that composites are better than the individual polymers is mainly because composites are a combination of all the beneficial properties from the individual materials that was used to make the polymer composite.

High impact polypropylene (HiPP) is a complex copolymer that was developed to overcome the restrictions of polypropylene (PP). Although PP have excellent properties at lower temperatures, it loses these advantages at elevated temperatures. High impact polypropylene has a much better impact strength and is processable at high temperatures. High impact polypropylene has been studied in depth for its applications and its superior properties such as an improved impact strength. The tensile properties, after the incorporation of a nanofiller, have however not been investigated to our knowledge. Nanofillers have reinforcing abilities due to the nano-scale diameters. Particles that have sizes on a nanometer range are mostly devoid of defects. Nanofillers that are biopolymers have additional advantages such that can consist of antimicrobial abilities, renewability, biocompatibility and biodegradability. Composites reinforced with chitin nanowhiskers (chnw) have shown to have valuable applications in the latest medical, industrial and environmental developments.

Different loadings of chnw were incorporated into a HiPP matrix in order to investigate the effects that this nanofiller will have on the tensile properties of HiPP. There were two challenges that required attention during the incorporation of chnw into HiPP. The first major challenge was the poor interaction that exist between chnw and HiPP due to the hydrophobic nature of the HiPP matrix and the hydrophilic nature of chnw. The second problem was the agglomeration that can occur because of the hydrogen bonding between the chnw that is caused by the structure of the chnw chains. In order to gain the best dispersion of chnw within the HiPP matrix it was necessary to use compatibilizers and different methods of incorporation. The two types of compatibilizers that were chosen to improve the compatibility between the HiPP matrix and chnw were polypropylene-*graft*-maleic anhydride (PPgMA) and poly(ethylene-*co*-vinyl alcohol)(EVOH). Injection molding is typically used to process HiPP and was chosen as one of the methods for

incorporating chnw into the HiPP matrix. A second method of incorporation was used specifically for the nanocomposites containing EVOH known as electrospinning combined with meltpressing.

Tensile testing, DSC, TGA and FTIR were used to investigate the changes in the mechanical and thermal properties of the nanocomposites. SEM and TEM were employed to investigate the morphology of the electrospun fiber mats and to characterize the chnw. FTIR as well as TGA were used to characterize the chitin nanowhiskers and to identify the individual components within the nanocomposites after incorporation took place. The incorporation of chnw along with the compatibilizer did show improvement in some mechanical properties of the polymer matrix. However, the influence that each type of compatibilizer had on this effect varied depending on the content of the chnw and compatibilizer with regards to the polymer matrix.

Contents

Acknowledgments	i
Declaration	ii
Abstract	iii
List of Figures	vii
List of Tables	xii
Nomenclature	xiii
1 Introduction and Objectives	1
1.1 Introduction	1
1.2 Objectives	3
1.3 Methodology	3
References	4
2 Theoretical Background	6
2.1 Polypropylene	6
2.2 Chitin	7
2.3 Compatibilizer	13
2.4 Nanocomposites	16
2.5 Electrospinning	18
2.6 Characterization of isolated nanowhiskers and nanocomposites	24
References	27
3 Experimental	35
3.1 Materials	35
3.2 Preparation of chitin nanowhiskers	35
3.3 Preparation of HiPP/chnw composites with PPgMA as compatibilizer . . .	36
3.4 Preparation of HiPP/chnw composites with EVOH as compatibilizer . . .	36

<i>CONTENTS</i>	vi
3.5 Injection molding	37
3.6 Hydraulic melt pressing	38
3.7 Methods of characterization	38
References	41
4 Characterization of chitin nanowhiskers	42
4.1 Transmission electron microscopy	42
4.2 Fourier transform infrared analysis	43
4.3 Thermogravimetric analysis	43
4.4 Conclusion	45
References	46
5 Results for HiPP/chnw nanocomposites with PPgMA as compatibilizer	47
5.1 Fluorescence microscopy analysis	47
5.2 Attenuated total reflectance-fourier transform infrared spectroscopy (ATR- FTIR)	49
5.3 Differential scanning calorimetry analysis (DSC)	56
5.4 Thermogravimetric analysis (TGA)	62
5.5 Tensile testing	66
5.6 Conclusion	76
References	77
6 Results for HiPP/chnw nanocomposites with EVOH as compatibilizer	78
6.1 Solvent casting and injection molding	78
6.2 Electrospinning and melt-pressing	101
6.3 Conclusion	111
References	113
7 Conclusions and Recommendations for Future Work	115
7.1 Conclusion	115
7.2 Future work	116
A FTIR data	117
A.1 FTIR spectra of nanocomposites containing EVOH as compatibilizer . . .	117
B DSC Data	120
B.1 DSC results for HiPP/chnw nanocomposites with PPgMA as compatibilizer	120
C SEM images of nanocomposites	124

List of Figures

2.1	Formation of HiPP [11].	7
2.2	Molecular structure of chitin [14].	9
2.3	Chemical structure of chitin (The dotted line indicates hydrogen bonding) [18].	9
2.4	Arrangements of various types of chitin chains.	9
2.5	FTIR spectrum of (a) α -chitin and (b) β -chitin [14].	10
2.6	TEM images of isolated chitin nanowhiskers from(a) squid pen and (b) crab shells [49].	13
2.7	Conversion of EVA to EVOH [14].	13
2.8	Molecular structure of polypropylene- <i>graft</i> -maleic anhydride where a) indicates the polypropylene portion and b) maleic anhydride [71].	15
2.9	Various types of interaction between the layered silicate and polymer chain [75].	17
2.10	Photograph of a meniscus of Polyvinyl Alcohol in aqueous solution showing a fiber drawn from a Taylor Cone by the process of electrospinning [82].	19
2.11	Diagram showing the mechanism of electrospinning [83].	20
2.12	Ball spinning method showing upward electrospinning fibers [84].	20
2.13	Horizontal electrospinning set up [14].	21
2.14	Fiber beading can be avoided by adjusting one or more of the electrospinning parameters as seen above when the voltage was adjusted from a)-10_20kV to b)-5_10kV.	22
2.15	Nanocomposite consisting of EVOH-chnw elctrospun fibers sandwiched between two LDPE films.	23
2.16	TEM image of chnw.	24
4.1	TEM images of chitin nanowhiskers a) redispersed after freeze drying and b) sampled directly from a dialysis tube.	42
4.2	FTIR of pure chnw	43
4.3	TGA curves of chitin nanowhiskers.	44
5.1	Confocal microscope images of nanocomposites containing a) 3 wt% chnw and 6 wt% PPgMA (Frame 1) b) 3 wt% chnw and 6 wt% PPgMA (Frame 2) and c) 8 wt% chnw and 6 wt% PPgMA (Frame 1) d) 8 wt% chnw and 6 wt% PPgMA (Frame 2)	48

5.2	FTIR spectra of clean components.	49
5.3	FTIR spectra of nanocomposite without compatibilizer.	50
5.4	FTIR spectra of nanocomposites consisting of the HiPP matrix, 2 wt% PPgMA and varying chnw loadings.	51
5.5	FTIR spectra of nanocomposites consisting of the HiPP matrix, 4 wt% PPgMA and varying chnw loadings.	52
5.6	FTIR spectra of nanocomposites consisting of the HiPP matrix, 6 wt% PPgMA and varying chnw loadings.	53
5.7	FTIR spectra of nanocomposites consisting of the HiPP matrix, 8 wt% PPgMA and varying chnw loadings.	54
5.8	FTIR spectra of nanocomposites consisting of the HiPP matrix, 10 wt% PPgMA and varying chnw loadings.	55
5.9	DSC thermograms showing the effect that various wt% PPgMA and 3 wt% chnw have on the HiPP matrix.	58
5.10	DSC thermograms showing the effect that various wt% PPgMA and 5 wt% chnw have on the HiPP matrix.	59
5.11	DSC thermograms showing the effect that various wt% PPgMA and 8 wt% chnw have on the HiPP matrix.	60
5.12	DSC thermograms showing the effect that various wt% PPgMA and 10 wt% chnw have on the HiPP matrix.	61
5.13	TGA curves of the individual components used in the preparation of the nanocomposites.	62
5.14	TGA curves overlayed to show the change in onset and maximum temperature during incorporation of various chnw loadings with 2 wt% PPgMA into HiPP matrix compared with neat samples of HiPP, chnw and PPgMA.	63
5.15	TGA curves overlayed to show the change in onset and maximum temperature during incorporation of various chnw loadings with 4 wt% PPgMA into HiPP matrix compared with neat samples of HiPP, chnw and PPgMA.	63
5.16	TGA curves overlayed to show the change in onset and maximum temperature during incorporation of various chnw loadings with 6 wt% PPgMA into HiPP matrix compared with neat samples of HiPP, chnw and PPgMA.	64
5.17	TGA curves overlayed to show the change in onset and maximum temperature during incorporation of various chnw loadings with 8 wt% PPgMA into HiPP matrix compared with neat samples of HiPP, chnw and PPgMA.	65
5.18	TGA curves overlayed to show the change in onset and maximum temperature during incorporation of various chnw loadings with 10 wt% PPgMA into HiPP matrix compared with neat samples of HiPP, chnw and PPgMA.	65
5.19	Stress-strain curves showing composites containing no chnw and only HiPP and PPgMA	67

5.20	Stress-strain curves showing composites containing no compatibilizer and only HiPP and chnw	68
5.21	Stress-strain curves showing 3% chnw combined with varying PPgMA content within HiPP nanocomposites	68
5.22	Stress-strain curves showing 5% chnw combined with varying PPgMA content within HiPP nanocomposites	69
5.23	Stress-strain curves showing 8% chnw combined with varying PPgMA content within HiPP nanocomposites	70
5.24	Stress-strain curves showing 10% chnw combined with varying PPgMA content within HiPP nanocomposites	70
5.25	Stress-strain curves showing various concentrations of chnw combined with 2% PPgMA within HiPP nanocomposites	71
5.26	Stress-strain curves showing various concentrations of chnw combined with 4% PPgMA within HiPP nanocomposites	72
5.27	Stress-strain curves showing various concentrations of chnw combined with 6% PPgMA within HiPP nanocomposites	72
5.28	Stress-strain curves showing various concentrations of chnw combined with 8% PPgMA within HiPP nanocomposites	73
5.29	Stress-strain curves showing various concentrations of chnw combined with 10% PPgMA within HiPP nanocomposites	73
6.1	FTIR spectra of clean components.	79
6.2	FTIR spectra of nanocomposite without compatibilizer.	80
6.3	FTIR spectra of nanocomposites consisting of the HiPP matrix, 2 wt% EVOH and varying chnw loadings.	81
6.4	FTIR spectra of nanocomposites consisting of the HiPP matrix, 4 wt% EVOH and varying chnw loadings.	82
6.5	FTIR spectra of nanocomposites consisting of the HiPP matrix, 6 wt% EVOH and varying chnw loadings.	83
6.6	FTIR spectra of nanocomposites consisting of the HiPP matrix, 8 wt% EVOH and varying chnw loadings.	84
6.7	FTIR spectra of nanocomposites consisting of the HiPP matrix, 10 wt% EVOH and varying chnw loadings.	85
6.8	TGA curves of individual components used in the preparation of the nanocomposites.	86
6.9	TGA curves overlayed to show the change in onset and maximum temperature during incorporation of various chnw loadings with 2 wt% EVOH into HiPP matrix compared with neat samples of HiPP, chnw and EVOH.	87

6.10	TGA curves overlayed to show the change in onset and maximum temperature during incorporation of various chnw loadings with 4 wt% EVOH into HiPP matrix compared with neat samples of HiPP, chnw and EVOH	87
6.11	TGA curves overlayed to show the change in onset and maximum temperature during incorporation of various chnw loadings with 6 wt% EVOH into HiPP matrix compared with neat samples of HiPP, chnw and EVOH	88
6.12	TGA curves overlayed to show the change in onset and maximum temperature during incorporation of various chnw loadings with 8 wt% EVOH into HiPP matrix compared with neat samples of HiPP, chnw and EVOH	89
6.13	TGA curves overlayed to show the change in onset and maximum temperature during incorporation of various chnw loadings with 10 wt% EVOH into HiPP matrix compared with neat samples of HiPP, chnw and EVOH	90
6.14	DSC curves showing the effect that various wt% EVOH and 3 wt% chnw have on the HiPP matrix.	92
6.15	DSC curves showing the effect that various wt% EVOH and 5 wt% chnw have on the HiPP matrix.	92
6.16	DSC curves showing the effect that various wt% EVOH and 8 wt% chnw have on the HiPP matrix.	93
6.17	DSC curves showing the effect that various wt% EVOH and 10 wt% chnw have on the HiPP matrix.	93
6.18	Stress-strain curves showing composites containing no compatibilizer and only HiPP and chnw	94
6.19	Stress-strain curves of 3 wt% chnw with varying EVOH content	95
6.20	Stress-strain curves of 5 wt% chnw with varying EVOH content	95
6.21	Stress-strain curves of 8 wt% chnw with varying EVOH content	96
6.22	Stress-strain curves of 10 wt% chnw with varying EVOH content	96
6.23	Stress-strain curves of 2 wt% EVOH with varying chnw content	97
6.24	Stress-strain curves of 4 wt% EVOH with varying chnw content	97
6.25	Stress-strain curves of 6 wt% EVOH with varying chnw content	98
6.26	Stress-strain curves of 8 wt% EVOH with varying chnw content	98
6.27	Stress-strain curves of 10 wt% EVOH with varying chnw content	99
6.28	SEM images of chnw_EVOH electrospun fiber mats containing (a) clean 5% EVOH, (b) 3% chnw_5% EVOH, (c) 5% chnw_5% EVOH, (d) 8% chnw_5% EVOH and (e) 10% chnw_2% EVOH	101
6.29	SEM images of electrospun fiber mat consisting of 3 wt% chnw and 5 wt% EVOH in HiPP.	103
6.30	FTIR of EVOH/chnw electrospun fiber mats.	104
6.31	FTIR of EVOH/chnw electrospun fiber mats melt pressed into a HiPP matrix.	105
6.32	TGA overlay of electrospun chnw/EVOH fiber mats.	106

6.33	TGA overlay of electrospun chnw/EVOH fiber mats that were sandwiched between two HiPP films and meltpressed.	107
6.34	DSC thermograms of chnw/EVOH electrospun fibers.	109
6.35	DSC thermograms of chnw/EVOH electrospun fibers meltpressed into a HiPP matrix.	110
6.36	Tensile overlay of electrospun chnw_EVOH fiber mats that were sandwiched between two HiPP films and then melt-pressed.	110
A.1	FTIR spectra of 3 wt% chnw and varying EVOH.	117
A.2	FTIR spectra of 5 wt% chnw and varying EVOH.	118
A.3	FTIR spectra of 8 wt% chnw and varying EVOH.	118
A.4	FTIR spectra of 10 wt% chnw and varying EVOH.	119
B.1	DSC thermograms showing the effect that 10 wt% PPgMA and various wt% chnw have on the HiPP matrix.	121
B.2	DSC thermograms showing the effect that 8 wt% PPgMA and various wt% chnw have on the HiPP matrix.	122
B.3	DSC thermograms showing the effect that 6 wt% PPgMA and various wt% chnw have on the HiPP matrix.	122
B.4	DSC thermograms showing the effect that 4 wt% PPgMA and various wt% chnw have on the HiPP matrix.	123
B.5	DSC thermograms showing the effect that 2 wt% PPgMA and various wt% chnw have on the HiPP matrix.	123
C.1	SEM images of 5 wt% chnw and 5 wt% EVOH indicating the layers of HiPP with electrospun chnw_EVOH fiber mat.	124
C.2	SEM images of 8 wt% chnw and 5 wt % EVOH in HiPP.	125
C.3	SEM images of 10 wt% chnw and 2 wt% EVOH in HiPP.	125

List of Tables

2.1	List of chitin nanowhisker sources [41].	12
2.2	Parameters that effect electrospinning.	22
3.1	Electrospinning conditions.	37
5.1	Melting points (°C) of HiPP/chnw (PPgMA) nanocomposites where 0 wt% chnw and 0 wt% PPgMA indicates clean HiPP.	57
5.2	Percentage crystallization (%) of HiPP/chnw (PPgMA) nanocomposites where 0 wt% chnw and 0 wt% PPgMA indicates clean HiPP.	57
5.3	TGA onset degradation temperature and weight loss percentage of nanocomposites with various chnw loadings and 2 wt% PPgMA.	66
5.4	TGA onset degradation temperature and weight loss percentage of nanocomposites with various chnw loadings and 10 wt% PPgMA.	66
5.5	Tensile testing data of clean sample HiPP as well as HiPP containing chnw with no compatibilizer	74
5.6	Tensile testing data of 2 wt% PPgMA with various wt% chnw in HiPP matrix	75
5.7	Tensile testing data of 10 wt% PPgMA with various wt% chnw in HiPP matrix	75
6.1	Melting points (°C) of HiPP/chnw (EVOH) nanocomposites where 0 wt% chnw and 0 wt% EVOH indicates clean HiPP	91
6.2	Percentage crystallization (%) of HiPP/chnw (EVOH) nanocomposites where 0 wt% chnw and 0 wt% EVOH indicates clean HiPP	91
6.3	Tensile testing data of clean sample HiPP as well as HiPP containing chnw with no compatibilizer	99
6.4	Tensile testing data of 2 wt% EVOH with various wt% chnw in HiPP matrix .	100
6.5	Tensile testing data of 10 wt% EVOH with various wt% chnw in HiPP matrix	100
6.6	DSC data of electrospun fibers consisting of EVOH and chnw	108
6.7	DSC data of nanocomposite consisting of electrospun EVOH, chnw and HiPP	109
6.8	Tensile testing data of electrospun chnw_EVOH in HiPP	111

Nomenclature

Abbreviations

ATR-FTIR	Attenuated total reflectance-Fourier transform infrared
chnw	Chitin nanowhiskers
DMSO	Dimethyl sulfoxide
DSC	Differential scanning calorimetry
EPR	Ethylene-propylene rubber
EVA	Parent ethylene- <i>co</i> -vinyl acetate polymer
EVOH	Poly(ethylene- <i>co</i> -vinyl alcohol)
FITC	Fluorescein isothiocyanate
HiPP	High impact polypropylene
iPP	Isotactic polypropylene
IR	Infrared
LSM	Laser scanning microscope
MAH	Maleic anhydride
MFI	Melt flow index
NaOH	Sodium hydroxide
PE	Polyethylene
PP	Polypropylene
PPgMA	Polypropylene- <i>graft</i> -maleic anhydride
PVOH	Poly vinyl-alcohol
rpm	Rotation per minute
SEM	Scanning electron microscope
TEM	Transmission electron microscope
TGA	Thermal gravimetric analysis
wt%	Weight percentage

Chapter 1

Introduction and Objectives

1.1 Introduction

Polymer composites are very important in our daily lives and can be found in household appliances, medical equipment as well as construction and building materials. Polymer composites consist of a polymer matrix and a filler material. One of the biggest advantages of polymer composites is that the beneficial properties of both polymers are combined in order to have enhancing effects on the composites compared to the pure polymer and filler material when used separately.

Polymer composites that consist of a thermoplastic such as HiPP and biopolymer nanofillers such as chitin nanowhiskers (chnw) show great promise because of the possible benefits of combining the advantageous properties of each individual polymer within one composite. Research concerning these types of composites have been published by Madeleine Du Toit [1]. The study done by Du Toit investigates the effects caused by incorporating polysaccharide nanocrystals into a poly (ethylene-*co*-vinyl alcohol) matrix. Other studies published by Nair and Dufresne [2, 3, 4] consist of a series of investigations regarding chnw reinforced natural rubber nanocomposites and in a separate investigation Sriupayo *et al.* [5] also studied chnw as a filler within nanocomposite films. Combining a polysaccharide with a thermoplastic have become the main focus in many studies.

In this study high impact polypropylene (HiPP) was used as polymer matrix. There has been an annual increase of 10% in the production of HiPP which is a good indication of the growing popularity of this copolymer within the industry and research fields [6]. The importance it has acquired can be ascribed to the excellent thermal properties and high impact strength possessed by HiPP. High impact polypropylene is a copolymer that consists of a crystalline isotactic polypropylene (iPP) matrix, a rubber component (EPR) and a range of ethylene-propylene copolymers [7]. This semi-crystalline copolymer has enhanced mechanical properties compared to the homopolymer, polypropylene, and is

most commonly used to manufacture automotive parts [8, 9, 10]. The thermal properties of HiPP is excellent and this thermoplastic can easily be melted down and re-used. High impact polypropylene is easily processable due to its thermal stability but it is not just subjected to injection molding processes. In studies done by P. Edward [11] another process was investigated where it was possible to mold HiPP into films. This process created opportunities for HiPP to be used for other types of applications such as film packaging and biomedical applications [11].

Polysaccharides, specifically chitin, have recently been studied with increasing interest by a number of polymer science researchers because of the positive attributes that these biopolymers possess. Chitin is a renewable, biodegradable and abundant polymer that can be utilized from the shells of arthropods like crabs, shrimps and beetles [12]. Chitin also has zero toxicity and is compatible with biological materials such as human tissue. This polysaccharide also has antibacterial abilities and can absorb and retain moisture which makes it ideal for wound healing treatment applications [13]. Chitin can undergo acid hydrolysis in a water suspension and yield highly crystalline nanocrystals that are commonly known as chitin nanowhiskers (chnw) [14, 15, 16]. These nanocrystals have nano-scale diameters and lengths which means that chnw are mostly devoid of defects unlike chitin [12]. These qualities and all the properties mentioned above make chnw a very good reinforcing agent. The increased crystallinity of chnw enhances the mechanical properties of this nanofiller significantly.

The effect that chnw can have on the mechanical properties within a thermoplastic is of great interest. The beneficial properties of chnw and HiPP can be combined into one composite that exhibits excellent thermal stability and also possesses antimicrobial properties. This can be very advantageous for application in the packaging industry and biomedical field where antimicrobial properties become necessary.

There are some challenges that arise when working with chnw. The small diameters of these nanocrystals cause them to agglomerate. Therefore, in solution, one must always ensure that they are well dispersed by using methods like ultra-sonication. The hydrophilic nature of chnw also hinders compatibility with a hydrophobic polymer such as HiPP. This complication can possibly be overcome by addition of an appropriate compatibilizer. This allows the chnw and the HiPP matrix to interact better without chemically modifying chnw in order to improve the compatibility between the filler and its matrix.

Compounds such as poly(ethylene-*co*-vinyl alcohol) (EVOH) and poly(propylene-*graft*-maleic anhydride) (PPgMA) are often used as compatibilizers between hydrophobic and hydrophilic matrices. Both these compatibilizers were tested for their effectiveness in enhancing the interaction between chnw and HiPP in this research study project. This

study furthermore investigated various methods of incorporating chnw along with the compatibilizer into the HiPP matrix in order to find the most adequate way possible that will ensure good dispersion and maximum interaction.

1.2 Objectives

The objective for this study was to investigate the effect that chnw as reinforcement have on the mechanical and thermal properties of the HiPP matrix in a HiPP/chnw nanocomposite. For this purpose two different compatibilizers and various methods for incorporating chnw into HiPP were investigated. Solution casting and injection molding was the first processing method that was investigated and PPgMA and EVOH were used separately as compatibilizers during the incorporation of chnw into HiPP. Electrospinning and melt pressing were the second processing method that was investigated where the electrospun fibers consisting of EVOH and chnw were melt pressed into films in between two HiPP films. The results of this study will be valuable to the knowledge of chnw as fillers in thermoplastic polymers and the effect on the properties of the nanocomposite.

1.3 Methodology

1. Synthesis and characterization of chnw.
2. Incorporation of chnw into HiPP matrix using PPgMA.
3. Incorporation of chnw into HiPP matrix via electrospinning, using EVOH, and then melt pressing these fiber mats between two HiPP films.
4. Analysis of thermal, mechanical and morphologies of the nanocomposite.

References

- [1] M. Du Toit, "Incorporation of polysaccharide nanowhiskers into a poly (ethylene-co-vinyl alcohol) matrix," p. 1, 2013.
- [2] K. Nair and A. Dufresne, "Crabshell chitin whisker reinforced natural rubber nanocomposites, 1. processing and swelling behavior," *Biomacromolecules*, vol. 4(3), pp. 657–665, 2003.
- [3] A. Dufresne and K. Nair, "Crabshell chitin whisker reinforced natural rubber nanocomposites, 2. mechanical behavior," *Biomacromolecules*, vol. 4(3), pp. 666–674, 2003.
- [4] A. Morin and A. Dufresne, "Nanocomposites of chitin nanowhiskers from rifting tubes and poly(caprolactone)," *Macromolecules*, vol. 35(6), pp. 2190–2199, 2002.
- [5] J. Sriupayo, P. Supaphol, J. Blackwell, and R. Rujiravanit, "Preparation and characterization of α -chitin whiskers-reinforced chitosan nanocomposite films with or without heat treatment," *Carbohydrate Polymers*, vol. 62(2), pp. 130–136, 2005.
- [6] I. Urdampilleta, A. Gonzalez, J. Iruin, J. De La Cal, and J. Asua, "Morphology of high impact polypropylene particles." *Macromolecules*, 2005.
- [7] N. Basson, "The effect of molecular architecture on the properties of propylene impact copolymers." *University of Stellenbosch*, pp. 13–23, 2010.
- [8] C. Zhang, Y. Shangguan, R. Chen, and Q. Zheng, "Study on thermal behaviour of impact polypropylene copolymer and its fractions," *Journal of Applied Polymer Science*, vol. 119, p. 1560, 2011.
- [9] H. Cheng and M. Kakugo, "¹³C nmr analysis of compositional heterogeneity in ethylene-propylene copolymers," *Macromolecules*, p. 1724, 1991.
- [10] A. Van Reenen and N. Basson, "Molecular composition and properties of impact polypropylene copolymers," *eXPRESS Polymer Letters*, vol. 6(5), p. 427, 2012.
- [11] P. Edward, "Polypropylene handbook," *Hanser Publishers, Munich*, p. 12, 1996.

- [12] M. Mincea, A. Negrulescu, and V. Ostafe, "Preparation, modification, and applications of chitin nanowhiskers: a review," *Review on Advanced Material Science*, vol. 30, pp. 225–242, 2012.
- [13] A. Mera, J. Araki, T. Ohtsuki, M. Shimosaka, and N. Yoshida, *Biotechnol Biomaterial*, vol. 1, 2011.
- [14] M. Ravi Kumar, "Reactive and functional polymers," *Biotechnol Biomaterial*, vol. 46, p. 1, 2000.
- [15] P. Visakh and S. Thomas, *Waste Biomass Valor*, vol. 1, p. 121, 2010.
- [16] M. Rinaudo, *Progress in Polymer Science*, 2006.

Chapter 2

Theoretical Background

2.1 Polypropylene

Polypropylene (PP) is the most promising thermoplastic of all thermoplastics for the synthesis of composites using biofibers and nanoparticles. It has been substantially used in an array of applications including carpet backing, face yarn and construction fabrics, self-hinging packages, appliance parts, medical equipment, automobile parts, films, bottles and containers [1].

There are three types of stereo conformations for PP, known as isotactic, atactic and syndiotactic. Isotactic PP has CH_3 groups on the same side of the polymer chain backbone while syndiotactic PP have alternating CH_3 groups on each side of the backbone. Atactic PP does not have any particular order of CH_3 arrangement on the polymer backbone and is completely random [2]. Isotactic polypropylene (iPP) is rigid with thermal and chemical resistance. At low temperatures iPP unfortunately possesses mediocre impact strength which therefore restricts its usefulness.

Isotactic polypropylene can be mechanically improved by incorporating an elastomer or ethylene copolymer [3, 4]. Sequential multistage polymerization appears to be the best method to improve upon the mechanical properties of iPP. This process is used to incorporate ethylene-propylene rubber (EPR) into iPP. Homopolymerization propylene takes place in the first stage. In the second stage the copolymerization occurs where the above mentioned copolymer is incorporated into the PP matrix [5, 6]. The end product of this process is high impact polypropylene (HiPP).

2.1.1 High impact polypropylene

This copolymer is very complex. High impact polypropylene consists of finely distributed poly(ethylene-co-propylene) elastomeric copolymer within a iPP matrix. As mentioned before, the formation of HiPP occurs within a sequential multistage polymerization pro-

cess. The first reactor contains the iPP and this is where the morphology of forming iPP receives the main focus [7]. In the second reactor the confinement and dispersion of EPR is important within the iPP matrix. This is very important because it directly affects the impact properties of HiPP [8].

It had been proposed that as the EPR content is increased, it create stress under the layer of PP-homopolymer during the process occurring in the second reactor and then flow through the cracks into the micro and macro pores and onto the surface of the polymer particle [9, 4]. The formation of HiPP is illustrated in Figure 2.1 [10].

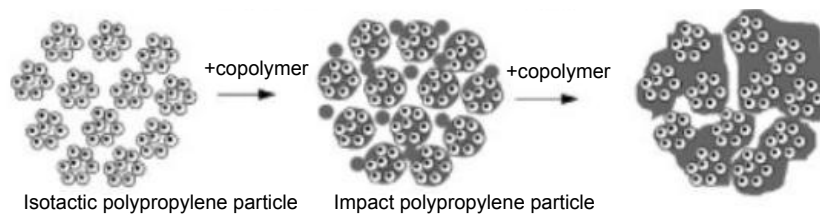


Figure 2.1: Formation of HiPP [11].

High impact polypropylene has improved impact strength at low temperatures and has improved toughness [2]. The rubber phase is strengthened because of the polyethylene crystals in the EPR phase and this helps to inhibit the formation of voids in the rubber phase during stretching of the polymer. High impact polypropylene is very versatile in applications due to its unique properties.

High impact polypropylene is not limited to injection molding processing only; it can also undergo an air-quenched bubble process known as calendaring that can form HiPP into films [2]. This makes it possible to use HiPP for packaging, biohazard bags, diaper backing films, industrial bags, roof sheeting, geomembranes, medical tubing and bags, and car bumpers [2]. High impact polypropylene is an embellished asset commonly used for parts in automobiles because it can be easily injection molded due to its high thermal stability.

2.2 Chitin

Research increased with regards to the production of nanocomposites containing natural polymers like chitin and cellulose. These materials are polysaccharides and exist naturally and abundantly in the world. Polysaccharides are favorable candidates for the synthesis of nanocomposites because they introduce additional functionalities like biodegradability, biocompatibility and renewability [12]. In spite of the presence of nitrogen for polysaccharides such as chitin and chitosan, immunogenicity and toxicity is very low [13]. Polysac-

charides can therefore be accepted into the tissue or cells of a living organism without inducing a humoral or cell mediated immune response.

The physiochemical properties of chitin are very agreeable. It is a highly crystalline, natural polymer that has antimicrobial properties and birefringence [14]. Chitin and cellulose share similar qualities but there are some aspects where these two types of polysaccharides differ. The processing step for nanowhisker production from cellulose is much more complex than that of chitin. Hydro sulphuric acid is used in the acid hydrolysis step instead of hydrochloric acid, as is used for chitin, which can create complications during analysis work. Hydro sulphuric acid is difficult to get rid off and can cause degradation or interfere with the interactions within the nanocomposite [14]. Chitin also possesses natural antimicrobial properties that can not be found in cellulose without additional modification. Chitin is capable of acting as an individual reinforcing phase or as an uninterrupted matrix phase for dispersing one or more secondary phase(s). Chitin can behave as a true matrix by controlling the nucleation and growth of secondary phases that are polymeric, ceramic or metallic in composition [12].

A French scientist, Henri Braconnet, was the first to isolate chitin from mushrooms in 1811. Odier also found that the same substance could be found in the cuticles of insects in 1823. Chitin became the most abundant natural polymer after cellulose on earth. Chitin can be found in arthropods, particularly in their exoskeletons and, as found by Braconnet, in the cell wall of fungi [12].

The molecular structure of chitin can be seen in Figure 2.2. The structure contains 2-acetamido-2-deoxy- β -D-glucose [12, 15]. Chitin is a linear polymer with a $\beta - 1, 4$ -linked N-acetylglucosamine. The fundamental units of chitin are bound by glycosidic bonds. Chitin has low reactivity because of the highly ordered hydrogen bonding occurring between the chains as can be seen in Figure 2.3. The poor solubility is caused by the rigid structure due to the hydrogen bonding. Poor swelling behavior and processing characteristics are also displayed and are also accredited to the hydrogen bonds within the chemical structure of chitin. Chemical modification of chitin have been found to improve the solubility in general organic solvents as seen in studies done by Kurita et al. [16] and Inoue et al. [17].

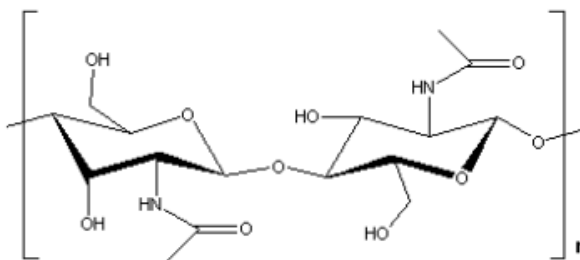


Figure 2.2: Molecular structure of chitin [14].

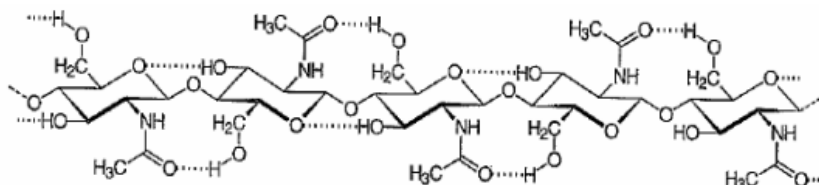


Figure 2.3: Chemical structure of chitin (The dotted line indicates hydrogen bonding) [18].

Three types of polymorphic forms of chitin exist known as α -chitin, β -chitin, γ -chitin. The crystal structure of each varies due to the varying polarities of the adjacent chains in successive sheets and the layering or packing of these same sheets [12]. Chitin is highly basic, unlike most other natural polysaccharides. The natural abundant polymorphic form is α -chitin with an antiparallel configuration. The α -chitin has a highly ordered crystalline structure and strong hydrogen bonding between its chains due to the anti-parallel arrangements. This makes chitin a very rigid and insoluble compound. The β -chitin has a parallel configuration while the γ -chitin has a random configuration varying between anti-parallel and parallel. The arrangement for α -, β - and γ -chitin can be seen in Figure 2.4.

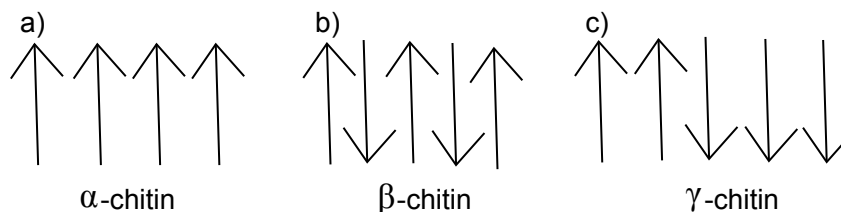


Figure 2.4: Arrangements of various types of chitin chains.

Chitin is usually characterized using NMR, FTIR, X-ray diffraction and crystallography. As illustrated in the IR-spectra presented in Figure 2.5 the characteristic amide moiety causing the C=O stretching region between 1600cm^{-1} and 1500cm^{-1} for the two types of crystal structures (α - and β -chitin) is distinguishable [19].

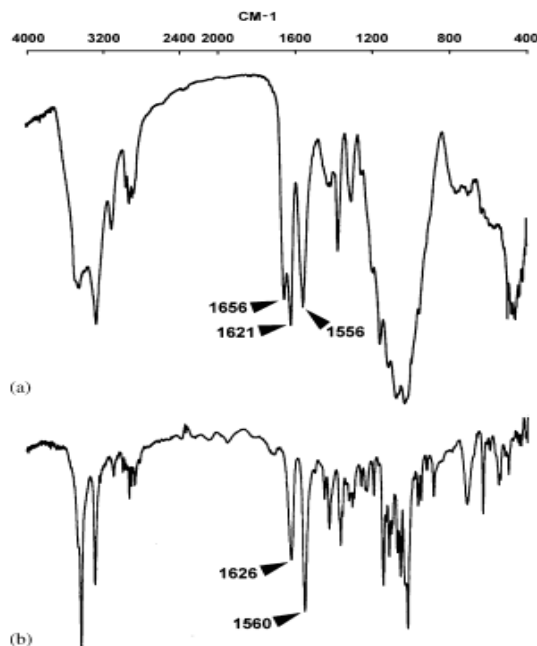


Figure 2.5: FTIR spectrum of (a) α -chitin and (b) β -chitin [14].

Chitin can act as a useful chelating agent due to its high nitrogen content (6.89%) [15]. It has been shown that polysaccharides can be used to help purify and remove toxic metals and organic compounds from water in studies done by Gregorio Crini [20]. Besides being a good separation material for water purification, chitin has also been found useful in cosmetics [20].

Production of chitin and some of its derivatives like chitosan are mostly from crab and shrimp shells that are discarded as waste by canning industries at sites in Oregon, Washington, Virginia, Japan and also by fishing fleets in the Antarctic. Countries such as India, Japan, Poland, Norway and Australia began producing chitin and chitosan commercially because of the useful carotenoids such as astaxanthin that serves as a food additive in aquaculture e.g. salmon [12, 15].

Other applications for which chitin have been found effective is regulating photosynthesis of maize and soy beans [12]. It can also act as a component in anti-cancer drugs, and in other biomedical applications such as dental restoration, drug delivery systems and also structural constituent in synthetic organs [12]. Chitin also found uses in composite reinforcement due to its good mechanical properties as mentioned earlier.

2.2.1 Chitin nanowhiskers

Chitin nanowhiskers (chnw) can be extracted from chitin using a variety of techniques such as acid hydrolysis [21, 22, 23, 24, 25, 26, 27], TEMPO-mediated oxidation [28, 29, 30], ultrasonication [31], electrospinning [32], mechanical treatment [33, 34, 35] and gelation [36].

Chitin nanowhiskers have been used as a reinforcing component in many studies [14, 37, 38]. It has been found to improve the mechanical properties of a soy protein nanocomposite and also decreased its water sensitivity [37]. It has already been mentioned in section 1.1 that chnw have some extremely beneficial properties that can contribute the tensile properties of a polymer matrix. The highly crystalline structure of chnw allows it to be very strong and have a high modulus. The tiny diameters of chnw also cause it to be almost completely free of defects. Chitin nanowhiskers are easy to chemically modify, light in weight, have a high surface area and aspect ratio. Chitin nanowhiskers are also abundant and biodegradable [39, 40].

Acid hydrolysis helps to remove the amorphous regions in the chitin by splitting the glucose bonds. This method is the most popular and was also used in this study. After acid hydrolysis, the suspension is centrifuged, placed in dialysis tubes and dialyzed for 7 to 10 days until it has reached a pH close to 7 (neutral) [21]. The stable colloidal chnw suspension has amino groups that can be protonated yielding a positively charged suspension. This protonation helps to stabilize the watery colloidal dispersions of chnw due to the repulsive forces between the crystallites [41].

The various sources and methods for how chnw can be extracted are presented in Table 2.1. The structural characteristics of chnw differs when extracted from different chitin sources. The lengths and diameters of the chnw tend to vary as well as the aspect ratio because of the varying chitin sources. These two factors are very important when chnw are used as a reinforcing agent. A higher aspect ratio and smaller diameters for chnw results in greater reinforcement properties [41, 42].

Table 2.1: List of chitin nanowhisiker sources [41].

Nr	Chitin Sources	Extraction Method	Structural parameters of nanowhisikers			Ref.
			Length (nm)	Width (nm)	Aspect Ratio	
1	Crab shells	Hydrochloric acid hydrolysis	50-300	6-8	15	[22]
2	Crab shells	Hydrochloric acid hydrolysis	100-600		16	[43]
3	Crab shells	Hydrochloric acid hydrolysis	100-650		10±5	[23]
4	Crab shells	Hydrochloric acid hydrolysis	200-500		15-20	[44]
5	Chitin powder from crab shells	Hydrochloric acid hydrolysis	255±56		8	[45]
6	Crab shells	TEMPO-mediated oxidation and subsequent ultrasonic treatment	340	8		[29]
7	Chitin powder from crab shells	Partial deacetylation with NaOH by fibril surface cationization and subsequent disintegration	250±140	6.2±1.1		[30]
8	Chitin powder from crab shells	Gelation with 1-allyl-3-methylimidazolium bromide followed by regeneration with methanol	Several hundred	20-60		[36]
9	Shrimp shells	Hydrochloric acid hydrolysis	150-800	5-70		[46]
10	Shrimp shells	Hydrochloric acid hydrolysis	231-969	12-65	18	[47]
11	Shrimp shells	Hydrochloric acid hydrolysis	180-820	8-74	10	[24]
12	Shrimp shells	Hydrochloric acid hydrolysis	110-975	8-73	7.5	[29]
13	Squid pen	Hydrochloric acid hydrolysis	50-300	10	15	[25]
14	Squid pen	TEMPO-mediated oxidation	Few microns	3-4		[29]
15	Riftia Tubes	Hydrochloric acid hydrolysis	500-10000	18	120	[48]

Chitin nanowhiskers present some challenges when it comes to regulating good, uniform dispersion and compatibility with a hydrophobic polymer matrix. Solutions to this problem have been investigated and the most popular methods have been found to be chemical modification, or the use of a compatibilizer [40].

Characterization of chnw can be done using AFM, TEM and ATR-FTIR. The characterization of chnw, specifically for chnw extracted from crab shells, will be discussed in Chapter 4. It is important to remember that the crystal structure for chnw differ depending on the source of chitin as seen in the TEM images illustrated in Figure 2.6 [14].

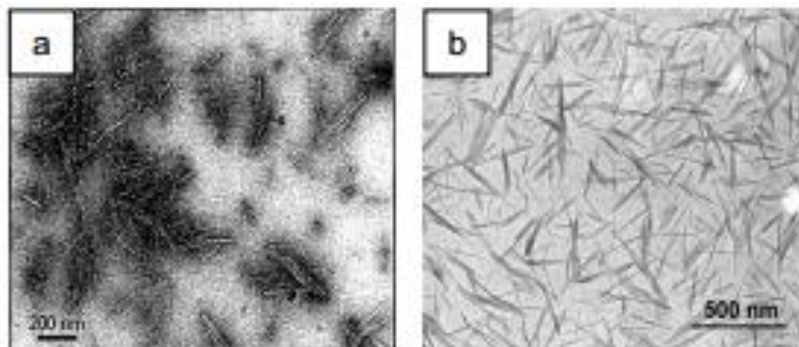


Figure 2.6: TEM images of isolated chitin nanowhiskers from (a) squid pen and (b) crab shells [49].

2.3 Compatibilizer

2.3.1 Poly (ethylene-*co*-vinyl alcohol) (EVOH)

Poly (ethylene-*co*-vinyl alcohol) is an amphoteric polymer which means that it consist of haphazard combinations of hydrophobic ethylene and hydrophilic vinyl alcohol segments. This polymer is produced from a hydrolysis reaction of a parent ethylene-*co*-vinyl acetate polymer (EVA). As shown in Figure 2.7, the acetoxy groups become transformed to a secondary alcohol [50].

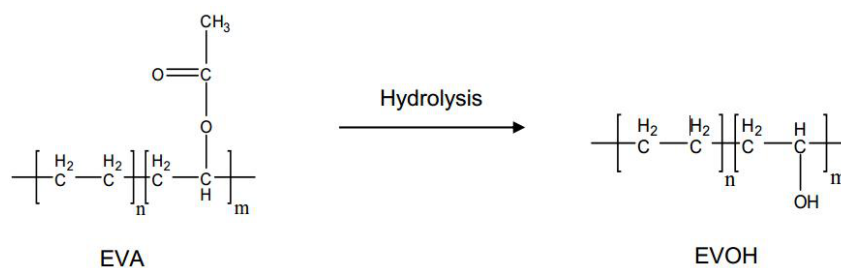


Figure 2.7: Conversion of EVA to EVOH [14].

Poly (ethylene-co-vinyl alcohol) has two types of adaptations used for different applications. The first type is normally used for adhesives where EVOH consists of an ethylene content of 82-90 mole %. The other form of EVOH is where it is completely hydrolyzed from EVA and contains 60-75 mole % vinyl alcohol. This second type of EVOH is commonly used in barrier materials, owing its excellent barrier properties to the vinyl alcohol component [51]. The ethylene content allows the polymer to have good moisture resistance and good mechanical and thermal properties. Other benefits gained from EVOH are its ability to be easily sterilized, its biocompatibility and the fact that it is biologically and chemically resistant [52]. Strong intra- and inter-hydrogen bonding that exist between the alcohol groups can form a barrier for oxygen as well as other gases or organic solvents.

Poly (ethylene-co-vinyl alcohol) is a water sensitive polymer which is one of the drawbacks of this polymer especially in packaging application. When the polymer is exposed to high humidity the water molecules present in the environment can interfere with the hydrogen bonds of the polymer and weaken the interaction between the alcohol groups [53, 54]. Pairing poly (ethylene-co-vinyl alcohol) and nanofillers has been suggested in a number of studies. Clay platelets have been used in PVOH to minimize access of water molecules into the chains of the polymer [55]. Studies have also shown that pairing EVOH with hydrophobic polymers like polypropylene or polyethylene in the form of multi-layered structures can counteract this type of weakness [56, 50].

Poly (ethylene-co-vinyl alcohol) is furthermore used as an adhesive as well as in the packaging industry for its barrier properties. This polymer has also found applicability in the biomedical field. In a study done by Young, T.H *et al.* [57]. Poly (ethylene-co-vinyl alcohol) has been used for neuronal cell culturing proving this polymer very biocompatible. Young *et al.* also studied the culturing of myoblast cells as well as the formation of a uniform bone-like apatite layer using EVOH membranes as a scaffold or substrate. Poly (ethylene-co-vinyl alcohol) can also be used for other types of tissue engineering, drug delivery and wound healing treatments [14, 57].

One of the reasons why EVOH is so effective as a scaffold for cultivating fibroblasts and smooth muscle cells is because it can be easily electrospun into nanofibers [58]. Although EVOH is not as biodegradable as poly(vinyl alcohol) because of the ethylene component, it has many other positive attributes as previously mentioned [59]. One of the most commendable properties of EVOH is the specific interaction it can have with chemical species due to its hydroxyl group which allows surface functionalization. The possibility of modifying EVOH makes this polymer compatible in blends and with fillers or for uses such as drug delivery [60, 61, 62].

2.3.2 Poly propylene-*graft*-maleic anhydride (PPgMA)

Polypropylene-*graft*-maleic anhydride consists of a polypropylene (PP) chain that contains side groups of maleic anhydride [52, 54, 56, 63]. This allows for good compatibility between PPgMA and a polypropylene matrix as well as a filler containing OH-groups. The polypropylene part of PPgMA can interact well with PP and allows compatibility between hydrophilic fillers and a hydrophobic polymer matrix [64]. Polypropylene that is modified with MAH is one of the most important functionalized polyolefins in commercial applications due to the low cost, high activity and good processability [65].

Polypropylene can be treated with maleic anhydride in the presence of peroxide initiators in order to form a chemically modified polymer that possesses improved mechanical and adhesion properties [66]. The maleic anhydride increases degradation of polypropylene because of the presence of peroxide [67]. Grafting of MAH onto PP also influences the melt flow index (MFI) and molecular weight distribution of PP as found by Berzin et al.[67].

Compatibility that improves interaction between a filler and the matrix enhances the strength of composites as found in studies done by Gaucher-Miri *et al.* [68] and more [37, 50, 55, 57, 58, 60, 61, 62, 66, 69, 70]. The mechanical properties namely the tensile strength, impact strength and elongation at break of the composite are all improved when the interaction between filler and matrix is improved.

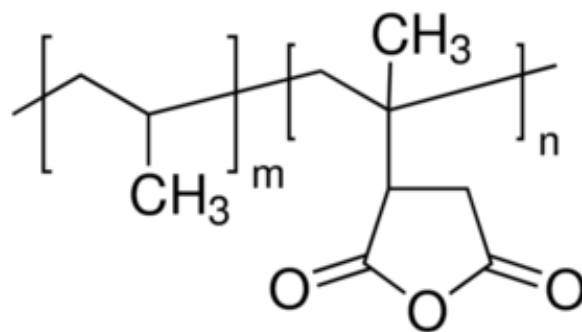


Figure 2.8: Molecular structure of polypropylene-*graft*-maleic anhydride where a) indicates the polypropylene portion and b) maleic anhydride [71].

The polar group, as can be seen in Figure 2.8(b), creates chemical bonds with a substrate like a polar nanofiller. The olefin portion, polypropylene, forms a hair-like structure that intertwines with the bulk of the composite which would be the polymer matrix. The percentage maleic anhydride (MAH) cannot be too high within the PPgMA or else discoloring and foul odor will be a result. The percentage MAH must be chosen at an optimal amount in order to have good mobility and interaction with the nanofiller. The chain lengths

for the polypropylene section of the PPgMA also needs to be an ideal length in order to provide good strength and mechanical entanglement [71].

2.4 Nanocomposites

Richard Feynman was the first to introduce the idea of nanotechnology in 1959. Nanotechnology has been expanded from then on into a wide array of fields within science and technology [72]. Long before this, however, composite materials and nanoparticles have already been in use. In 1907, Bakelite, a fiber reinforced thermoset polymer, was one of the first polymer composites synthesized. Automobile tires were also already strengthened by a composite composed of carbon black nanoparticles and vulcanized rubber [73].

Nanocomposites consist of at least two individual components. One acts as the scaffold or base and the other acts as the reinforcing part. The polymer base surrounds this reinforcing phase and is known as the matrix. The constituents contributing to the reinforcing properties are named a filler [14].

A nanocomposite is only regarded as such when the reinforcing phase is a nanoparticle which means that it needs to be nano-scale and even smaller [38]. Nanocomposites are almost completely free from defects and imperfections due to their small size, especially when compared to macro particles. Nanoparticles can display optical clarity in composites due to the fact that they have shorter wavelengths than that of light and thus do not scatter or bend light [49, 74]. Better interaction is also ensured because of the high surface area. This characteristic in turn also contributes to the reinforcing ability of the nanoparticle within the polymer matrix [72].

Studies by Alexandre *et al.* [75] and Ludeña *et al.* [76] done on separate occasions showed the interaction between silicate-polymer composites. Two types of nanoscale composites may be produced due to the interaction between the layered silicate and the polymer chains. The structure of the interaction of the layered silicate and the polymer chains is illustrated in Figure 2.9. The polymer chain can however ingress into the internal region of the silicate layer, thus resulting in a third type of form that has a multilayer structure with alternating polymer inorganic layers called intercalated composites [75, 76].

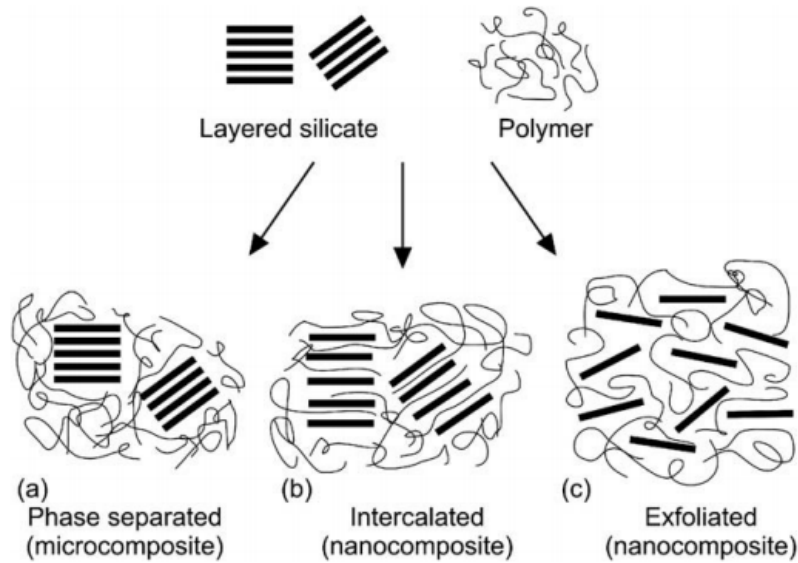


Figure 2.9: Various types of interaction between the layered silicate and polymer chain [75].

The properties of a polymer composite can be improved or deteriorated with the incorporation of nanoparticles. It all depends on how good the interaction is between the filler and the matrix as well as the dispersion of the filler (nanoparticles) within the matrix. The thermal stability and crystallization of the nanoparticles are also two important factors that will influence how the composite will be affected [14].

2.4.1 Nanopolysaccharide composites

Nanopolysaccharides like chitin nanocrystals, also referred to as nanowhiskers due to their spindle shape and whisker-like form, are superior as reinforcing fillers within a matrix. Nanowhiskers provide better reinforcement compared to macro-scale particles. Macro-scale particles contain defects and have a lower aspect ratio than nanowhiskers which is not favorable for the filler-matrix interactions of the nanocomposite. Nanopolysaccharides are very abundant, highly biodegradable, renewable and provides beneficial chemical, electrical and optical properties [72].

It is challenging to achieve uniform dispersion of nanowhiskers in a thermoplastics matrix during incorporation. The nanowhiskers are hydrophilic and tend to agglomerate due to strong intermolecular hydrogen bonding that results in poor dispersion [14]. Good interaction between a matrix and a filler is very important. The amount of stress transferred from the matrix to the filler will depend on the compatibility of the nano-filler and the polymer matrix. Enhanced interaction between the filler and the polymer matrix can be improved, as mentioned earlier, by using an appropriate compatibilizer. This compatibilization is necessary if the polarity of the filler and matrix differ.

The average length found in a study done by Lu *et al.* [23] was 500nm for chitin nanowhiskers (chnw) while the diameter was found to be 50 nm. Lu *et al.* [23] added chnw to soy protein isolate (SPI) thermoplastic. Their studies have shown that the mechanical properties as well as the water resistance of SPI were greatly improved [23].

Sriupayo *et al.* [77] also studied chnw as a filler and incorporated it into chitosan films. Sriupayo discovered that the amount of chnw introduced into the matrix have an effect on the properties of the nanocomposite. The study showed that the tensile strength of chitosan improved until 2.96% chnw content was added. The mechanical properties started to decline when the content of chnw were increased further [77]. Other studies that were done by Fricain *et al.* [78] showed the beneficial properties that polysaccharides can have in a composite for biomedical application such as bone tissue engineering. The study indicated how propitious polysaccharide nanocrystal composites are for the synthesis of bionanocomposites because these nanocrystals are so abundant in nature, rigid and strong with low weight and good biodegradability. Alain Dufresne [38] investigated a new processing method for making polysaccharide nanocrystal composite. The method described by Dufresne included the transformation of polysaccharide nanocrystal composites into a co-continuous material through long chain surface chemical modification. The nanoparticles are subjected to chemical modification with the use of grafting agents bearing a reactive end group and a long compatibilizing tail [38].

Polysaccharides also have polyfunctionality, high chemical reactivity, chirality, chelation and adsorption capacities. These properties were further investigated by Crini *et al.* [20] and the application of polysaccharide-based materials as adsorbents in wastewater treatment were studied. The applications for polysaccharides nanocrystal composites have become vast and keeps growing as new discoveries are made.

2.5 Electrospinning

2.5.1 Introduction

Electrospinning is a technique that provides the formation of fibers with very small dimensions. The useful properties that are gained by using this type of technique are monumental. The technique is very simple and allow for the possibility of large scale production [79].

Electrospinning is useful in fields such as biomedicine. The technique can be used in materials required for filtration, protection, electrical and optical applications. It can also

be used for sensors and also in nanofiber reinforced composites.

Material or composites can be modified via electrospinning assembly thus combining different properties and morphology depending on the type of application it is needed for. Electrospinning is also a good way to enhance dispersion of nanoparticles like chnw within a polymer matrix.

2.5.2 History

In the late 1800's, the process of electrospinning has already become a useful technique since it was first described by William Gilbert in the late 16th century. After interest in nanotechnology took hold in the 1900's, the interest in electrospinning increased even more. It was only patented by Anton Formhals in 1934 after it became commercially popular [80].

Between 1964 and 1969, Sir Geoffrey Ingram Taylor produced a study of electrospinning that modeled the shape of the cone formed by the solution droplet by using mathematics. He also investigated the effect of an electric field particularly on this droplet. This droplet became known as the Taylor cone [81].

2.5.3 Process and setup

A strong electric field is applied to a solution within a needle. The needle acts as an electrode causing deformation in the droplet that forms at the tip of needle. This droplet then ejects after enough disturbance from the tip of the droplet known as the Taylor cone as shown in Figure 2.10. It then propels toward the oppositely charged collector base. The solvent evaporates off during this process and the fibers are collected on the collector. The electrospinning process is presented in Figure 2.11 to give a better indication of what takes place during electrospinning.

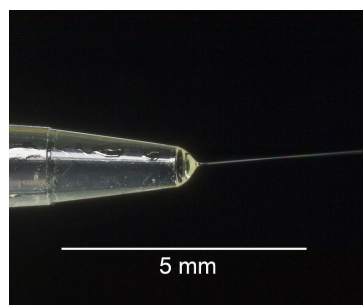


Figure 2.10: Photograph of a meniscus of Polyvinyl Alcohol in aqueous solution showing a fiber drawn from a Taylor Cone by the process of electrospinning [82].

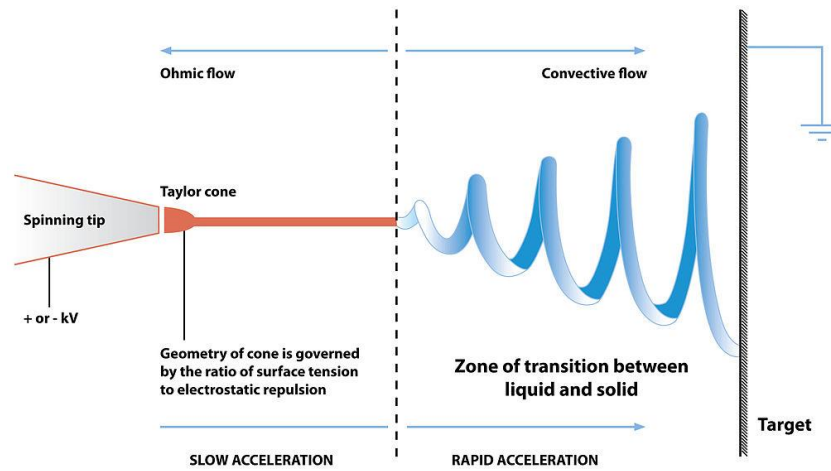


Figure 2.11: Diagram showing the mechanism of electrospinning [83].

Over the years a variety of new and improved types of electrospinning setups have been invented. From 1979 - 2004, needleless electrospinning setups were invented to allow production of nanofibers on a larger industrial scale. Setups, such as ball electrospinning, have also been invented that can allow fibers to be electrospun from multiple points due to the formation of multiple Taylor cones caused by a rotating roller. Instead of a needle a small glass ball, known as a ball spinneret, is placed in the solution and rotated while applying a electrical field as shown in Figure 2.12. The fibers are spun upwards which helps prevent polymer solution from dripping onto the fiber mat that is collected on the collector plate.

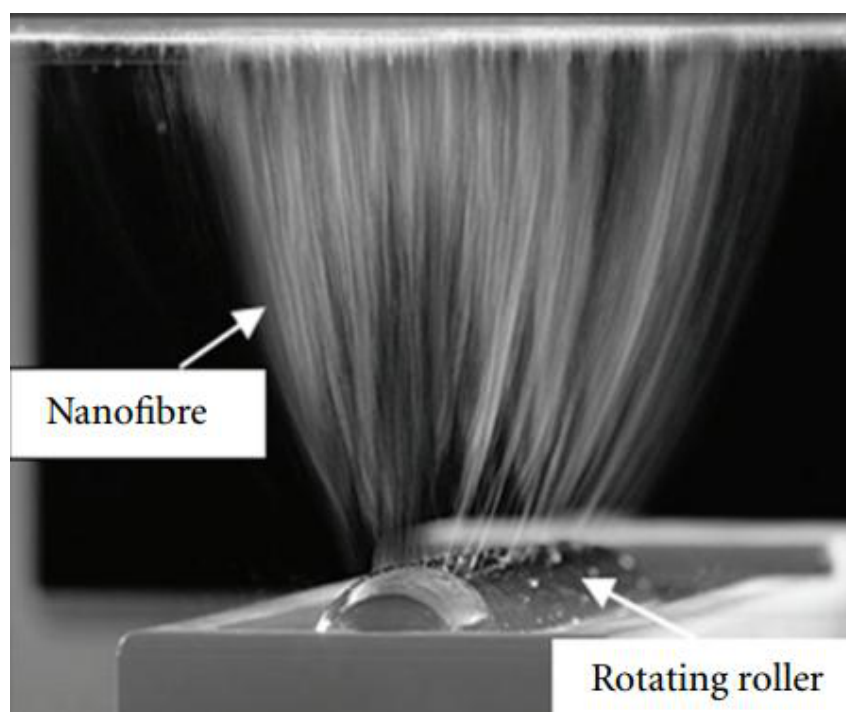


Figure 2.12: Ball spinning method showing upward electrospinning fibers [84].

Multi-needle electrospinning techniques have also been investigated where more than one needle is used in the electrospinning system and each needle nozzle produces a electrospinning jet. A large working environment is required for multi-needle electrospinning so that the strong interferences between adjacent solution jets can be avoided [84]. The multi-needle electrospinning system needs a regular cleaning system for each needle nozzle in order to prevent solution blockage that can occur during the fiber production.

The conventional setup (horizontal or vertical) is still used widely in hundreds of labs all over the world. In this study only the conventional horizontal setup was used and can be seen in Figure 2.13 [14].

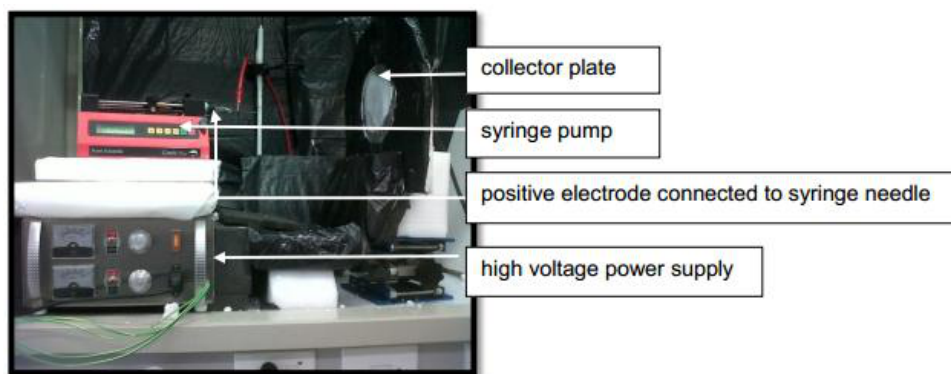


Figure 2.13: Horizontal electrospinning set up [14].

The three main components for a conventional horizontal setup are:

- The high voltage power supply (that can produce an electrical field of 5-50kV) [14].
- The spinneret that contains the electrospinning solution and feeds the solution at controlled flow rate by using a syringe pump.
- A grounded collecting plate with opposite charge to the electrode that is charging the electrospinning solution.

The grounded collecting plate can be stationary or rotate. A rotating collecting plate allows the fibers that are electrospun to be more aligned and uniform [85]. Uniaxially orientated nanofibers can be fabricated by electrospinning onto a rotating cylinder collector [86]. Fibers alignment can improve the mechanical properties of a nanocomposite even further than randomly orientated fibers [14].

2.5.4 Parameter effects

Electrospinning has many factors that can influence the diameter and morphology of nanofibers. The results caused by these factors can clearly be seen in Figure 2.14. The electrospun fiber mat initially had beading that was caused during the electrospinning process. The electromagnetic field that was created during the electrospinning process was too high and caused the electrospinning solution to spatter. The Taylor cone could not form properly before the solution was pulled to the collector base. The lowering of the voltage at the electrodes proved to cause less beading to occur. The morphology and fiber diameter of the nanofibers can therefore be improved by changing one or more of the electrospinning parameters [87].

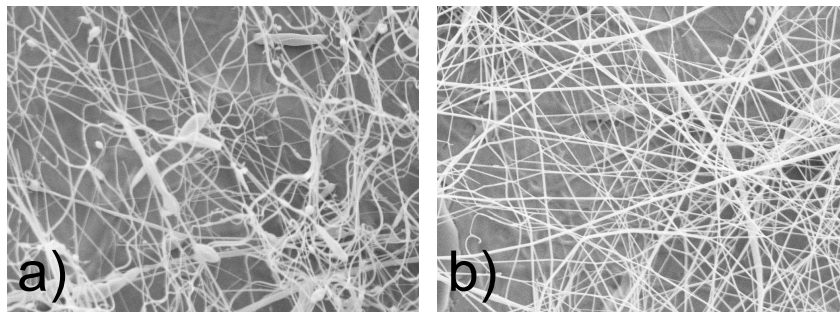


Figure 2.14: Fiber beading can be avoided by adjusting one or more of the electrospinning parameters as seen above when the voltage was adjusted from a)-10_20kV to b)-5_10kV.

The variables and parameters that influence the type of fiber that will form are summarized in Table 2.2. Processing parameters include the intrinsic properties of the electrospinning solution. The polymer type, chain conformation, viscosity, elasticity, polarity and electrical conductivity are all important contributions to the properties of the nanofibers. The surface tension of the solvent also influences the way that the solution will electrospin. The conditions within the lab also contribute to the end product of the electrospinning process. The last two factors that can impact the morphology and diameter of the fiber mat are humidity and temperature [87, 88].

Table 2.2: Parameters that effect electrospinning.

	Solution Properties		Processing Properties
1	Concentration and Viscosity	1	Applied voltage
2	Molecular Weight and Architecture	2	Flow rate
3	Conductivity	3	Tip to collector distance
		4	Atmospheric Temperature and Humidity

Minimizing the surface tension of the solvent causes one or more spherical droplets to form from out the electrospinning solution jet. The electrostatic repulsion between the

charges on the jet surface tends to increase the surface area. This is favorable for the formation of a thin jet rather than beads. Good viscoelastic forces within the polymer solution also prevents rapid changes in the shape of the fiber and afford more support for smooth fiber surfaces [87].

2.5.5 Chnw/EVOH electrospun fiber nanocomposites

Nanocomposites containing electrospun fibers can be made by using a melt pressing apparatus that can mold the fibers in between two polymer films. The temperature should be kept below the melting point of the fibers but high enough to allow the polymer films to melt. This is an excellent technique to ensure good compatibility and uniform dispersion between nanoparticles like chnw and a polymer matrix with different polarities.

Figure 2.15 shows the nanocomposites containing chnw/EVOH electrospun fibers sandwiched between two LDPE (low density polyethylene) films. The fibers that can be seen in between the two LDPE films affords proper support to the nanocomposite. It has been found in previous studies that nanocomposites with lower nanowhisker content show better and more uniform dispersion [23].

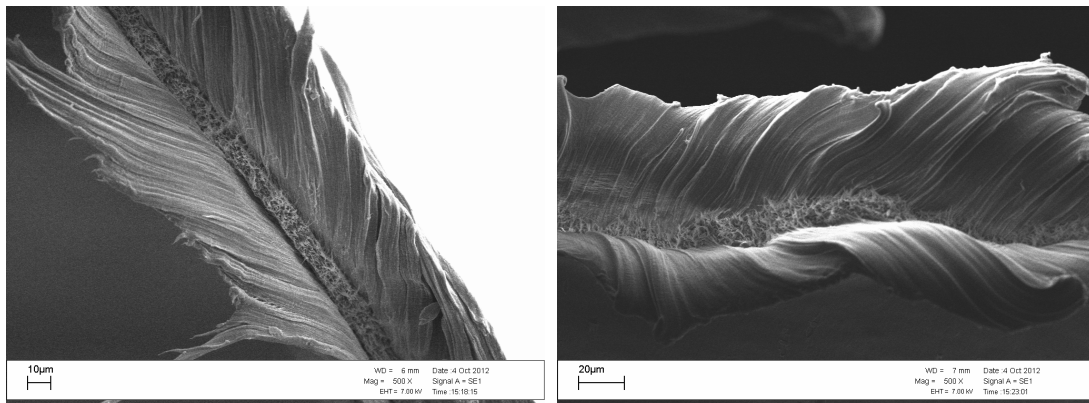


Figure 2.15: Nanocomposite consisting of EVOH-chnw electrospun fibers sandwiched between two LDPE films.

2.6 Characterization of isolated nanowhiskers and nanocomposites

2.6.1 Transmission electron microscopy (TEM)

Electrons are sent through the sample that then allows the viewer to see detailed images at a very small scale (to the order of a few angstroms). Negative staining with urinal acetate is used in order to increase the contrast between the different phases of the sample. In Figure 2.16 the TEM image for chnw is presented. Some agglomeration of chnw can be seen. TEM can be used to investigate the dispersion of the chnw. The size and shape of the nanowhiskers can also be established by using TEM.

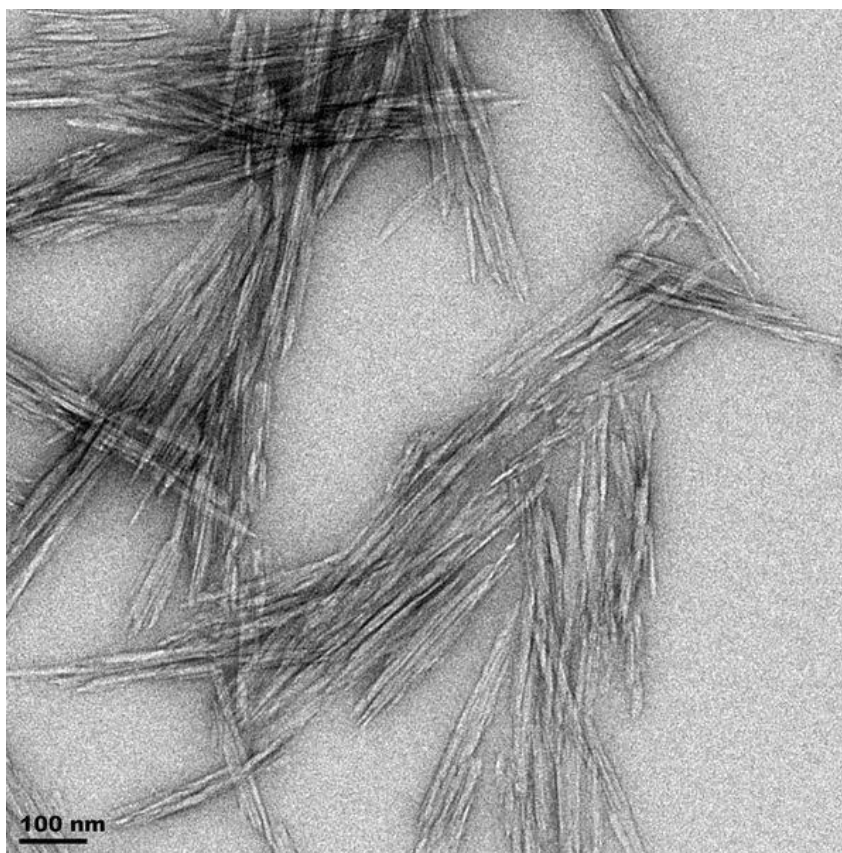


Figure 2.16: TEM image of chnw.

2.6.2 Scanning electron microscopy (SEM)

The information acquired here are more of a topographic type due to the fact that this microscope uses electrons to scan over the surface of a sample. Homogeneity of the nanocomposites as well as presence of voids can be studied using this technique. Nanowhisker dispersion and orientation can also be confirmed within the nanocomposite using with the use of a SEM instrument [89, 90, 91, 92, 93, 94].

2.6.3 Tensile testing

Mechanical strength of polysaccharide based nanocomposites can be determined using this relatively inexpensive and easy technique. The material will react to the force that is applied onto it and behave in a certain way. The material can either break immediately or elongate before it fractures. The amount of tension and the rate at which it is applied can be controlled during the experiment.

Tensile testing can be used to measure the Young's modulus, toughness and strength of the material. As mentioned earlier, macro particles can cause negative effects in composites due to the presence of defects and low surface area. Nano-scale particles are much more effective reinforcement for nanocomposites. Chitin nanowhiskers can agglomerate within a polymer matrix that can lead to ineffective reinforcement because of poor interaction between the nanofiller and polymer matrix.

2.6.4 Thermogravimetric analysis (TGA)

This technique allows the study of the thermal stability of composites and their individual components. This technique is used to measure any sort of loss in the weight of a sample with regards to temperature. This is done in a controlled environment where conditions, except for the temperature, are held constant. Samples will lose weight when it undergoes decomposition, oxidation or dehydration at certain temperature intervals.

2.6.5 Attenuated total reflectance-Fourier transform infrared (ATR-FTIR)

Different functional groups on a compound can absorb infrared radiation at various wavelengths. This allows the investigator to detect the presence of specific functional groups within a composite.

An attenuated total reflectance-Fourier transform infrared spectrometer is a very effective and simple instrument to use. Information about the chemical composition of the material

as well as evidence proving the presence of specific particles within the material (blend, composites etc.) can be acquired.

2.6.6 Differential scanning calorimetry (DSC)

This technique can help to determine the physical composition of the sample. The thermal transition of a sample can be measured while the conditions are completely controlled with a heating profile preprogrammed before the sample is allowed to run. Information such as the crystallinity, melting point, polydispersity of crystals as well as the glass transition temperature can be ascertained. DSC can also be used to detect changes in crystallinity and melting peaks of the matrix caused by the incorporation of fillers such as chnw.

2.6.7 Fluorescence microscopy

Transmission electron microscopy and scanning electron microscopy lack to provide decent imagery of filler on a nano-scale. Fluorescence microscopy can give the investigator an enhanced image with far better resolution and also show the dispersion of the nanofiller in the polymer matrix on a 3D level. This is done by using thin optical sections which can be obtained when combined with a laser scanning microscope (LSM). These sections can be stacked and forms the 3D picture that can show particle dispersion within the matrix on various levels and depths

References

- [1] A. Oromiehie, H. Ebadi-Dehaghani, and S. Mirbagheri, "Chemical modification of polypropylene by maleic anhydride: Melt grafting, characterization and mechanism," *International Journal of Chemical Engineering and Applications*, vol. 5(2), pp. 117–120, 2014.
- [2] P. Edward, "Polypropylene handbook," *Hanser Publishers, Munich*, p. 12, 1996.
- [3] Y. Zhang, J. Xu, H. Wang, L. Feng, and Z. Fan, *Polymer*, vol. 42, pp. 5559–5566, 2001.
- [4] P. Kittilsen and T. Mckenna, *Journal of Applied Polymer Science*, vol. 82, pp. 1047–1060, 2001.
- [5] J. Xu, Y. Zhang, Z. Fan, and Z. Fu, *Journal of Applied Polymer Science*, vol. 97, pp. 640–647, 2005.
- [6] Z. Fu, Z. Fan, Y. Zhang, and L. Feng, *European Polymer Journal*, vol. 39, pp. 795–804, 2003.
- [7] G. Bukatov, V. Zaikovskii, V. Zakharov, G. Kryukova, V. Fenelonov, and R. Zagradskaya, *Polymer Science USSR*, vol. 24, pp. 599–605, 1982.
- [8] H. Mahdavi and M. Nook, "Structure and morphology of a commercial high-impact polypropylene in-reactor alloy synthesized using a spherical ziegler-natta catalyst." *Polymer International*, vol. 59, pp. 1701–1708, 2010.
- [9] T. Mckenna, D. Bouzid, S. Matsunami, and T. Sugano, *Polymer Reaction Engineering*, vol. 11, pp. 177–197, 2003.
- [10] N. Basson, "The effect of molecular architecture on the properties of propylene impact copolymers." *University of Stellenbosch*, pp. 13–23, 2010.
- [11] J. A. Debling and H. W. Ray, *Journal of Applied Polymer Science*, vol. 81, p. 3085, 2001.
- [12] K. Nair and A. Dufresne, "Crabshell chitin whisker reinforced natural rubber nanocomposites, 1. processing and swelling behavior," *Biomacromolecules*, vol. 4(3), pp. 657–665, 2003.

- [13] A. Dufresne, S. Thomas, and L. Pothan, "Biopolymer nanocomposites: Processing properties and applications." *Wiley series on Polymer Engineering and Technology*, pp. 54–70, 2013.
- [14] M. Du Toit, "Incorporation of polysaccharide nanowhiskers into a poly (ethylene-co-vinyl alcohol) matrix," p. 1, 2013.
- [15] M. Ravi Kumar, "Reactive and functional polymers," *Biotechnol Biomaterial*, vol. 46, p. 1, 2000.
- [16] K. Kurita, H. Yoshino, K. Yokota, M. Ando, S. Inoue, S. Ishii, and S. Nishimura, "Preparation of tosyl chitins as precursors for facile chemical modification of chitin," *Macromolecules*, vol. 25, p. 3786, 1992.
- [17] K. Kurita, S. Inoue, and S. Nishimura, "Preparation of soluble chitin derivatives as reactive precursors for controlled modification: Tosyl-and iodo chitins," *Journal of Polymer Science Part A: Polymer Chemistry*, vol. 29, p. 937, 1991.
- [18] A. Einbu, "Characterisation of chitin and a study of its acid-catalysed hydrolysis." *Thesis for the degree of philosophiae.*, 2007.
- [19] M. Rinaudo, *Progress in Polymer Science*, 2006.
- [20] G. Crini, "Recent developments in polysaccharide-based materials used as adsorbents in wastewater treatment," *Progress in Polymer Science*, vol. 30(1), pp. 38–70, 2005.
- [21] A. Mera, J. Araki, T. Ohtsuki, M. Shimosaka, and N. Yoshida, *Biotechnol Biomaterial*, vol. 1, 2011.
- [22] J. Revol and R. Marchessault, *International Journal of Biological Macromolecules*, vol. 15, p. 329, 1993.
- [23] Y. Lu, L. Weng, and L. Zhang, "Morphology and properties of soy protein isolate thermoplastics reinforced with chitin whiskers," *Biomacromolecules*, vol. 5, pp. 1046–1051, 2004.
- [24] M. Paillet and A. Dufresne, *Macromolecules*, vol. 34, p. 6527, 2001.
- [25] A. Morin and A. Dufresne, *Macromolecules*, vol. 34, p. 6527, 2001.
- [26] A. Watthana Phanit, P. Supaphol, H. Tamura, S. Tokura, and R. Rujiravanit, *Journal of Applied Polymer Science*, vol. 110, p. 890, 2008.
- [27] V. Jacobs, R. Anandjiwala, M. John, A. Mathew, and K. Oksman, *TAPPI*, 2010.
- [28] T. Saito, A. Isogai, and Y. Fan, *Biomacromolecules*, vol. 9, p. 192, 2008a.

- [29] A. Isogai, Y. Fan, and T. Saito, *Biomacromolecules*, vol. 9, p. 1919, 2008b.
- [30] Y. Fan, T. Saito, and A. Isogai, *Carbohydrate Polymer*, vol. 79, p. 1046, 2010.
- [31] H. Zhao, X. Feng, and H. Gao, *Applied Physics Letter*, vol. 90, 2007.
- [32] B. Min, S. Lee, J. Lim, Y. You, T. Lee, P. Khang, and W. Park, *Polymer*, vol. 45, p. 7137, 2004.
- [33] S. Ifuku, M. Nogi, K. Abe, M. Yoshioka, M. Morimoto, H. Saimoto, and H. Yano, *Biomacromolecules*, vol. 10, p. 1584, 2009.
- [34] S. Ifuku, M. Nogi, M. Yoshioka, M. Morimoto, H. Saimoto, and H. Yano, *Carbohydrates Polymers*, vol. 81, p. 134, 2010.
- [35] R. Kose and T. Kondo, *Seni Gakkaishi*, vol. 2011, p. 91, 67.
- [36] J. Kadokawa, A. Takegawa, S. Mine, and K. Prasad, *Carbohydrate Polymers*, vol. 84, p. 1408, 2011.
- [37] H. Zheng, Z. Tan, Y. Ran Zhan, and J. Huang, "Morphology and properties of soy protein plastics modified with chitin," *Journal of Applied Polymer Science*, vol. 90(13), pp. 3676–3682, 2003.
- [38] A. Dufresne, "Processing of polymer nanocomposites reinforced with polysaccharide nanocrystal." *Open Access, Molecules*, vol. 15, p. 4111, 2010.
- [39] J. Zeng, Y. He, S. Li, and Y. Wang, "Chitin whiskers: An overview," *Biomacromolecules*, vol. 13(1), pp. 1–11, 2012.
- [40] L. Feng, Z. Zhou, A. Dufresne, J. Huang, M. Wei, and L. An, "Structure and properties of new thermoforming bionanocomposites based on chitin whisker-graft-polycaprolactone." *Journal of Applied Polymer Science*, vol. 112, pp. 2830–2837, 2009.
- [41] M. Mincea, A. Negrulescu, and V. Ostafe, "Preparation, modification, and applications of chitin nanowhiskers: a review," *Review on Advanced Material Science*, vol. 30, pp. 225–242, 2012.
- [42] D. Dubief, E. Samain, and A. Dufresne, *Macromolecules*, vol. 32, p. 5765, 1999.
- [43] K. Gopalan Nair and A. Dufresne, *Biomacromolecules*, vol. 4, p. 657, 2003.
- [44] Y. Yamamoto, T. Nishimura, T. Saito, and T. Kato, *Polymer Journal*, vol. 42, p. 583, 2010.
- [45] P. Hariraksapitak and P. Supaphol, *Journal of Applied Polymer Science*, vol. 117, p. 3406, 2010.

- [46] J. Junkasem, R. Rujiravanit, and P. Supaphol, *Nanotechnology*, vol. 17, p. 4519, 2006.
- [47] P. Wongpanit, N. Sanchavanakit, P. Pavasant, T. Bunaprasert, Y. Tabata, and R. Rujiravanit, *European Polymer Journal*, vol. 43, p. 4123, 2007.
- [48] A. Morin and A. Dufresne, "Nanocomposites of chitin nanowhiskers from rifting tubes and poly(caprolactone)," *Macromolecules*, vol. 35(6), pp. 2190–2199, 2002.
- [49] S. Eichorn, A. Dufresne, M. Aranguren, N. Marcovich, J. Capadona, and S. Rowan, "Review: Current international research into cellulose nanofibers and nanocomposites." *Journal of Materials Science*, vol. 45(1), pp. 1–33, 2010.
- [50] A. Lopez-Rubio, J. Lagaron, P. Hernandez-Munoz, E. Almenar, R. Catala, and R. Gavara, "Effect of high pressure treatments on the properties of evoh-based food packaging materials," *Innovative food science and emerging technologies*, vol. 6(1), pp. 51–58, 2005.
- [51] H. Mark, "Encyclopedia of polymer science and engineering," *John Wiley and sons Inc*, vol. 2(2), pp. 188–189, 1985.
- [52] C. Zhang, Y. Shangguan, R. Chen, and Q. Zheng, "Study on thermal behaviour of impact polypropylene copolymer and its fractions," *Journal of Applied Polymer Science*, vol. 119, p. 1560, 2011.
- [53] A. Lopez-Rubio, J. Lagaron, E. Gimenez, D. Cava, P. Hernandez-Munoz, T. Yamamoto, and et al., "Morphology alteration induced by temperature and humidity in ethylene-vinyl alcohol copolymers," *Macromolecules*, vol. 25, pp. 9467–9476, 2003.
- [54] J. Lagaron, E. Gimenez, and J. Saura, "Degradation of high barrier ethylene-vinyl alcohol copolymer under mild thermal-oxidative conditions studied by thermal analysis and infrared spectroscopy," *Polymer International*, vol. 50(6), pp. 635–642, 2001.
- [55] N. Artzi, M. Narkis, and A. Siegmann, "Evoh/clay nanocomposites produced by dynamic melt mixing," *Polymer Engineering and Science*, vol. 44(6), pp. 1019–1026, 2004.
- [56] L. Cabedo, J. Lagaron, D. Cava, J. Saura, and E. Gimenez, "The effect of ethylene content on the interaction between ethylene-vinyl alcohol copolymers and water: Influence of watersorption on the mechanical properties of evoh copolymers," *Polymer Testing*, vol. 25(7), pp. 860–867, 2006.
- [57] T. Young, C. Lin, L. Cheng, and C. Hsieh, "Preparation of eval membranes with smooth and particulate morphologies for neuronal culture," *Biomaterials*, vol. 22(13), pp. 1771–1777, 2001.

- [58] E. Kenawy, J. Layman, J. Watkins, G. Bowlin, J. Matthews, and D. Simpson, "Electrospinning of poly(ethylene-co-vinyl alcohol) fibers," *Biomaterials*, vol. 24(6), pp. 907–913, 2003.
- [59] C. Arboleda, A. Mejia, and B. Lopez, "Poly(vinyl alcohol-co-ethylene) biodegradation on semi solid fermentation by *Phanerochaete chrysosporium*," *Acta Farmacológica Bonaerense*, vol. 23(2), pp. 123–128, 2004.
- [60] A. Oyane, M. Kawashita, K. Nakanishi, T. Kokubo, M. Minoda, and T. Miyamoto, "Bonelike apatite formation on ethylene-vinyl alcohol copolymer modified with silane coupling agent and calcium silicate solution." *Biomaterials*, vol. 24(10), pp. 1729–1735, 2003.
- [61] J. Wen and G. Wilkes, "Surface modification of ethylene-vinyl alcohol (evoh) copolymer films by the attachment of triethoxysilane functionality," *Polymer Bulletin*, vol. 37(1), pp. 51–57, 1996.
- [62] J. Villalpando-Olamr, S. Sanchez-Valdes, and I. Yanez-Flores, "Performance of polyethylene/ethylene-vinyl alcohol copolymer/polyethylene multilayer films using maleated polyethylene blends," *Polymer Engineering and Science*, vol. 39(9), pp. 1597–1603, 1999.
- [63] K. Mokwena, J. Tang, and M. Laborie, "Water absorption and oxygen barrier characteristics of ethylene vinyl alcohol films," *Journal of food Engineering*, vol. 105(3), pp. 436–443, 2011.
- [64] A. Tidjani, O. Wald, M. Pohl, M. Hentschel, and B. Schartel, "Polypropylene-graft-maleic anhydride-nanocomposite: Characterization and thermal stability of nanocomposites produced under nitrogen and in air," *Polymer Degradation and Stability*, vol. 82, pp. 133–140, 2003.
- [65] A. C. Lopez de Dicastillo, M. Castro, J. Vilarino, and R. M. V. Gonzalez, "Study of the interaction between a natural antioxidant and anhydride maleic modified polypropylene formulations," *5th International Symposium on Food Packaging*, vol. Poster Presentation, 2012.
- [66] Bortolon, "Process for modifying polypropylene with maleic anhydride," *United State patent no. US 6,437,049 B1*, August 20, 2002.
- [67] F. Berzin, J.-J. Flat, and B. Vergnes, "Grafting of maleic anhydride on polypropylene by reactive extrusion: Effect of maleic anhydride and peroxide concentrations on reaction yield and products characteristics," *Journal of Polymer Engineering*, vol. 33(8), pp. 673–682, 2013.

- [68] V. Gaucher-Miri, G. Jones, R. Kaas, A. Hilther, and E. Baer, "Plastic deformation of eva, evoh and their multilayer," *Journal of materials Science*, vol. 37(13), pp. 2635–2644, 2002.
- [69] L. Dayodi, T. Janecska, Z. Szabo, G. Nagy, J. Moczo, and B. Pukanszky, "Wood flourfilled polypropylene composites: Compatibilization and adhesion," *Composites science and technology*, vol. 67(13), p. 2838, 2009.
- [70] Matuana, "Process for the preparation of maleated polyolefin modified wood particles in composites and products," *United States patent no. US 7, 605, 197 B2, October 20*, 2009.
- [71] L. Martin, "Overview of maleic-anhydride-grafted polyolefin coupling agents." *Add-comp Polymer additive solutions*.
- [72] M. Henriette and A. De, "Nanocomposites for food packaging applications," *Food Research International*, vol. 43(9), pp. 1240–1253, 2009.
- [73] A. Balazs, T. Emrick, and T. Russel, "Nanoparticle polymer composites: Where two small worlds meet." *Science*, vol. 314(5802), pp. 1107–1110, 2006.
- [74] V. Hristov, M. Krumova, S. Vasileva, and G. Michler, "Modified polypropylene wood flour composites: Fracture, deformation and mechanical properties," *Journal of Applied Polymer Science*, vol. 92, p. 1286, 2004.
- [75] M. Alexandre and P. Dubois, "Polymer-layered silicate nanocomposites: Preparation, properties and uses of a new class of materials," *Materials Science and Engineering*, vol. 28, pp. 1–63, 2000.
- [76] L. Luduena, V. Alvarez, and A. Vasquez, "Processing and microstructure of pcl/clay nanocomposite," *Materials Science and Engineering: A*, pp. 21–129, 2007.
- [77] J. Sriupayo, P. Supaphol, J. Blackwell, and R. Rujiravanit, "Preparation and characterization of α -chitin whiskers-reinforced chitosan nanocomposite films with or without heat treatment," *Carbohydrate Polymers*, vol. 62(2), pp. 130–136, 2005.
- [78] J. Fricain, S. Schlaubitz, C. Le Visage, I. Arnault, S. Derkaoui, R. Siadous, S. Catros, C. Lalande, R. Bareille, M. Renard, T. Fabre, S. Cornet, M. Durand, A. Leonard, N. Sahraoui, D. Letourneur, and J. Amedee, "A nano-hydroxyapatite-pullulan/dextran polysaccharide composite macroporous material for bone tissue engineering," *Biomaterials*, vol. 34(12), pp. 2947–59, 2013.
- [79] S. Agarwal, J. Wendorff, and A. Greiner, "Use of electrospinning technique for biomedical applications," *Polymer*, vol. 49, pp. 5603–5621, 2008.

- [80] D. Reneke and I. Chun, "Nanometre diameter fibers of polymer, produced by electrospinning," *Nanotechnology*, vol. 7(3), p. 216, 1996.
- [81] G. Taylor, "Electrically driven jets," *Proceeding of the Royal Society A313*, vol. 1515, p. 453, 1969.
- [82] Rob, "The new zealand institute for plant and food research ltd."
- [83] J. Gatford, *The New Zealand Institute for Plant and Food Research Ltd.*
- [84] N. Haitao and L. Tong, "Fiber generations in needeless electrospinning." *Journal of Nanomaterials*, vol. 2012, pp. 1–4, 2012.
- [85] H. Pan, L. Li, L. Hu, and X. Cui, "Continuous aligned polymer fibers produced by a modified electrospinning method." *Polymer*, vol. 47(14), pp. 4901–4904, 2006.
- [86] L. Huaqiang, W. Yiqiong, W. Meiyu, Z. Xianrong, and L. Haiqing, "Aligned electrospun cellulose fibers reinforced epoxy resin composite films with high visible light transmittance," *Cellulose*, vol. 19(1), pp. 111–119, 2012.
- [87] L. Dan and X. Younan, "Electrospinning of nanofibers: Reinventing the wheel?" *Advanced Materials*, vol. 16(14), pp. 1151–1166, 2004.
- [88] Z. Huang, Y. Zhang, M. Kotaki, and S. Rmakrishna, "A review on polymer nanofiber by electrospinning and their applications in nanocomposites." *Composites Science and Technology*, vol. 63(15), pp. 2223–2253, 2003.
- [89] M. Peresin, Y. Habibi, J. Zoppe, J. Pawlak, and O. Rojas, "Nanofiber composites of polyvinyl alcohol and cellulose nanocrystals: Manufacture and characterization." *Biomacromolecules*, vol. 11(3), pp. 647–681, 2010.
- [90] R. Olsson, R. Kraemer, A. Lopez-Rubio, S. Torres-Giner, M. Ocio, and J. Lagaroin, "Extraction of microfibrils from bacterial cellulose networks for electrospinning of anisotropic biohybrid fiber yarns." *Macromolecules*, vol. 43(9), pp. 4201–4209, 2010.
- [91] I. Kvien, B. Tanem, and K. Oksman, "Investigation of the structure of cellulose whiskers and its nanocomposites using tem, sem, afm and x-ray diffraction," *8th International conference on wood fiber-plastic composites*, 2005.
- [92] P. Lu and Y. Hsieh, "Preparation and properties of cellulose crystals: Rods, spheres and network." *Carbohydrate Polymers*, vol. 2(2), pp. 329–336, 2010.
- [93] P. Visakh, S. Thomas, K. Oksman, and A. Mathew, "Crosslinked natural rubber nanocomposites reinforced with cellulose whiskers isolated from bamboo wast: Processing and mechanical/thermal properties," *Composites Part A: Applied Science and Manufacturing*, vol. 43(4), pp. 735–741, 2012.

- [94] M. Azizi Samir, S. Ahmed, F. Alloin, J. Snachez, N. El Kissi, and A. Dufresne, “Preparation of cellulose whiskers reinforced nanocomposites from an organic medium suspension.” *Macromolecules*, vol. 37(1), pp. 1386–1393, 2004.

Chapter 3

Experimental

3.1 Materials

High impact polypropylene was selected as the polymer matrix (HiPP, CMR 648, Sasol Polymers, ethylene content 14.87%). Two types of compatibilizer were chosen poly propylene-*graft*-maleic anhydride (PPgMA) and poly (ethylene-*co*-vinyl alcohol) (EVOH, with an ethylene content of 32%) from SIGMA - Aldrich. Chitin Nanowhiskers (derived from Chitin, *N*-acetyl-1, 4- β -D-glucopyranosamine, supplied by USA from shrimp shells) were used as the reinforcing nanofiller. Xylene, DMSO and an 70/30% isoproponal/water solution was used as solvent (SIGMA). Stabilizers (2% w/w mixture of Irganox1010 and Irgafos168) was added during this dissolution to prevent degradation during the processing of composites.

3.2 Preparation of chitin nanowhiskers

Chitin nanowhiskers were prepared according to the method described in Mincea *et al.* [1]. The preparation of chitin nanowhiskers consists of 4 main procedures:

1. Hydrolysis
2. Centrifugation
3. Dialysis
4. Freeze drying

Acid hydrolysis was done using 3 g chitin and 90 mL of 3 M HCl. The solution was heated up to 105 °C and kept there for 4 hours. A beaker of about 90 mL iced distilled water was added after the 4 hours. Centrifugation was done six times of 5 minutes each at high rpm. During the centrifugation process the chitin nanowhiskers were separated from the larger particles within the solution and decanted into dialysis tubes. The dialysis tubes were placed in a large holder filled with distilled water. The water needed to be changed three

time daily in order to remove the acid within the chnw solution. After 7 - 10 days the chitin nanowhiskers solution was placed in round-bottom flasks and frozen using liquid nitrogen and dried under vacuum on the freeze dryer.

The chitin nanowhiskers were produced after freeze drying and had a white cotton-like appearance. Ultra-sonification was necessary in order to enhance the dispersion of the chitin nanowhiskers when these nanowhiskers were redispersed within the distilled water or solvent for the production of nanocomposites.

3.3 Preparation of HiPP/chnw composites with PPgMA as compatibilizer

Chitin nanowhiskers were added in varying concentrations to the solution of HiPP while the PPgMA concentration was held constant at 2 wt%, 4 wt%, 6 wt%, 8 wt% and 10 wt%. The varying chitin nanowhisiker loadings were selected as 3 wt%, 5 wt%, 8 wt% and 10 wt%. Chitin nanowhiskers were sonicated separately for an hour, each in 10 mL xylene while PPgMA was dissolved at 135 °C in 20 mL xylene. The well dispersed chnw was then added to the PPgMA and allowed to mix for 2 minutes at 135 °C. This solution was then added to the HiPP solution and was mixed for another 2 minutes on a magnetic heating stirrer plate with a magnetic stirrer at medium rotation speed while the temperature was kept constant at 135 °C.

This solution was then attached to a rotary evaporator and the solvent was evaporated off at a temperature of 60 °C at 40 mbar. The sample was placed in a vacuum oven for 4 hours at 60 °C to ensure all the solvent has evaporated [2]. The composite sample was a white dry powder that could be injection molded and investigated further.

3.4 Preparation of HiPP/chnw composites with EVOH as compatibilizer

Two different methods were used for incorporation of chnw into the HiPP matrix. The first method that was used consist of solvent casting and injection molding. The second method that was used was electrospinning followed by metlpressing.

The procedure for the first processing method was as follows: The same procedure as described for Section 3.3 was used for making nanocomposites with the exception of a few small changes in order to compensate for the insolubility of EVOH in xylene [2]. Poly(ethylene-*co*-vinyl alcohol) was dissolved in 10 mL DMSO for an hour at 135 °C and

the chnw were sonicated in 10 mL DMSO for an hour. High impact polypropylene was dissolved with 2 wt% stabilizer in 20 mL xylene instead of 300 mL as in the case of section 3.3. The rest of the method remained the same as mentioned above. During rotary evaporation the xylene was first evaporated off at 40 mbar followed by the DMSO at 18 mbar.

The conditions for the electrospinning of EVOH/chnw fiber mat are tabulated in Table 3.1. Poly (ethylene-*co*-vinyl alcohol) was dissolved in an isopropanol/water (70/30%) solution in order to get a 5 wt% EVOH solution. The chitin nanowhiskers were redispersed in an isopropanol/water (70/30%) solution using ultra-sonification and then incorporated into the EVOH fibers in loadings of 3 wt%, 5 wt%, 8 wt% and 10 wt% chitin nanowhiskers. The solution of chitin nanowhiskers within EVOH and also a solution of neat EVOH was made up at a reaction temperature of 90 °C with an isopropanol/water (70/30%) solution. After electrospinning, the fiber mats were placed between two HiPP films and melt pressed at 185 °C for 3 minutes under a maximum pressure of 3 bars.

Table 3.1: Electrospinning conditions.

Conditions	Setting
Voltage	15 kV
Temperature	23 - 25 °C
Solvent	30/70% water/isopropanol
Needle to tip distance	15 cm

3.5 Injection molding

Composite samples were molded into tensile bars with a HAAKE Mini Jet II from Thermo Scientific (type 557 - 2290). Five tensile bars were molded for each composite sample using injection molding. All composites that was produced with the the first technique, solvent casting, were subjected to injection molding in order to from tensile bars for further analysis with tensile testing. The only composite samples that were not subjected to injection molding were the electrospun fiber mats and the electrospun fiber mats nanocomposites.

The following settings for injection molding were used:

1. Cylinder temperature: 250 °C
2. Mold temperature: 80 °C
3. Injection pressure: 250 bar

4. Post (hold) pressure: 250 bar
5. Removal of sample

3.6 Hydraulic melt pressing

A hydraulic melt press (APEX Construction Ltd.) was used to heat the mold and press HiPP films. Sample preparation involved dissolution of the HiPP pellets in xylene followed by precipitation with acetone or rotary evaporation in order to convert the pellets into powder form. The precipitated powder was dried in a vacuum oven for 4 - 6 hours until the solvent was completely removed. 3 g of sample was used with 2 wt% stabilizer added to the polymer. The films were melt-pressed at 180 - 185 °C for 3 minutes, applying a pressure of 2 bars for 2 minutes, and then 3 bars for 1 minute. The sample was then removed and allowed to cool down.

3.7 Methods of characterization

3.7.1 TEM analysis

Transmission electron microscopy was used to obtain images of chitin nanowhiskers. A dilute droplet of redispersed chitin nanowhiskers was placed on a carbon coated TEM grid and was negatively stained with urinal acetate. A LEO 912 EM TEM instrument was used to obtain images of lower and higher magnification.

3.7.2 ATR-FTIR

One hundred scans were done for each sample. All the composites, EVOH/chnw electrospun fibers and neat EVOH electrospun fiber mats were investigated using ATR-FTIR. Analysis of composites and the individual compounds were done at room temperature using a Thermo Fisher Nicolet iS10 Attenuated total reflectance-Fourier Transform Infrared spectrometer in absorbance mode format with a resolution of 4 cm^{-1} .

3.7.3 TGA

The thermal stability of the composite materials as well as the electrospun fiber mats were analyzed using a Q500 TGA7 instrument (Perkin Elmer, USA). The TGA analyses were done under a nitrogen atmosphere. The samples were heated up over a temperature range of 25 - 900 °C at a rate of 20 °C/min.

3.7.4 SEM analysis

A Leo® 1430VP Scanning Electron Microscope at the central analytical facility of Stellenbosch University was used to analyze the morphology of the electrospun fibers mats and the nanocomposites. Gold coated samples were mounted on a stub using double sided carbon tape. Images were obtained in low and high magnifications (X1000 and X10000 respectively). Beam conditions during surface analysis were 7 KV and approximately 1.5 nA, with a working distance of 13 mm and a spot size of 150.

3.7.5 DSC

The change in crystallization and melting temperature of the composites and fibers were analyzed using a Q100 (TA instruments) DSC instrument. An indium standard was used under standard conditions. The procedure consisted of three cycles and a heating/cooling ramp of 10 °C/min. The temperature range was set for -20 - 200 °C and kept isothermal for 5 min at the last temperature. The thermal history was removed in this same way before analysis of the samples.

3.7.6 Tensile testing

The thickness for each tensile bar was measured before analysis. At least five specimens were tested for each composite sample in order to work out average for the tensile results. The analyses were done using a LRX (LLOYD instruments) tensile tester. The test speed was 50 mm/min and the initial force was 1 N. The sample dimensions were: gauge length 14.45 mm, width 3.02 mm, thickness 0.760 mm.

3.7.7 Fluorescence microscopy

Fluorescein isothiocyanate (FITC) was used as green fluorescence dye. The color green appears around 510 nm on the emission spectrum and that is what the confocal microscope was set to detect. Chitin nanowhiskers were dissolved in NaOH and sonicated for 5 min and then covered with foil. Fluorescein isothiocyanate and NaOH were mixed in a polytop and transferred to the chnw solution which was once again covered with foil and left to stand for 72 hours. Image acquisition was performed on a Carl Zeiss Laser Scanning Microscope (LSM) 780.

The setup for the experiment was as follows:

1. Laser: 488 nm (set at 4.5% laser power)
2. Beam splitters (used to direct light to the sample):
 - MBS: 488

- MBS InVis: Plate
3. FW1: None LSM
 4. Master gain: 800
 5. Filter (used to detect emitted fluorescence) 490-578
 6. Z-stack was performed with an increment of 1.500 μm
 7. Objective used: alpha Plan-Apochromat 100 x
 8. The Images were acquired with a pixel dwell time of 3.15 μs .
 9. Zoom: 1.0
 10. Pin hole: 77 μm

References

- [1] M. Mincea, A. Negrulescu, and V. Ostafe, "Preparation, modification, and applications of chitin nanowhiskers: a review," *Review on Advanced Material Science*, vol. 30, pp. 225–242, 2012.
- [2] N. Basson, "The effect of molecular architecture on the properties of propylene impact copolymers." *University of Stellenbosch*, pp. 13–23, 2010.

Chapter 4

Characterization of chitin nanowhiskers

4.1 Transmission electron microscopy

Transmission electron microscopy was used to analyze the produced chitin nanowhisker (chnw) diameter and length. Figure 4.1 illustrates chnw dispersed within a high impact polypropylene (HiPP) matrix. The fiber lengths of the chnw were between 150 - 250 nm with an average fiber diameter of 12 nm. Some single nanowhiskers can be seen in Figure 4.1 as well as some aggregation but with no apparent defects or flaws [1]. The aggregation is due to the high specific area and hydrogen bonding that occurs among the chitin nanowhiskers [2]. Solution of the chitin nanowhiskers that was not freeze dried and then redispersed appeared to have a homogeneous appearance. Only the chitin nanowhiskers that were previously freeze dried and then redispersed in distilled water presented agglomeration. Observations with the naked eye showed that chitin nanowhiskers that were redispersed in distilled water began to settle at the bottom of the polytop. Chitin nanowhiskers sampled from the dialysis tube before freeze drying remained in solution.

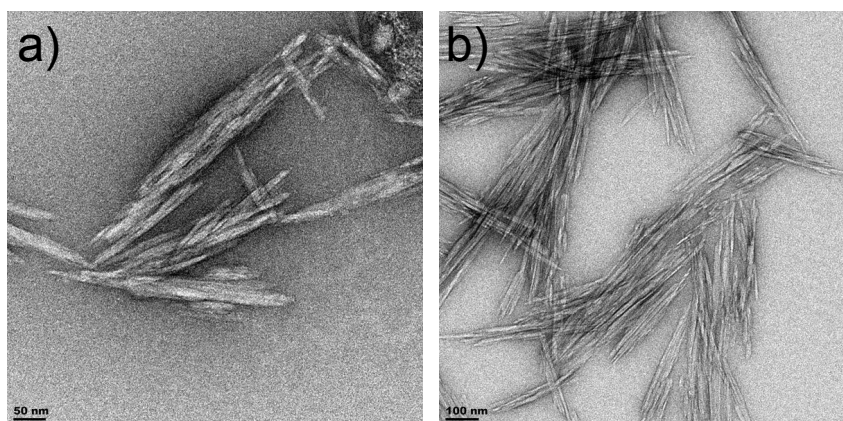


Figure 4.1: TEM images of chitin nanowhiskers a) redispersed after freeze drying and b) sampled directly from a dialysis tube.

During acid hydrolysis the chnw acquires a negative charge. The chitin nanowhiskers repel each other due to this charge and this allows good dispersion within the nanocomposite.

After freeze drying this charge is lost once the nanowhiskers are dry and thereafter they tend to aggregated at high concentration within solution.

4.2 Fourier transform infrared analysis

The FTIR spectrum of chitin nanowhiskers illustrated in Figure 4.2 shows the characteristic absorption bands [3] for the amide moieties at 1580 cm^{-1} , 1625 cm^{-1} and 1662 cm^{-1} . Although it is not possible to accurately determine concentration using ATR-FTIR, an increase in the intensity of the characteristic peaks indicates increased chnw content within the composite. The presence of the chitin nanowhiskers within a nanocomposite can be proved using FTIR. The important reactive hydroxyl groups that will interact with the maleic anhydride portion of PPgMA can also be identified using FTIR. These groups can be seen at 3250 cm^{-1} . The sharp peaks belonging to the hydroxyl group indicates the high crystallinity of chnw [4].

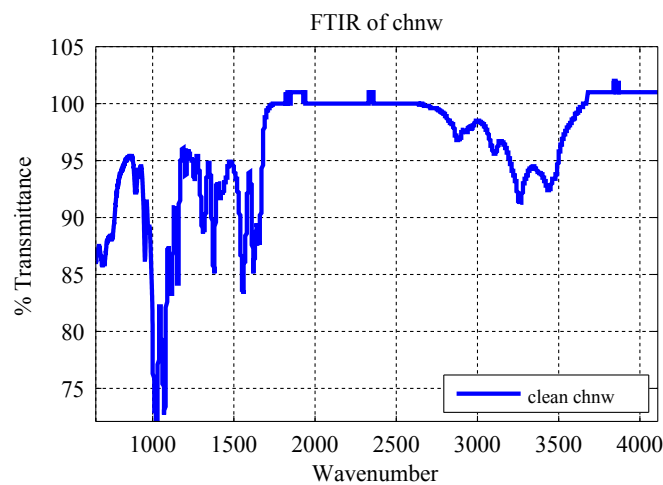


Figure 4.2: FTIR of pure chnw

4.3 Thermogravimetric analysis

The onset temperature of degradation is very similar for chitin and chnw. The hydrochloric acid that chitin is treated with to produce chnw as well as the strong hydrogen bonding that exist between the chitin nanowhisiker molecules because of the amide moieties allow for thermal stability [5].

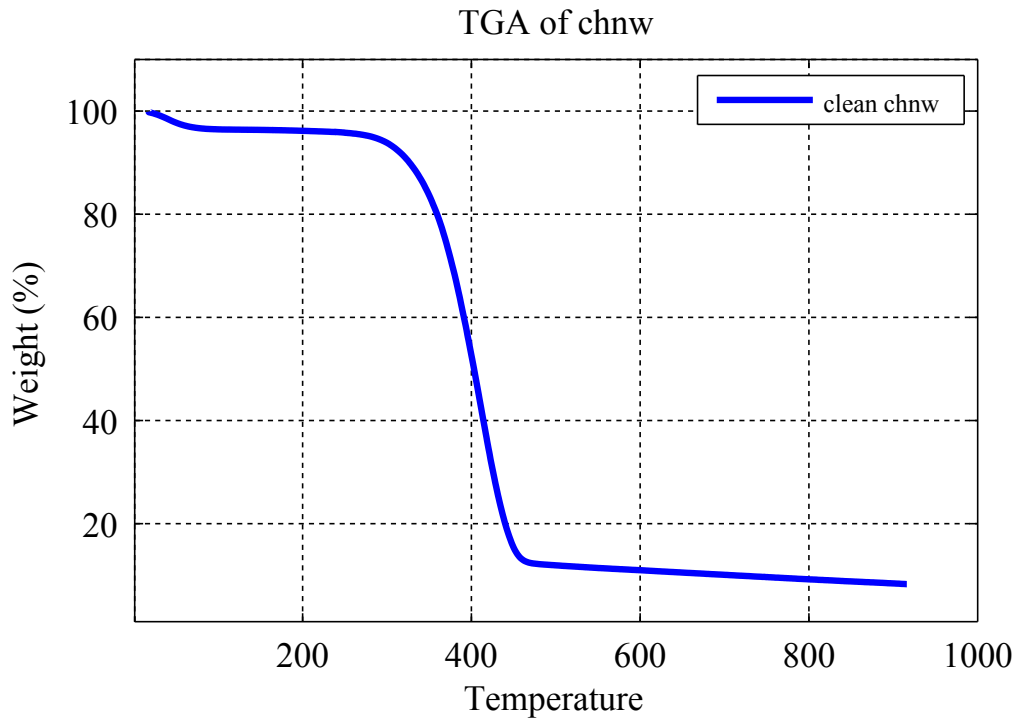


Figure 4.3: TGA curves of chitin nanowhiskers.

Figure 4.3 presents the TGA curve chnw. An immediate drop in the initial slope can be seen as loss of moisture within the chnw sample. This loss of moisture continues up to approximately 60 °C and then stabilizes for a while. An increase in weight loss then continues with a significant decline in the slope of the curve at 280 °C and becomes more gradual at approximately 470 °C [5].

4.4 Conclusion

Transmission electron microscopy shows the spindle rod-like shape of the chitin nanowhiskers. The images from TEM also indicates the good nano-scale dimensions of the chnw. A tendency to agglomerate was seen for chnw that were redispersed in solution after the freeze drying process.

The increase in crystallinity is a very important feature seen for chnw compared to chitin. The important reactive groups can be visualized in the FTIR spectra for chnw with particular focus on the amide moieties. The thermal stability for chnw and chitin is very similar and can be ascribed to these amide moiety groups that afford strong hydrogen bonding between the chnw ofr chitin chains. These reactive groups as well as the increased crystallinity and flawless nano-scale diameters of chnw is what will lend excellent mechanical properties to a nanocomposite.

References

- [1] V. Favier, H. Chanzy, and J. Cavaille, "Polymer nanocomposites reinforced by cellulose whiskers." *Macromolecules*, vol. 28, pp. 6365–6367, 1995.
- [2] J. De Mesquita, C. Ponnici, and F. Pereira, "Biobased nanocomposite from layer-by-layer assembly of cellulose nanowhiskers with chitosan." *Biomacromolecules*, vol. 11, pp. 473–480, 2010.
- [3] Y. Lu, L. Weng, and L. Zhang, "Morphology and properties of soy protein isolate thermoplastics reinforced with chitin whiskers," *Biomacromolecules*, vol. 5, pp. 1046–1051, 2004.
- [4] L. Heath, L. Zhu, and W. Thielmans, "Chitin nanowhisiker aerogels," *Chemsuschem*, vol. 6(3), pp. 537–544, 2013.
- [5] M. Du Toit, "Incorporation of polysaccharide nanowhiskers into a poly (ethylene-co-vinyl alcohol) matrix," p. 1, 2013.

Chapter 5

Results for HiPP/chnw nanocomposites with PPgMA as compatibilizer

In this study two types of compatibilizers were used in order to find optimized interaction and dispersion of the nanofibers within the nanocomposites. Chapter 5 will present the results and discussion for the HiPP/chnw nanocomposites synthesized using PPgMA as compatibilizer.

Polypropylene-*graft*-maleic anhydride presented no problems during the process of incorporating chnw into the matrix. Polypropylene-*graft*-maleic anhydride and chnw were dissolved within xylene and then mixed with HiPP. Xylene was used as solvent throughout the solvent casting process. Xylene is highly volatile and was easy to evaporate off before the injection molding process. Good interaction between the hydroxyl groups on PPgMA and the hydrophilic region in chnw allowed for good miscibility between the HiPP matrix and chnw.

Fluorescence microscopy was used to analyze the dispersion of chnw in HiPP matrix and to see the influence of PPgMA on the nanocomposite. Differential scanning calorimetry and thermal gravimetric analysis showed how the incorporation of chnw and PPgMA influenced the thermal properties of the nanocomposite. The tensile properties of the nanocomposites were investigated using tensile testing.

5.1 Fluorescence microscopy analysis

Preparing fluorescent-labeled chnw within all the nanocomposites with varying PPgMA loadings was a time consuming process and costly because a huge bulk of chitin is required to make only a small amount of chnw. Judging from the thermal and tensile analysis of the nanocomposites, a high loading of chnw within the HiPP matrix can become aggregated. We decided to take a nanocomposite sample with a PPgMA loading of 6 wt% as a representative of the overall dispersion of the chnw within the HiPP matrix and added a low and high loading of FITC-labeled chnw and illustrated the differences occurring in

the nanocomposites using confocal microscopy.

Confocal microscopy was used on the nanocomposites sample containing 3wt% chnw and 6 wt% PPGMA and the nanocomposite sample containing 8 wt% chnw and 6 wt% PPGMA to get an idea of the dispersion of chnw within the HiPP matrix. The nanocomposite sample containing 3wt% chnw and 6 wt% PPGMA presented in Figure 5.1(a) and (b) showed good dispersion of chnw within the HiPP matrix and agglomeration of chnw are fairly low. The nanocomposite sample containing 8 wt% chnw and 6 wt% PPGMA shown in Figure 5.1 (c) and (d) presented agglomeration within the HiPP matrix, with region containing bulky, aggregated chnw particles and other regions that barely have any chnw present as seen in Figure 5.1 (c). These images indicate that chnw are not uniformly dispersed and tend to agglomerate at higher concentrations due the strong hydrogen bonding that occur between the chnw chains [1]. Overall dispersion of a lower chitin nanowhiskers loading within the nanocomposite appeared to be good although only a very small frame of the nanocomposite can be examined with the fluorescence microscope because of the small diameters of the chnw within the HiPP matrix.

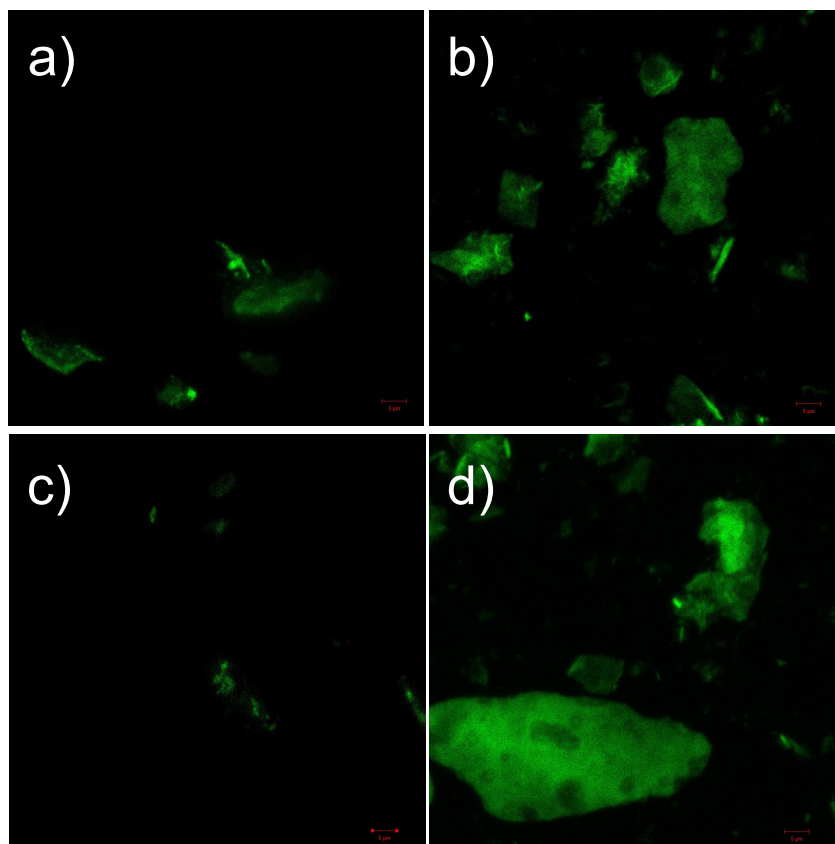


Figure 5.1: Confocal microscope images of nanocomposites containing a) 3 wt% chnw and 6 wt% PPGMA (Frame 1) b) 3 wt% chnw and 6 wt% PPGMA (Frame 2) and c) 8 wt% chnw and 6 wt% PPGMA (Frame 1) d) 8 wt% chnw and 6 wt% PPGMA (Frame 2)

5.2 Attenuated total reflectance-fourier transform infrared spectroscopy (ATR-FTIR)

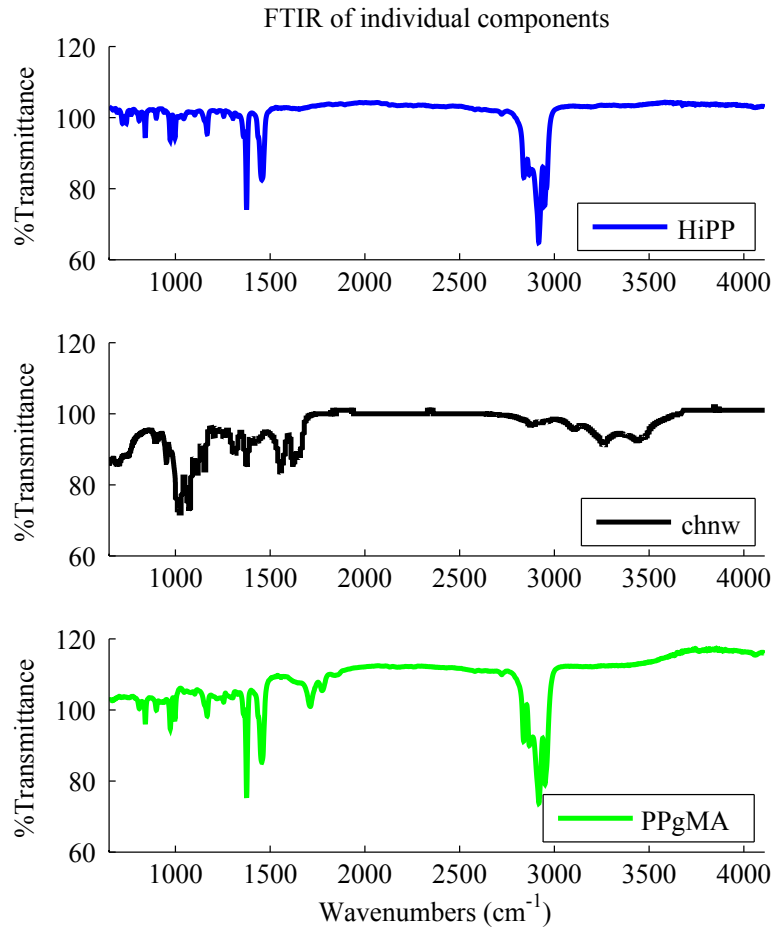


Figure 5.2: FTIR spectra of clean components.

Infrared spectroscopy was used to determine the presence of chnw and PPgMA in the nanocomposite. Figure 5.2 shows the IR spectra for all the neat components (HiPP, chnw and PPgMA) that were incorporated into the nanocomposite. Polypropylene-*graft*-maleic anhydride have two distinguished peaks between 1800 cm^{-1} and 1700 cm^{-1} and these are ascribed to the two ester carbonyl groups within the closed maleic anhydride ring structure that is found on the polymer backbone [2]. High impact polypropylene have two peaks between 1500 cm^{-1} and 1400 cm^{-1} that can be ascribed to the polypropylene segment within HiPP. The polypropylene portion of PPgMA have peaks in the same IR-range as the polypropylene portion of HiPP. At 720 cm^{-1} a peak ascribed to the ethylene sequence can be seen specifically for HiPP, which means that ethylene segments or blocks are present in the HiPP structure [3, 4, 5]. Clean chnw have prominent peaks at 1580 cm^{-1} , 1625 cm^{-1} and 1662 cm^{-1} that belongs to the amide moieties caused by

carbonyl stretching [6, 7, 1].

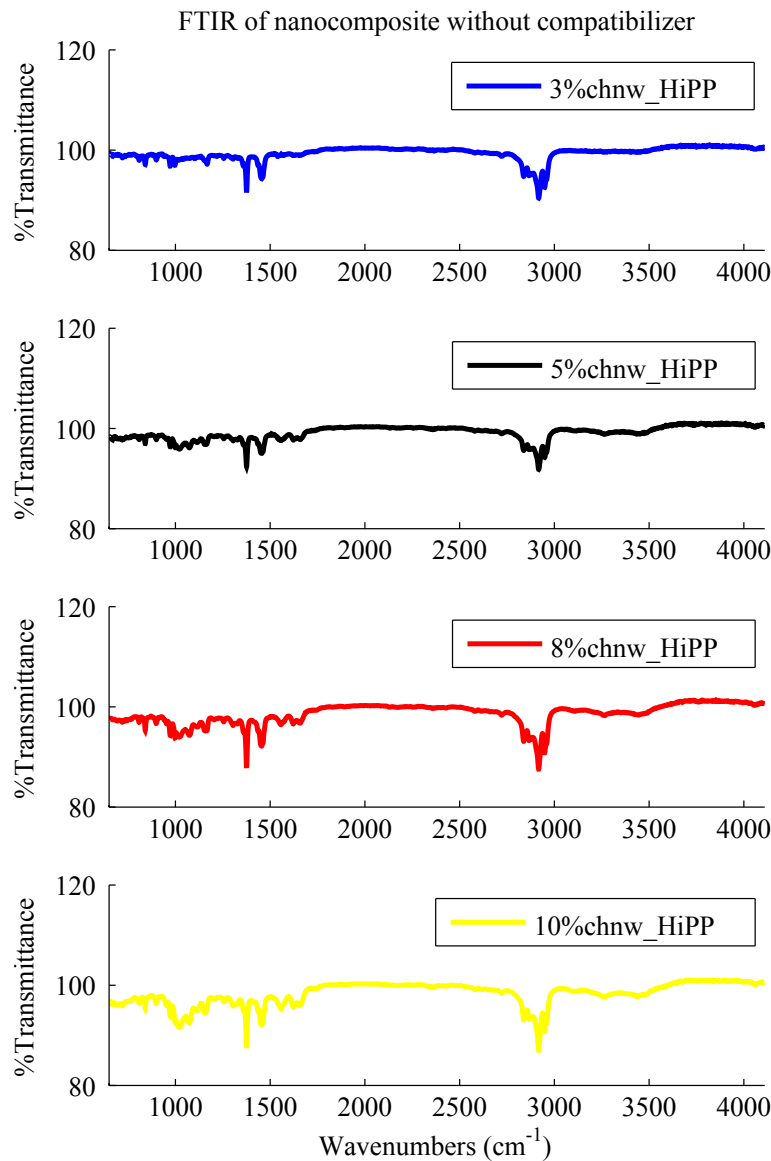


Figure 5.3: FTIR spectra of nanocomposite without compatibilizer.

The infrared spectra shown in Figure 5.3 for the nanocomposites without compatibilizer clearly shows the missing PPgMA peaks. The two peaks correlating to the maleic anhydride reactive group in PPgMA that is usually seen between 1800 cm^{-1} and 1700 cm^{-1} are not present. The peaks that can be spotted at 1580 cm^{-1} and 1662 cm^{-1} , next to the peaks belonging to the polypropylene portion of HiPP, belong to the amide moieties of chnw. This Figure presents increase in the peak intensity belonging to the chnw as the loading of the chnw is increased within the HiPP matrix.

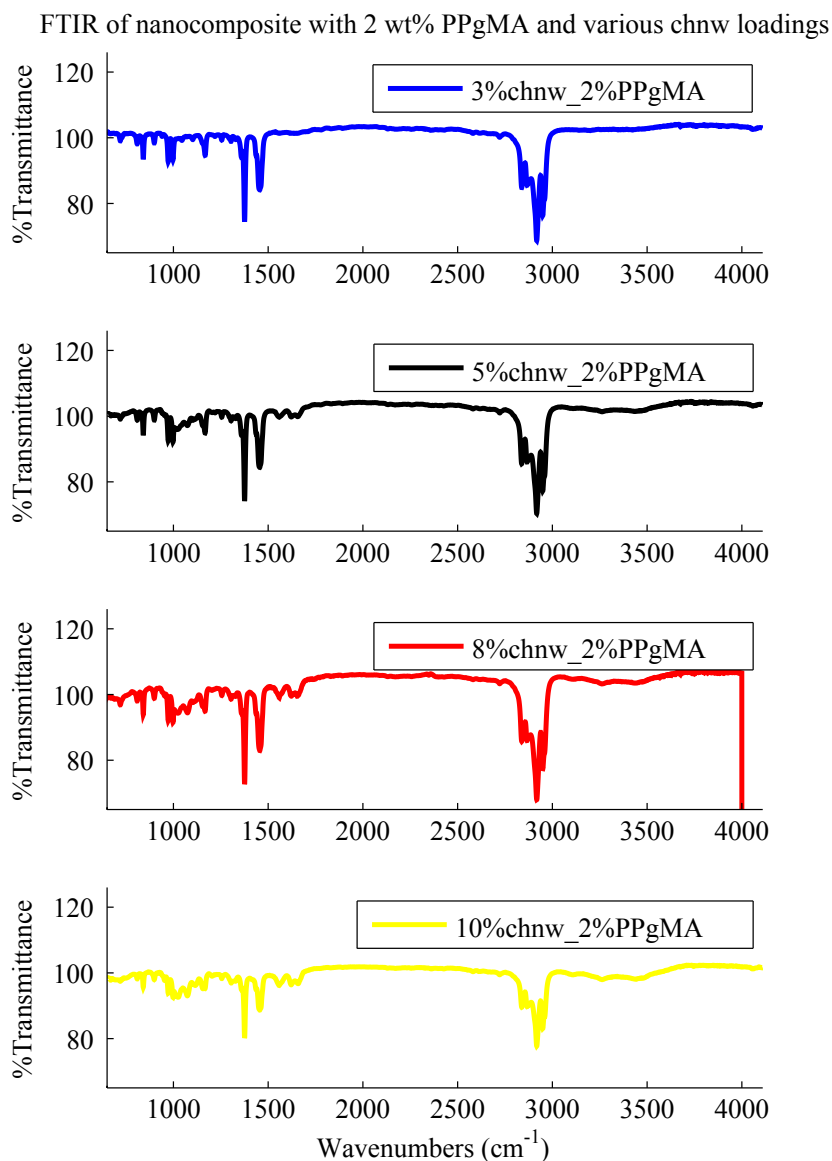


Figure 5.4: FTIR spectra of nanocomposites consisting of the HiPP matrix, 2 wt% PPGMA and varying chnw loadings.

Figure 5.4 shows the presence of the IR peak belonging to the maleic anhydride group of PPGMA between 1700 cm^{-1} and 1800 cm^{-1} . The characteristic peaks of the amide moieties for chnw are also present within the HiPP matrix. The intensity of the characteristic peaks for chnw between 1580 cm^{-1} and 1662 cm^{-1} are diminished at low chnw loadings. The peak intensities for PPGMA seems to remain about the same as for the clean sample of PPGMA. The lowering in intensity of the chnw peaks are because the polypropylene regions are more dominating compared to the chnw within the nanocomposite. The chnw becomes more obscured by the segments that belongs to the HiPP matrix. The decrease of the intensity of the amide moiety peaks belonging to chnw for the nanocomposite sample containing 10 wt% chnw and 2 wt% PPGMA could be because the samples that were used

contained unevenly distributed chnw within the nanocomposite caused by aggregation of chnw at high chnw loadings. This meant that the amount of chnw varied in some of the regions within the HiPP matrix and thus effecting the spectra and the peak intensities. The broad peak seen between 3350 cm^{-1} and 3400 cm^{-1} are indicative of the H-bonded hydroxyl groups of chnw which increase in intensity as the chnw concentration is increased from 3 wt% to 10 wt% chnw.

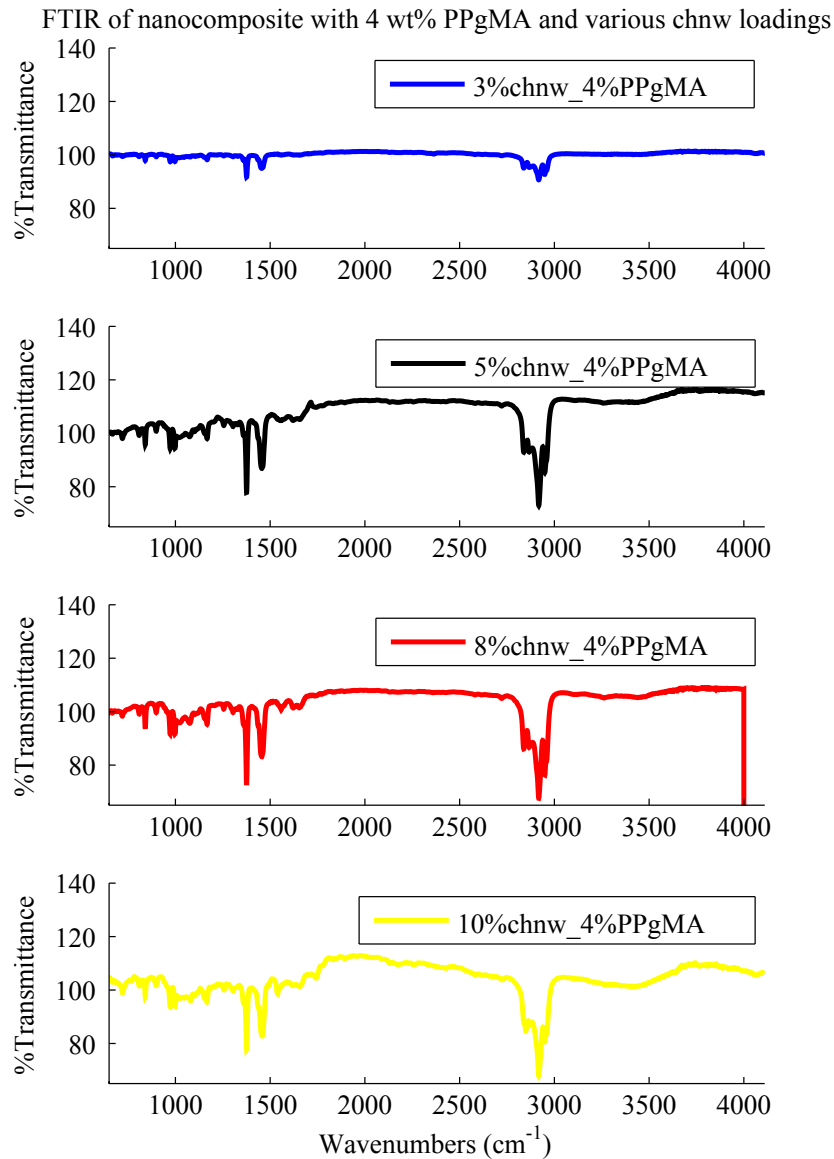


Figure 5.5: FTIR spectra of nanocomposites consisting of the HiPP matrix, 4 wt% PPgMA and varying chnw loadings.

Note that the scale was adjusted slightly for Figure 5.5 in order to show all the peak intensities as clearly as possible. The same increase in peak intensity for chnw can be

seen for these FTIR spectra as the chnw loading is increased. A slight increase can also be seen for the peak at approximately 3000 cm^{-1} mainly belonging to the HiPP matrix. This could be caused by the addition of PPGMA, with the polypropylene portion adding to the peak intensities.

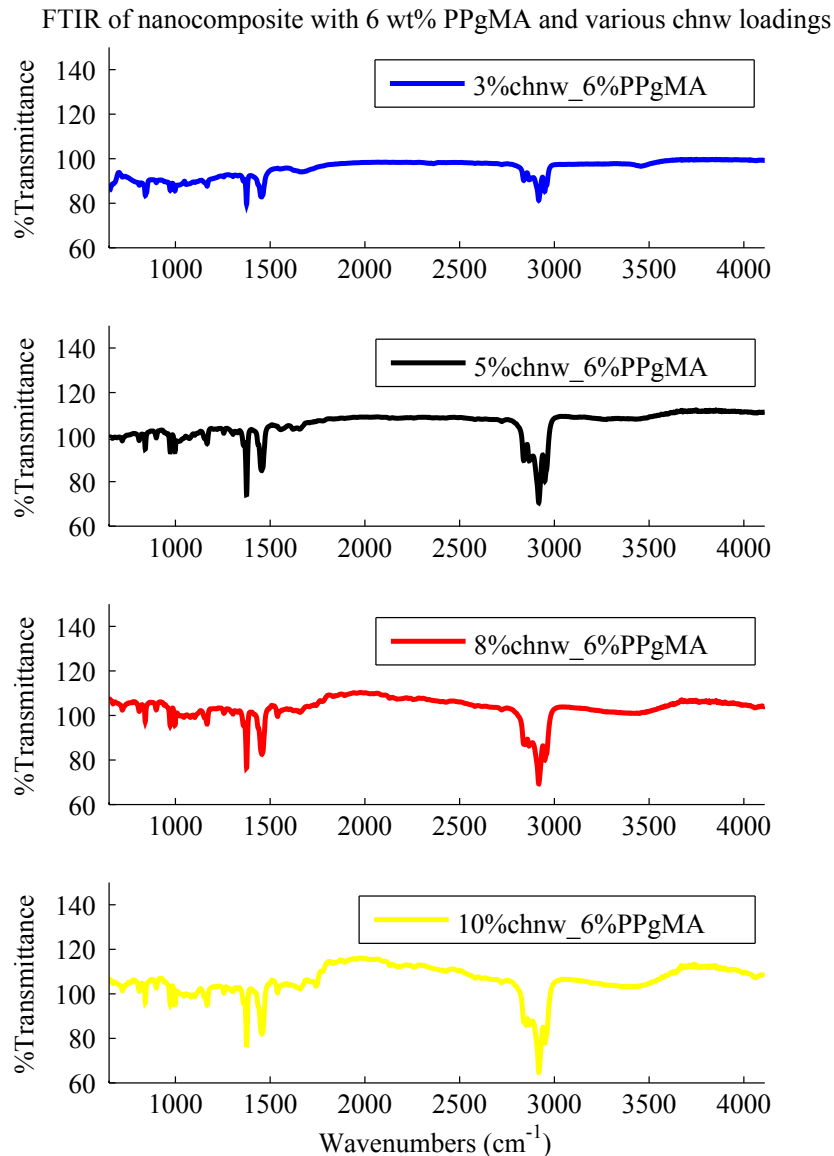


Figure 5.6: FTIR spectra of nanocomposites consisting of the HiPP matrix, 6 wt% PPGMA and varying chnw loadings.

Figure 5.6 shows further increase of the intensity of the peaks belonging to chnw as the loading increases. The peaks correlating to the polypropylene fractions of the HiPP as well as PPGMA also increase because of the higher content of PPGMA.

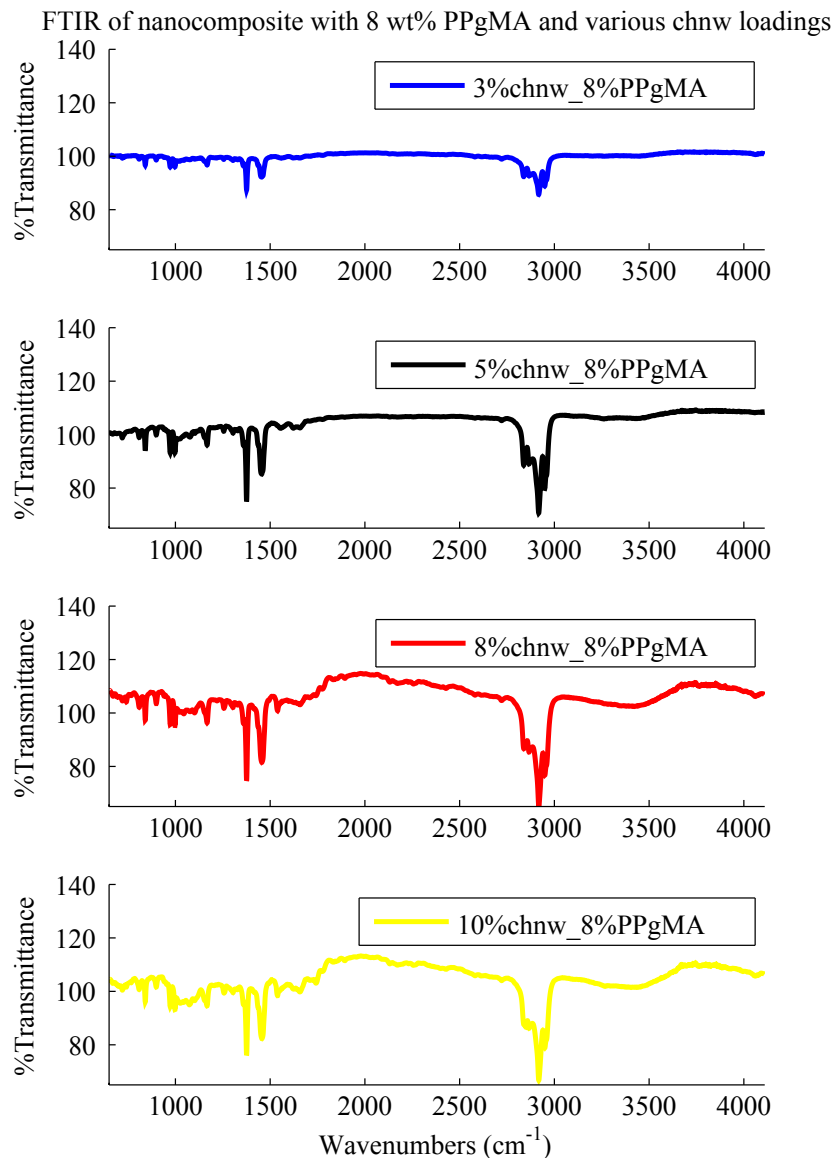


Figure 5.7: FTIR spectra of nanocomposites consisting of the HiPP matrix, 8 wt% PPGMA and varying chnw loadings.

The same results as stated before can be seen for Figure 5.7 and 5.8. The increase in the polypropylene peak intensity at approximately 1700 cm^{-1} and 1800 cm^{-1} as well as 3000 cm^{-1} is due to the increasing load of PPGMA in the nanocomposite. The amide moiety peaks for chnw also becomes more visible as the chnw content increases.

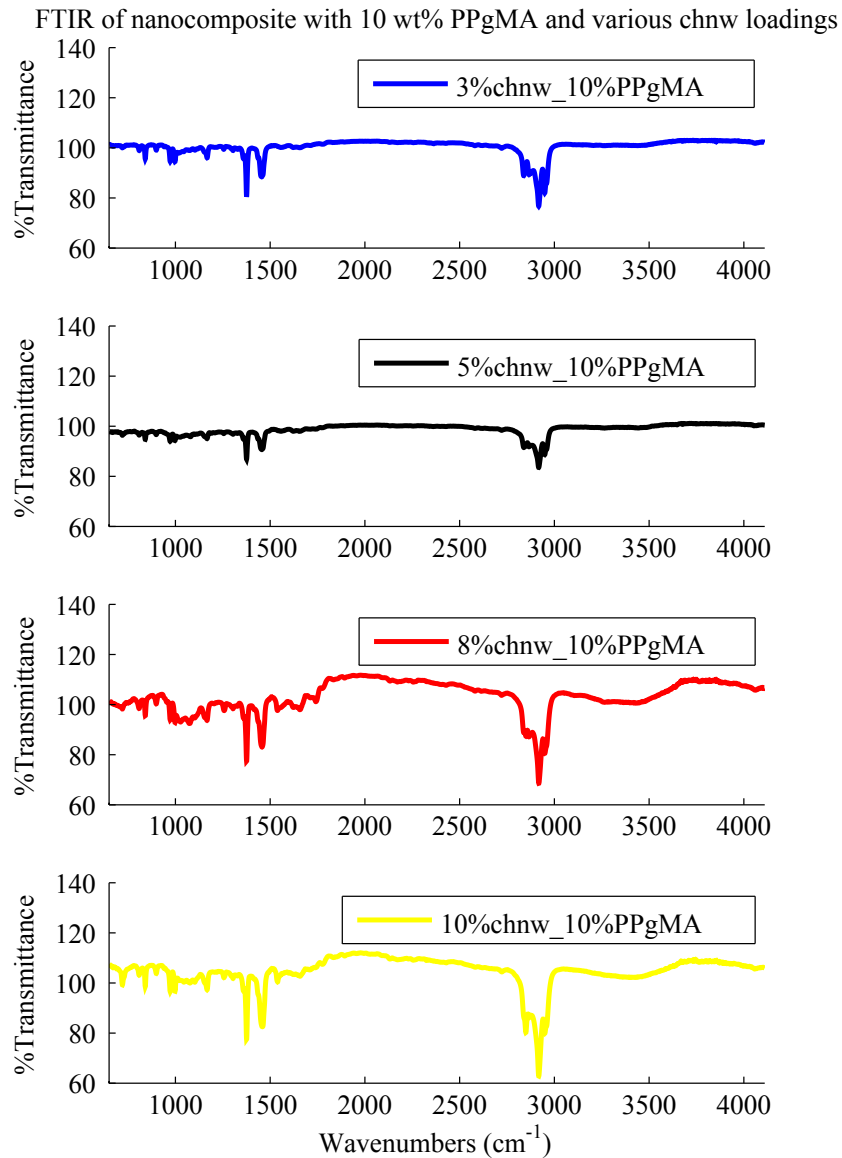


Figure 5.8: FTIR spectra of nanocomposites consisting of the HiPP matrix, 10 wt% PPgMA and varying chnw loadings.

5.3 Differential scanning calorimetry analysis (DSC)

The differential scanning calorimetry analysis is at constant pressure so the change in heat flow is purely connected to the changes in enthalpy for the nanocomposites [8]. The change in heat flow (difference between reference pan and sample pan) can be negative or positive depending on the type of processes that may occur within the nanocomposites. Endothermic processes such as decomposition reactions give a positive change in heat flow. Crystallization and other types of exothermic processes causes a negative change in heat flow [8].

High impact polypropylene is a general purpose injection molding grade and is therefore suitable for use under high temperatures. It is therefore important that these favorable thermal properties are not negatively affected by the incorporation of chnw. The thermal properties of the nanocomposite appear to remain greatly unchanged compared to the HiPP matrix. Figures 5.9 to 5.12 illustrate the DSC curves for all nanocomposite samples containing chnw and PPgMA.

The percentage crystallinity of each sample was determined by using equation (5.1) where the $\Delta H_{100\%}$ for polypropylene is 207 J/g.

$$\%Crystallization = \frac{\Delta H}{\Delta H_{100\%}} \cdot (100) \quad (5.1)$$

Table 5.1 shows the melting temperatures of the nanocomposites with various chnw and PPgMA content. A slight decrease in the melting temperature can be seen for the nanocomposites containing no compatibilizer. The nanocomposites containing 3 wt% chnw and increasing PPgMA content showed an slight decrease in melting temperature. There is not exactly a trend that can be seen for the 5 wt% chnw with PPgMA inside HiPP. The nanocomposites containing 5 wt% chnw show an increase at lower PPgMA content and then a decrease as PPgMA content is increased to 6 wt% PPgMA. The melting temperature lowers slightly more significantly for the nanocomposites containing 8 wt% chnw and a increasing PPgMA content. The polypropylene regions of the PPgMA seem to have an influence on the HiPP matrix causing the lowered melting temperature. The nanocomposite containing 10 wt% chnw showed a general decrease in the melting temperature as the PPgMA loading is increased. The melting temperature for the nanocomposite sample containing 8 wt% and 10 wt% chnw with 2 wt% PPgMA presented a similar melting temperature peak as seen for HiPP at approximately 165 °C.

Table 5.1: Melting points ($^{\circ}\text{C}$) of HiPP/chnw (PPgMA) nanocomposites where 0 wt% chnw and 0 wt% PPgMA indicates clean HiPP.

wt% chnw	T_m ($^{\circ}\text{C}$)					
	0%PPgMA	2%PPgMA	4%PPgMA	6%PPgMA	8%PPgMA	10%PPgMA
0	165.8					
3	163.7	163.7	163.7	163.3	163.6	163.1
5	163.6	164.5	164.0	163.4	163.1	163.2
8	164.0	165.2	163.6	161.6	162.3	162.1
10	164.0	165.1	162.8	162.4	163.0	162.1

Table 5.2 shows the crystallization percentage of the nanocomposites with various chnw and PPgMA content. The percentage of crystallization are much lower for nanocomposite samples containing no compatibilizer. It tends to decrease as the chnw content is increased. The percentage of crystallization appears to decrease for a nanocomposite sample with a chnw loading of 3 wt% chnw and low PPgMA content up to 4 wt%. The crystallization percentage increase above PPgMA loadings of 6 wt% PPgMA. The largest percentage crystallization for the nanocomposites containing 3 wt% can be seen in the combination with 10 wt% PPgMA. Nanocomposites containing 5 wt% chnw with increasing PPgMA content indicates a higher percentage of crystallization overall compared to a clean HiPP sample. The highest change in percentage crystallization can be seen for the nanocomposite sample containing 5 wt% chnw and 10 wt% PPgMA. The nanocomposites containing 10 wt% chnw showed an increased percentage of crystallization upon the addition of 2 wt% PPgMA, then a decrease could be seen as the PPgMA load was increased up to 6 wt%. The percentage crystallization increased for higher PPgMA loadings of 8 wt% and 10 wt% combined with lower chnw loadings.

Table 5.2: Percentage crystallization (%) of HiPP/chnw (PPgMA) nanocomposites where 0 wt% chnw and 0 wt% PPgMA indicates clean HiPP.

wt% chnw	% Crystallization					
	0%PPgMA	2%PPgMA	4%PPgMA	6%PPgMA	8%PPgMA	10%PPgMA
0	42.5					
3	40.0	39.4	34.2	39.8	42.5	42.1
5	37.0	43.7	42.1	55.4	46.6	49.7
8	37.1	43.2	37.6	38.7	42.8	36.3
10	37.1	43.3	39.4	35.0	41.6	44.2

There appears to be an overall slight increase in crystallization for nanocomposites containing higher PPgMA loadings and lower chnw loadings. Chitin nanowhiskers can act as a nucleating agent. This means that chnw can form smaller crystals within the ma-

trix. These smaller crystals can have lower melting points thus influencing the melting temperature of the HiPP matrix. There are however also some decrease in crystallization witnessed within the table for the nanocomposites containing lower PPgMA content and low chnw loadings. This lowering of the percentage crystallization can be caused by the chnw containing trace amounts of acid even after careful dialysis. The presence of acid can cause oxidative degradation that can result in changes in the chemical composition of chnw which in turn can result in the loss of alcohol groups that lowers the amount of hydrogen bonding between the chains. Chitin nanowhiskers can also prevent polymer chains from crystallizing because of the interference that can be caused by aggregated chnw within the HiPP matrix [1].

The changes that was illustrated in the Tables 5.1 and 5.2 for the nanocomposites containing various loadings of PPgMA and chnw are also presented in Figure 5.9 to 5.12. The crystallization percentage shows vertical shifting compared to the peaks for a clean HiPP sample as can be seen in all the DSC thermograms. The melting temperature of the melting peaks for the nanocomposites remain relatively the same as for clean HiPP.

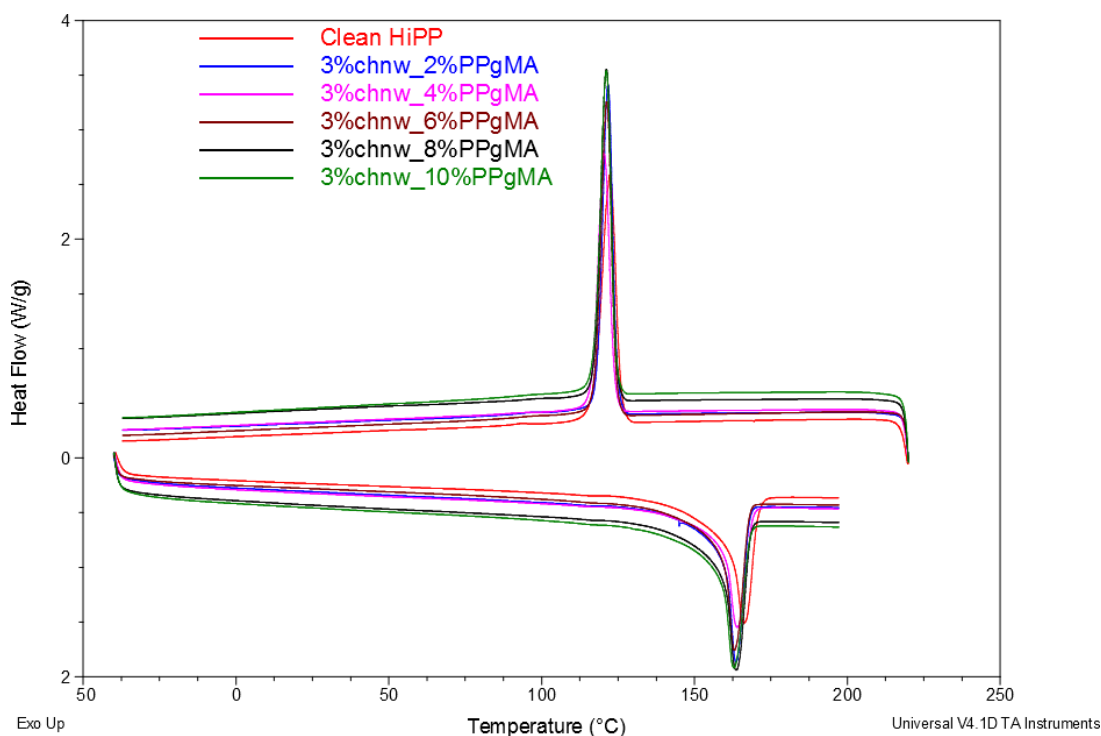


Figure 5.9: DSC thermograms showing the effect that various wt% PPgMA and 3 wt% chnw have on the HiPP matrix.

The presence of the chnw within the HiPP matrix appear to enhance the crystallinity of the nanocomposites slightly which can explain the change in heat flow compared to a clean HiPP sample. Figure 5.9 shows that the nanocomposites with low chnw loadings

and high PPgMA content have increased crystallization peaks compared to the nanocomposites samples with low chnw loadings and low PPgMA loadings.

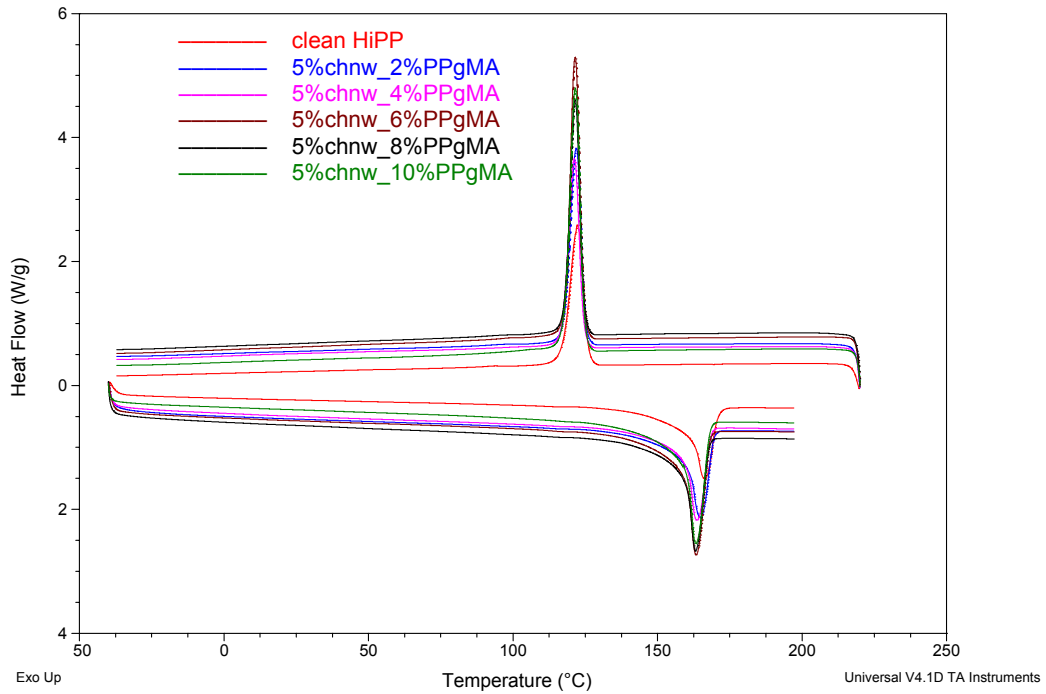


Figure 5.10: DSC thermograms showing the effect that various wt% PPgMA and 5 wt% chnw have on the HiPP matrix.

A increase in the crystallization peak can be seen for nanocomposites containing 6, 8 and 10 wt% PPgMA and a chnw loading of 5 wt% as presented in Figure 5.10. The rest of the nanocomposites containing PPgMA loadings of 2 wt% and 4 wt% have a lower crystallization peaks compared to the other nanocomposites. The highly crystalline chnw enhances the crystallinity because of the small crystals that form within the HiPP matrix.

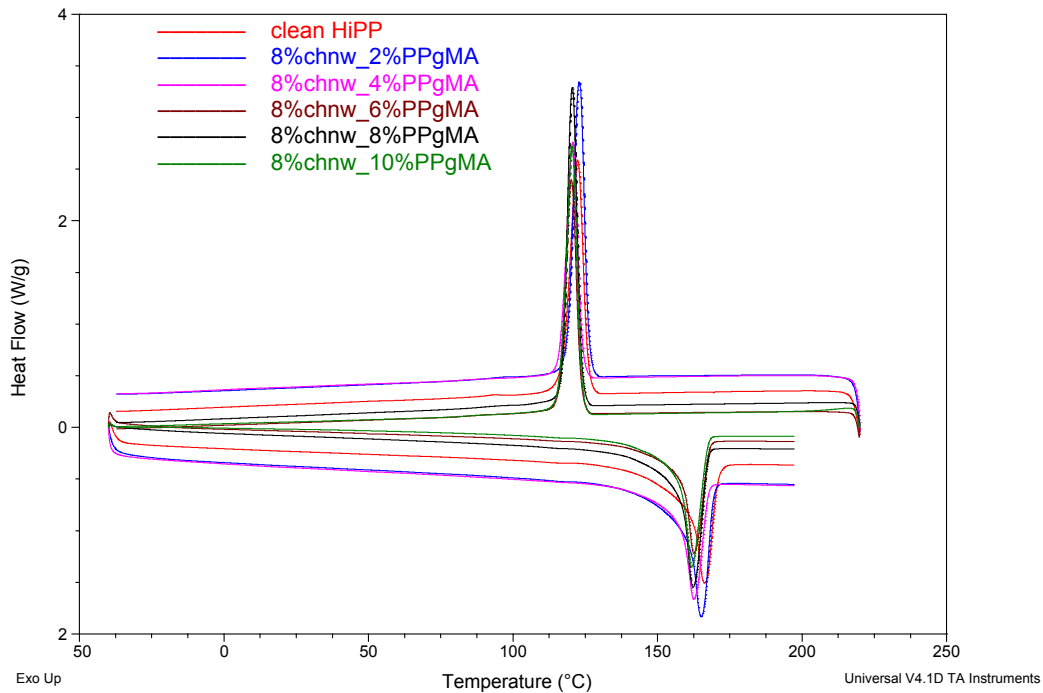


Figure 5.11: DSC thermograms showing the effect that various wt% PPgMA and 8 wt% chnw have on the HiPP matrix.

Similar results can be seen for the DSC thermogram in 5.11. Nanocomposites containing high amounts of chnw combined with low loadings of PPgMA, such as seen for the nanocomposite sample containing 8 wt% chnw and 2 wt% PPgMA, shows a larger increase in the crystallization peak compared to a clean HiPP sample. The nanocomposite sample containing 8 wt% chnw and 8 wt% PPgMA shows a high increase in percentage crystallization. This increase in crystallization can be caused by the irregular distribution of chnw on a molecular level within the nanocomposite sample caused by the aggregation that occur within the nanocomposite at high chnw loadings combined with a high PPgMA load. It was therefore possible that the samples used for the DSC analysis of the nanocomposite containing 8 wt% PPgMA and 8 wt% chnw consist of irregular distributed clusters of chnw which caused the increase in the crystallization peak.

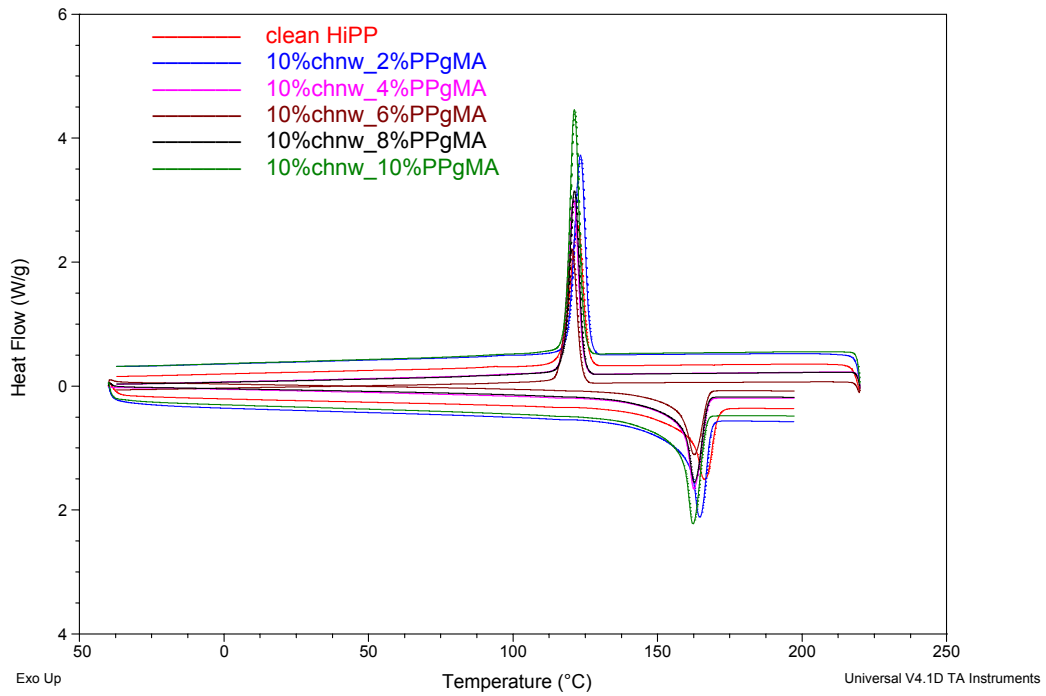


Figure 5.12: DSC thermograms showing the effect that various wt% PPGMA and 10 wt% chnw have on the HiPP matrix.

Figure 5.12 presented an increase in crystallization peaks for nanocomposites containing high chnw loadings and lower PPGMA loadings. The exception can be seen for nanocomposite samples containing 10 wt% chnw and 10 wt% PPGMA. Agglomeration occur between the chnw because of the high chnw loading, but the chnw content is so high that some interaction between the extremely high PPGMA content and the chnw must occur forcing some interaction between the chnw and the HiPP matrix.

5.4 Thermogravimetric analysis (TGA)

Figure 5.13 presents the TGA curves for the individual components used in the preparation of the nanocomposites. The weight loss of chnw appears to be immediate, and this can be due to the loss of moisture. This loss of moisture continues up to approximately 60 °C where after it seems to stabilize for a time. The weight loss then starts to increase significantly at 280 °C and begins to even out at approximately 470 °C [1].

Degradation for PPgMA occurs at about 144 °C and continues more rapidly at 380 °C until it reaches 100% weight loss at approximately 480 °C. High impact polypropylene has weight loss commencing at about 288 °C and rapidly increases at 400 °C until it reaches complete degradation at 500 °C. Similar results can be seen for all the nanocomposites with a slight increase of the temperature where it reaches 100% weight loss.

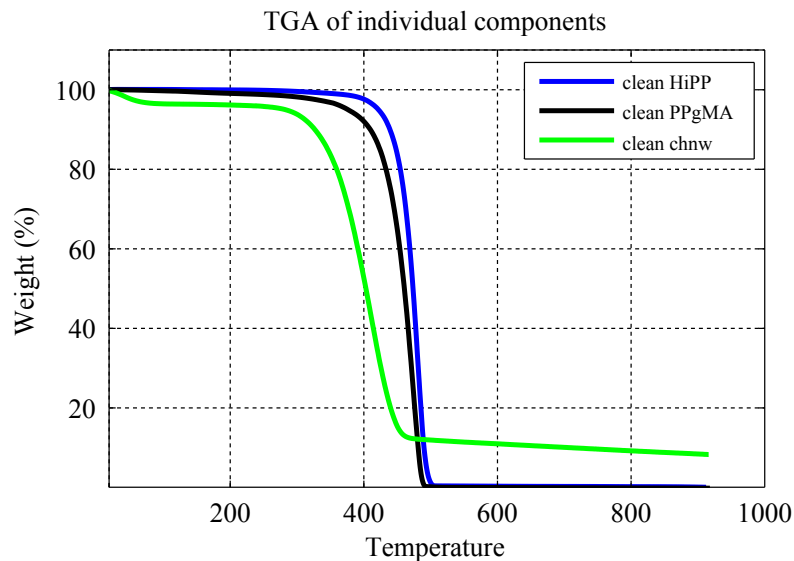


Figure 5.13: TGA curves of the individual components used in the preparation of the nanocomposites.

The thermogravimetric analysis results for the nanocomposites containing chnw and PPgMA were shown in Figure 5.14 to 5.18. Figure 5.14 presents the TGA results for 2 wt% PPgMA with various chnw loadings. The onset temperature does not seem to change significantly for the nanocomposites samples containing 2 wt% PPgMA and low chnw loadings. The slope of the TGA curves for higher chnw content with 2 wt% PPgMA appear to become slightly less steep indicating a small improvement in the thermal stability of the nanocomposite compared to clean HiPP.

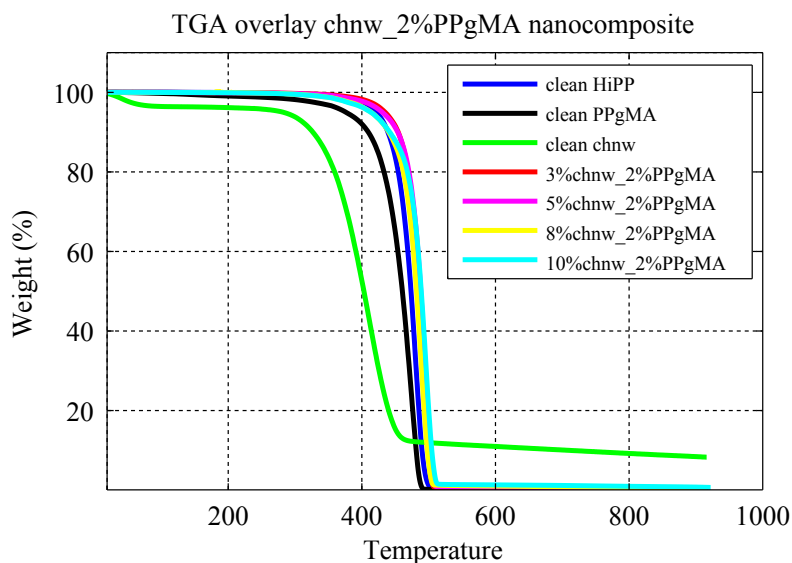


Figure 5.14: TGA curves overlaid to show the change in onset and maximum temperature during incorporation of various chnw loadings with 2 wt% PPgMA into HiPP matrix compared with neat samples of HiPP, chnw and PPgMA.

Figure 5.15 shows nanocomposite samples containing 3 - 5 wt% chnw with 4 wt% PPgMA that present a onset of degradation and overall weight loss at the same temperatures as that for the clean HiPP sample. The nanocomposite sample containing chnw loading of 8 and 10 wt% shows a slight increase in the onset of the degradation temperature as compared to the clean HiPP sample.

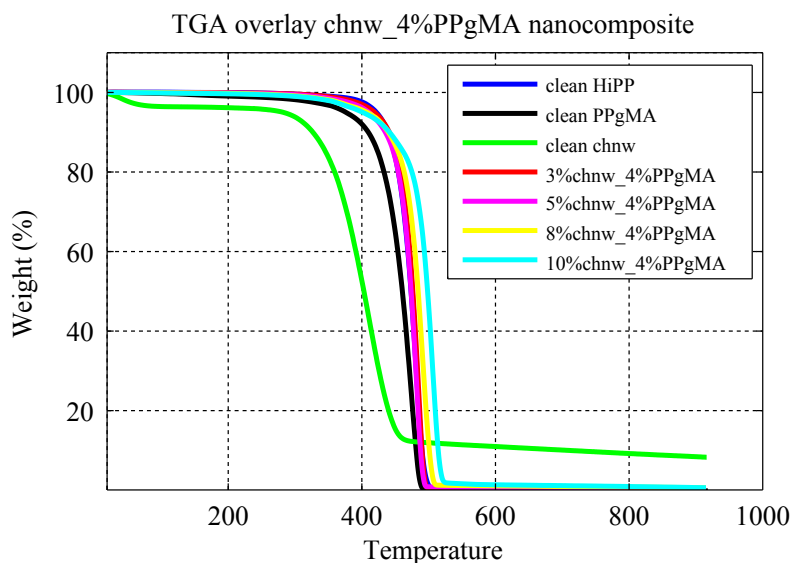


Figure 5.15: TGA curves overlaid to show the change in onset and maximum temperature during incorporation of various chnw loadings with 4 wt% PPgMA into HiPP matrix compared with neat samples of HiPP, chnw and PPgMA.

The nanocomposites containing 6 wt% PPgMA are illustrated in Figure 5.16. An improvement of thermal stability of the nanocomposite containing a higher loading of chnw such as seen for 8 and 10 wt% chnw can be seen in combination with a loading of 6 wt% PPgMA. Complete weight loss of the nanocomposite occurs at a higher temperature as that which can be seen for a clean sample of HiPP.

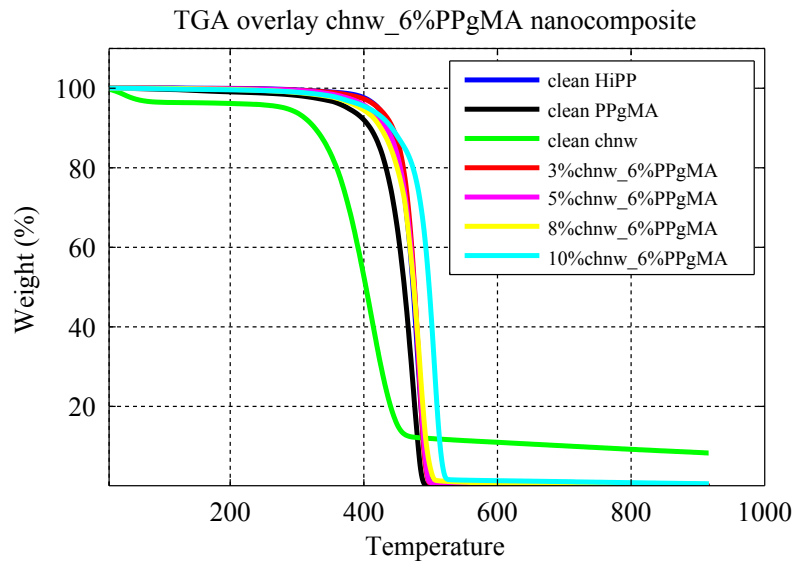


Figure 5.16: TGA curves overlayed to show the change in onset and maximum temperature during incorporation of various chnw loadings with 6 wt% PPgMA into HiPP matrix compared with neat samples of HiPP, chnw and PPgMA.

Figure 5.17 presents the nanocomposites containing 8 wt% PPgMA and varying chnw loading. The thermal degradation properties appear to be similar to that of the clean HiPP sample except for the 8 and 10 wt% chnw loadings. A steep initial weight loss can be seen for chnw loading of 8 wt% and 8 wt% PPgMA causing the further weight loss at approximately 50 °C to be lower than that for the clean HiPP sample. This could be caused by possible aggregation of chnw within the nanocomposite. Agglomeration of the chnw can cause the interaction between the PPgMA and the HiPP matrix to be hindered. The nanocomposite sample with 10 wt% chnw content have a weight loss at a higher temperature than all the other composites containing 8 wt% PPgMA along with the clean HiPP sample.

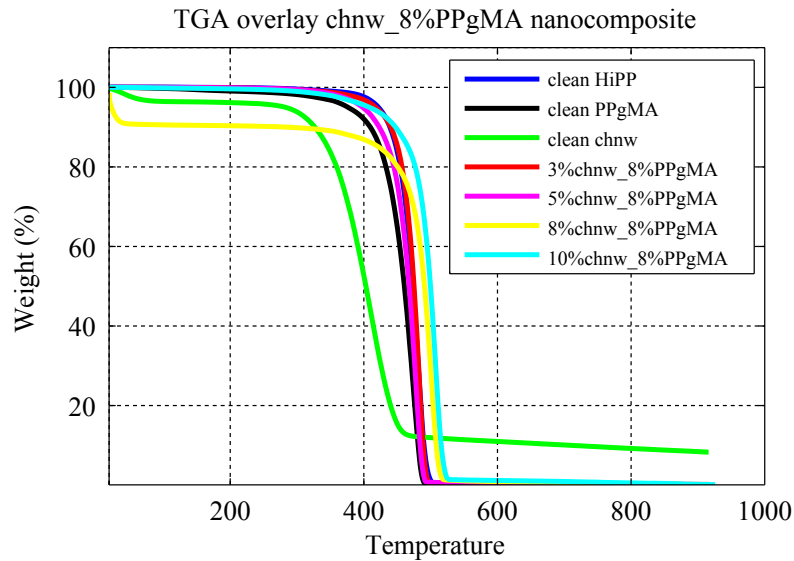


Figure 5.17: TGA curves overlaid to show the change in onset and maximum temperature during incorporation of various chnw loadings with 8 wt% PPgMA into HiPP matrix compared with neat samples of HiPP, chnw and PPgMA.

Figure 5.18 presents the nanocomposites containing 10 wt% PPgMA and varying chnw loading. Similar thermal degradation properties appear can be seen to that of a clean HiPP sample. The nanocomposites containing 8 and 10 wt% chnw loadings combined with 10 wt% PPgMA shows an increase in the onset of degradation temperature.

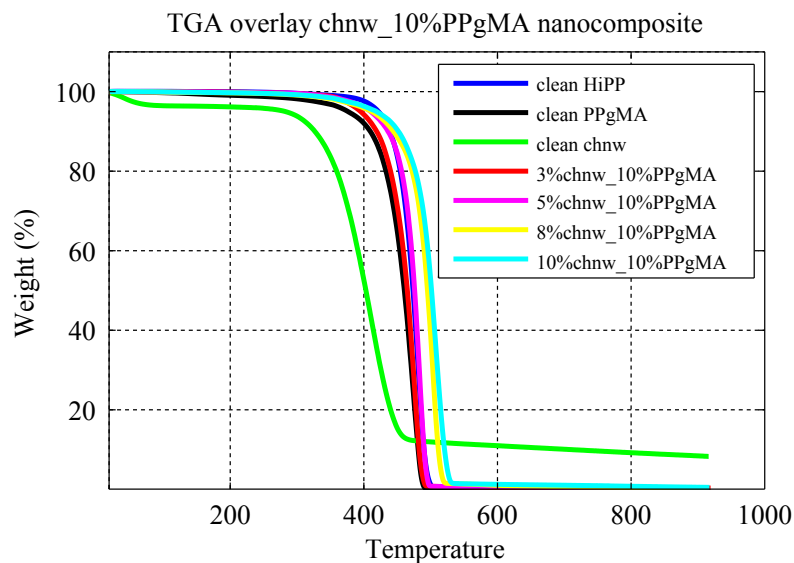


Figure 5.18: TGA curves overlaid to show the change in onset and maximum temperature during incorporation of various chnw loadings with 10 wt% PPgMA into HiPP matrix compared with neat samples of HiPP, chnw and PPgMA.

The onset of the degradation temperatures for the nanocomposites are summarized in Table 5.3 and 5.4. Only these nanocomposites were shown to get an overall view of the thermal stability of the nanocomposites since the results were very similar as seen in the TGA curves presented above. It is apparent in Table 5.3 that the weight loss of the nanocomposites occurs at relatively the same temperatures as seen for a clean HiPP sample. The increase in chnw can cause dispersion of the chnw within the matrix to become poor and this can lessen the effect the chnw have on the thermal stability of the nanocomposite. Table 5.4 shows how the increase in PPgMA affects the onset of degradation temperature of the nanocomposite in a positive manner. Although as mentioned earlier in this section, the thermal stability for the nanocomposites does not seem to be greatly affected or changed compared to a clean HiPP sample which is favorable.

Table 5.3: TGA onset degradation temperature and weight loss percentage of nanocomposites with various chnw loadings and 2 wt% PPgMA.

Sample	Onset degradation Temperature (°C)	Onset (weight%)
clean HiPP	289.0	99.7
clean chnw	277.1	94.2
clean PPgMA	144.0	99.6
3%chnw_2%PPgMA	318.3	99.4
5%chnw_2%PPgMA	319.9	99.4
8%chnw_2%PPgMA	316.9	99.4
10%chnw_2%PPgMA	309.8	99.5

Table 5.4: TGA onset degradation temperature and weight loss percentage of nanocomposites with various chnw loadings and 10 wt% PPgMA.

Sample	Onset degradation Temperature (°C)	Onset (weight%)
clean HiPP	289.0	99.7
clean chnw	277.1	94.2
clean PPgMA	144.0	99.6
3%chnw_10%PPgMA	270.8	98.4
5%chnw_10%PPgMA	286.1	98.1
8%chnw_10%PPgMA	289.0	99.7
10%chnw_10%PPgMA	292.11	99.64

5.5 Tensile testing

Tensile testing was done on each nanocomposite as described in Section 3.7.6 in order to obtain necessary information about the changes in the mechanical properties of the HiPP matrix caused by the chnw as fillers. Information such as the Young's modulus,

maximum tensile strength, stress before compensation and elongation at break were all accumulated during analysis.

Stress-strain curve overlays of the different HiPP/chnw nanocomposites synthesized with various loadings of PPgMA as compatibilizer are shown in Figures 5.21 to 5.29. Stress-strain curve overlays were used to compare how the various concentrations of PPgMA within the nanocomposites influenced the interaction between the chnw and HiPP matrix. The stress-strain curves also illustrate how the mechanical properties were affected by the incorporation of different loadings of chnw and PPgMA. Polypropylene-*graft*-maleic anhydride does contribute to the improvement of the Young's modulus of the HiPP matrix as seen in Figure 5.19 without the presence of chnw in the matrix. The maximum tensile strength appears to improve at low PPgMA loading compared to a clean sample of HiPP but the Young's modulus remained greatly unchanged.

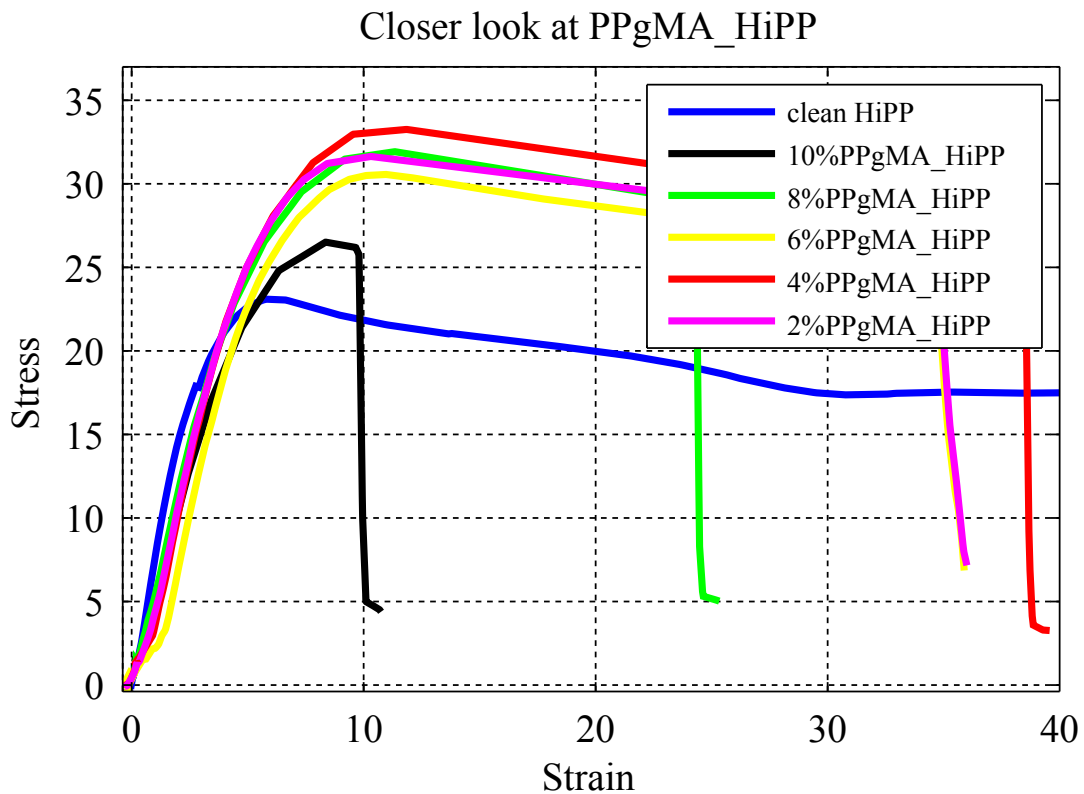


Figure 5.19: Stress-strain curves showing composites containing no chnw and only HiPP and PPgMA

A slight decrease in the maximum tensile strength occurs after PPgMA loading is increased to 6 wt%. At very high PPgMA content, the maximum stress was lowered severely and the extension before compensation of the HiPP matrix compared to clean HiPP were significantly diminished [9]. The largest decrease in maximum tensile strength can be seen for the nanocomposite that contains 10 wt% PPgMA. The interaction between the PPgMA and the HiPP matrix can cause deformation in the isotactic polypropylene portion of the HiPP matrix which is more crystalline and can cause the increase in maximum tensile strength [2].

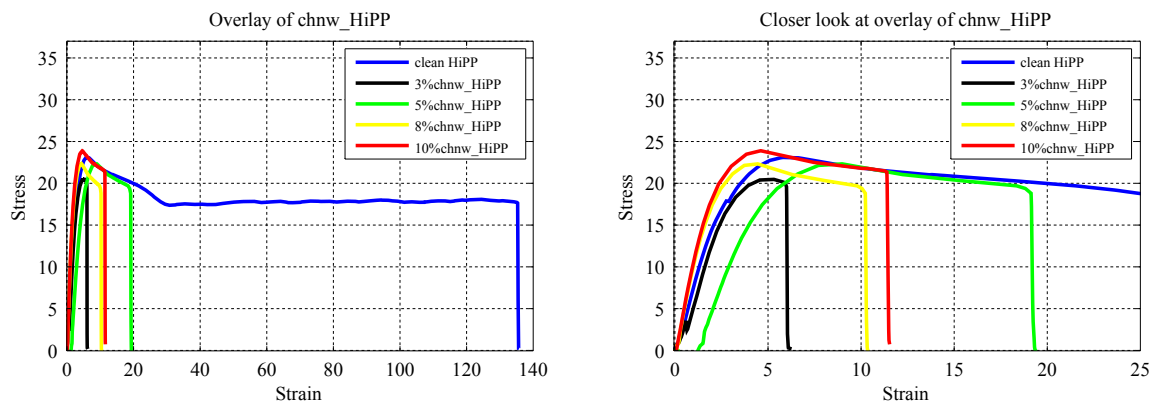


Figure 5.20: Stress-strain curves showing composites containing no compatibilizer and only HiPP and chnw

Figure 5.20 presents the nanocomposite containing no compatibilizer. The presence of chnw increase the Young's modulus of the HiPP matrix slightly and causes the HiPP matrix to become less ductile, lowering the elongation at break severely. The results indicate that there is little to no interaction between the chnw and HiPP matrix since the tensile strength appears to result only from the isotactic polypropylene of the HiPP matrix.

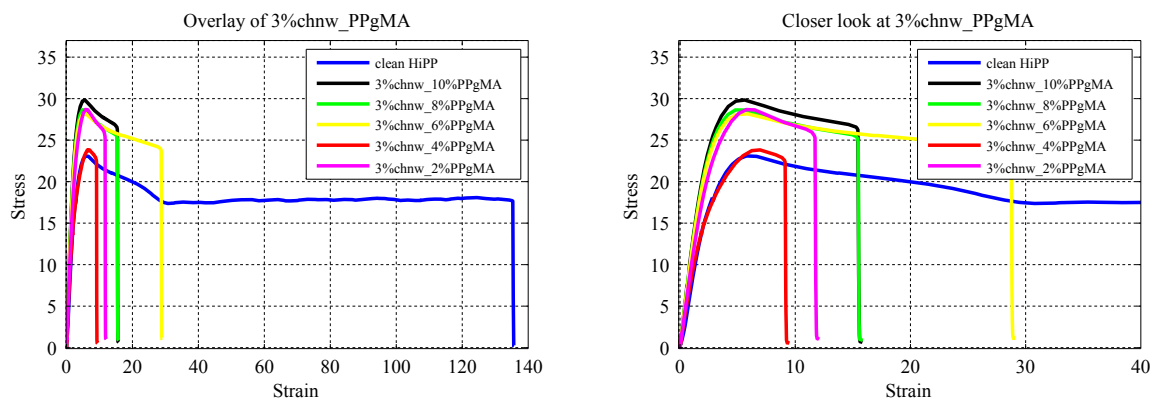


Figure 5.21: Stress-strain curves showing 3% chnw combined with varying PPgMA content within HiPP nanocomposites

The results presented in Figure 5.21 show an increase in the Young's modulus as soon as a PPgMA loading of 2 wt% is added. The Young's modulus increases as the PPgMA load is increased while the chnw content remains at 3 wt%. The highest value for the Young's modulus can be seen for the nanocomposite that contains 10 wt% PPgMA and 3 wt% chnw within the HiPP matrix. Loading of 4 wt% PPgMA appeared to be a poor combination with a chnw loading of 3 wt% which could be caused by poor dispersion of chnw within the PPgMA solution before solvent casting was done which will influence the interaction with the HiPP matrix. The maximum tensile strength decreased slightly compared to the nanocomposites containing no chnw loadings. The largest maximum tensile strength is seen for the 10 wt% PPgMA loaded nanocomposite with 3 wt% chnw. This can be due to good interaction between PPgMA and chnw.

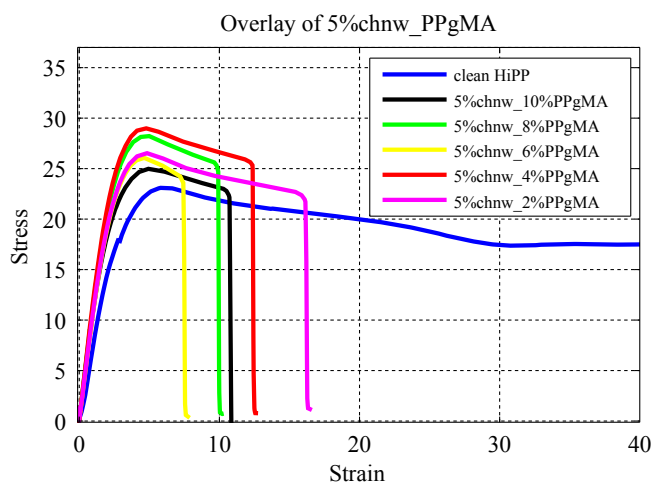


Figure 5.22: Stress-strain curves showing 5%chnw combined with varying PPgMA content within HiPP nanocomposites

Figure 5.22 shows the nanocomposites with 5 wt% chnw content and varying PPgMA content. The maximum tensile strength appears to increase for a PPgMA content of 4 wt% in combination with a chnw loading of 5 wt%. This means that the 5 wt% chnw loading is a good combination with the 4 wt% PPgMA loading and that there is good interaction and dispersion within the nanocomposite sample. The Young's modulus also appears to be greater than the 3 wt% chnw loading with 4 wt% PPgMA content in the previous nanocomposite sample. The maximum tensile strength is lower than compared to the composite sample containing 3 wt% chnw, with the exception of the composite sample containing 3 wt% chnw and 4 wt% PPgMA.

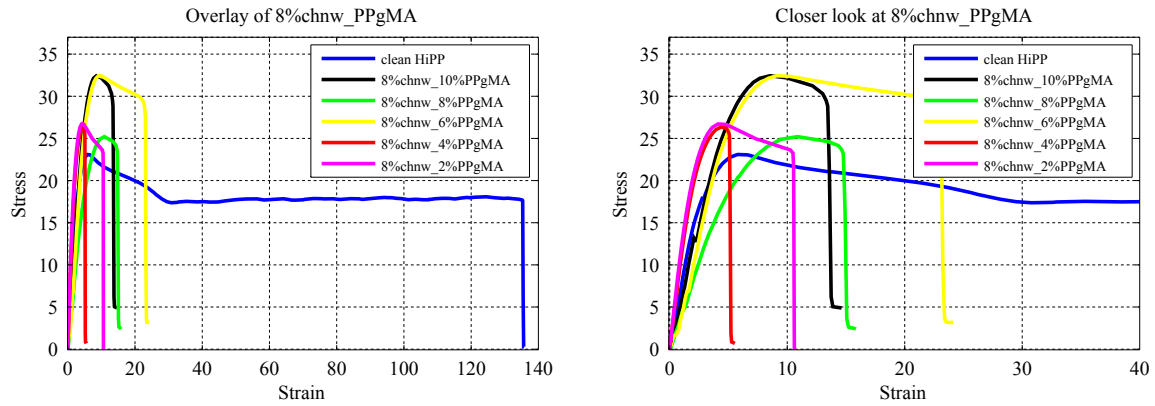


Figure 5.23: Stress-strain curves showing 8%chnw combined with varying PPGMA content within HiPP nanocomposites

The composite sample containing 8 wt% chnw and various loading of PPGMA can be seen in Figure 5.23. The maximum tensile strength for this composite containing a chnw loading of 8 wt% is higher than a clean sample of HiPP. The Young's modulus is much lower for the composite samples containing high loadings of PPGMA with 8 wt% chnw. Improvement of the Young's modulus can be seen as soon as the PPGMA content is lowered to 4 wt% and 2 wt%.

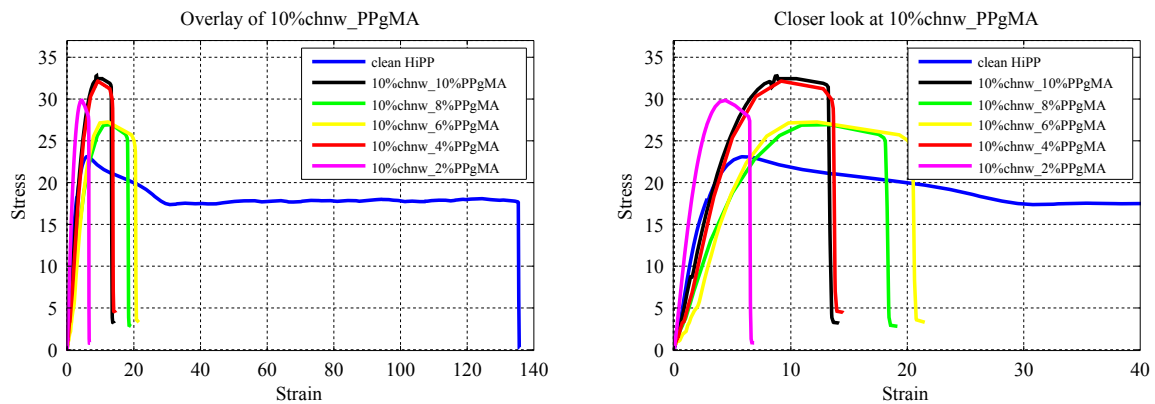


Figure 5.24: Stress-strain curves showing 10%chnw combined with varying PPGMA content within HiPP nanocomposites

Figure 5.24 illustrates the decrease in Young's modulus as the chnw content increase along with the increase of PPGMA content. At the high chnw content of 10 wt%, chnw tend to agglomerate more because of the increasing interaction between the chnw chains. The nanocomposite sample containing 10 wt% PPGMA with 10 wt% chnw shows a slight increase of the Young's modulus due to forced interaction between the PPGMA and chnw at such high loadings. It is possible, however, that for the rest of the nanocomposites containing high PPGMA and chnw loadings, the solution during solvent casting becomes too viscous. This increase in viscosity of the solution causes agglomeration of chnw and

less interaction with the PPgMA which leads to poor compatibility with the HiPP matrix. This explanation could be further justified by the fact that the only nanocomposite with 10 wt% chnw that is above the Young's modulus of HiPP is the nanocomposite sample of 2 wt% PPgMA and 10 wt% chnw.

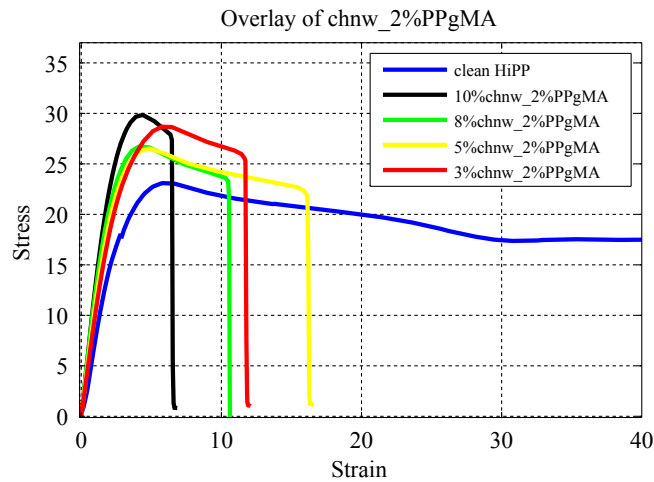


Figure 5.25: Stress-strain curves showing various concentrations of chnw combined with 2%PPgMA within HiPP nanocomposites

All the nanocomposite samples in Figure 5.25 showed a higher Young's modulus than that for a clean HiPP sample with the exception of the nanocomposites containing high chnw and PPgMA loadings. The best tensile properties that can be seen for these nanocomposite samples in Figure 5.25 are the nanocomposites containing 10 wt% chnw and 2 wt% PPgMA. Both the maximum strength and Young's modulus is greater for the nanocomposites containing loadings of 10 wt% chnw and 2 wt% PPgMA. This combination was effective in affording good dispersion and compatibility between the HiPP matrix and chnw. As soon as the PPgMA content becomes too high the increase in viscosity of the solution propagates agglomeration of the chnw.

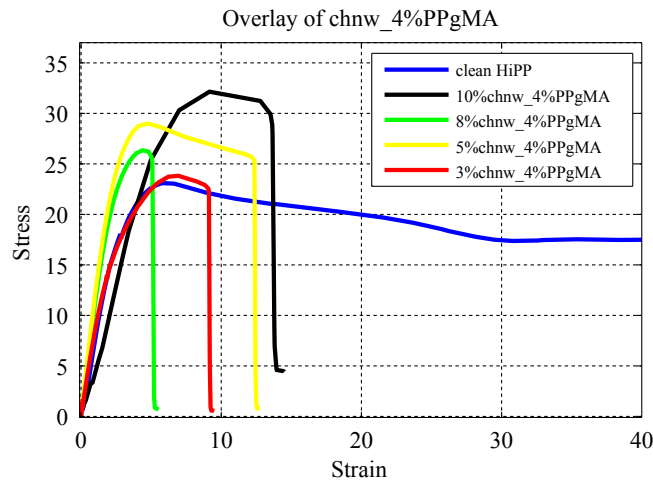


Figure 5.26: Stress-strain curves showing various concentrations of chnw combined with 4%PPgMA within HiPP nanocomposites

Figure 5.26 illustrates a decrease in the Young's modulus for all the nanocomposites that contain 4 wt% PPgMA except the nanocomposite samples containing 5 wt% and 8 wt% chnw. The maximum tensile strength remains relatively above the maximum tensile strength for the clean HiPP sample.

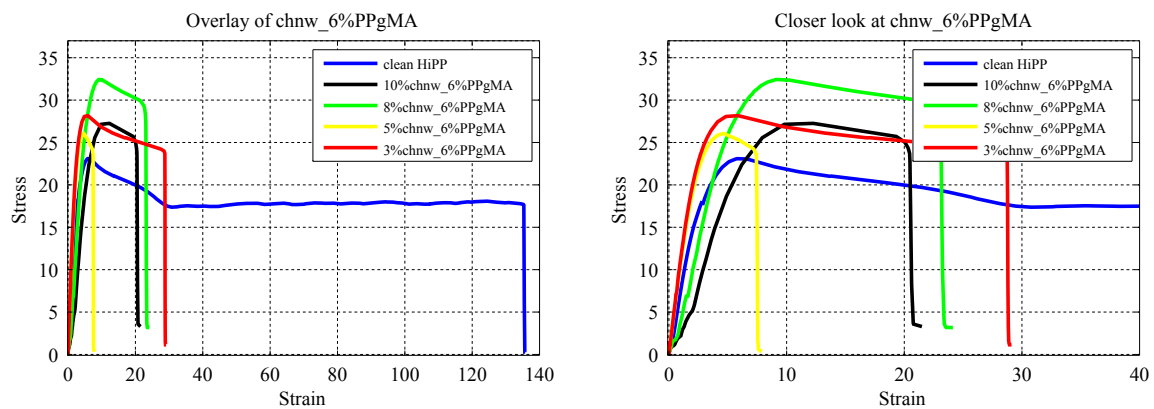


Figure 5.27: Stress-strain curves showing various concentrations of chnw combined with 6%PPgMA within HiPP nanocomposites

Figure 5.27 shows the nanocomposites with loadings of varying chnw and 6 wt% PPgMA. As mentioned previously in Figure 5.25, the increase in PPgMA content can become too much causing an increase in viscosity that forces chnw to aggregate. The nanocomposites with loadings of 6 wt% PPgMA and a high chnw content of 8 wt% and 10 wt% show a clear decline in Young's modulus. This further justifies the explanation that agglomeration of the chnw within a viscous solution have affected the interaction between the chnw and HiPP matrix.

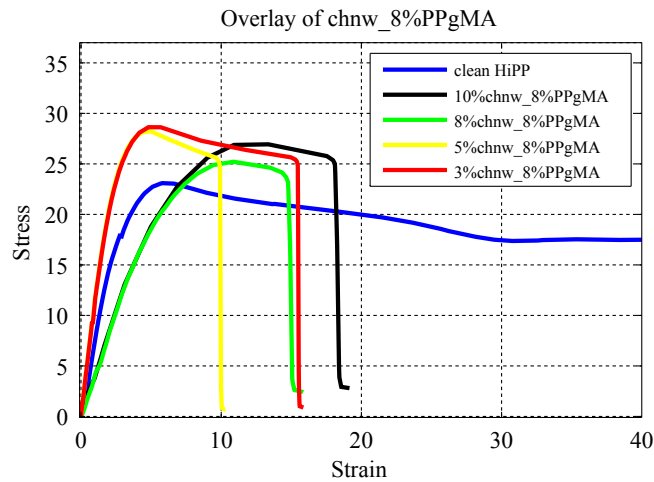


Figure 5.28: Stress-strain curves showing various concentrations of chnw combined with 8%PPgMA within HiPP nanocomposites

The viscous effect of the increase PPGMA and chnw content in solution has a clear influence on the interaction of the nanocomposite as shown in Figure 5.28. The nanocomposites containing 3 wt% and 5 wt% chnw combined with 8 wt% PPGMA show improved Young's modulus and maximum tensile strength. The rest of the composite samples show a decrease in the Young's modulus although the maximum tensile strength remains above that for the clean HiPP sample. The high amount of PPGMA added together with the high chnw content causes agglomeration because the solution becomes too viscous. This agglomeration leads to poor distribution of chnw within the HiPP matrix. Parts of the nanocomposites remain free of chnw and therefore leaves these areas vulnerable to high stress.

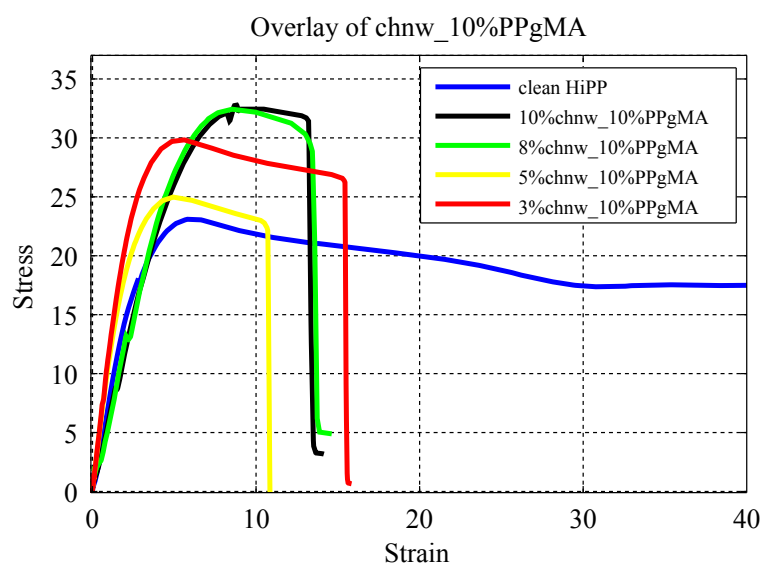


Figure 5.29: Stress-strain curves showing various concentrations of chnw combined with 10%PPgMA within HiPP nanocomposites

The optimum conditions for mechanical improvement appear to be at a high chnw content combined with very low PPgMA content, or low chnw content with a high PPgMA content. These combinations improved the Young's modulus and also the maximum tensile strength but the elongation at break for clean HiPP is dramatically larger compared to the nanocomposite containing chnw and PPgMA.

The maximum extension for a clean sample of HiPP before compensation is 63.33 mm, whereas for 3%chnw_10%PPgMA as seen in Figure 5.29, the extension before compensation is 6.08 mm. Overall the amount of load that can be supported by the nanocomposites are larger than what a sample of clean HiPP can withstand. Clean HiPP supports a load up to approximately 185 N but 3%chnw_10%PPgMA can support a load up to 253 N. A decrease in load support can be seen as the chnw concentration is increased as seen for the nanocomposite sample containing 8 wt% and 10 wt% chnw with 10 wt% PPgMA. An increase in chnw content causes the solution to become extremely viscous and allow agglomeration of the chnw within the HiPP matrix to occur.

The Young's modulus gave an indication of how the chnw affected the tensile properties of the HiPP matrix without compatibilizers added as can be seen in Table 5.5. The average tensile strength for the nanocomposites containing no compatibilizer appears largely unchanged leading to the conclusion that the chnw have extremely poor interaction with the matrix without the help of a compatibilizer. Only the combination of chnw and PPgMA within the HiPP matrix that presented ideal improvement in the Young's modulus and maximum tensile strength were presented in the Tables 5.5 to 5.7 along with the less favorable combinations of the same composite sample.

Table 5.5: Tensile testing data of clean sample HiPP as well as HiPP containing chnw with no compatibilizer

Sample Name	Young's Modulus (MPa)
Clean_HiPP	4.7
3%chnw_HiPP	4.6
5%chnw_HiPP	4.4
8%chnw_HiPP	4.7
10%chnw_HiPP	4.5

The improvement of the hardness of the HiPP matrix is dependent on the interaction between the chnw and the matrix as mentioned earlier. The rubber material distributed within the HiPP matrix and the isotactic polypropylene fractions [2] play a role in this interaction. Even with the presence of PPgMA as compatibilizer, as seen when comparing Tables 5.6 and 5.7 to 5.5, chnw can agglomerate and become poorly distributed within the HiPP matrix when added in higher concentrations. Compatibilizers that are added in

large amounts to a high concentration of chnw in solution can cause agglomeration, since the solution becomes too viscous. This agglomeration of chnw within the viscous solution causes defects within the nanocomposite due to poor distribution. This leaves parts of the matrix free of chnw and therefore much softer [2].

Table 5.6: Tensile testing data of 2 wt% PPgMA with various wt% chnw in HiPP matrix

Sample	Young's Modulus (MPa)
3%chnw_2%PPgMA	8.9
5%chnw_2%PPgMA	9.2
8%chnw_2%PPgMA	10.0
10%chnw_2%PPgMA	11.3

Table 5.7: Tensile testing data of 10 wt% PPgMA with various wt% chnw in HiPP matrix

Sample	Young's Modulus (MPa)
3%chnw_10%PPgMA	10.748
5%chnw_10%PPgMA	8.398
8%chnw_10%PPgMA	5.894
10%chnw_10%PPgMA	5.132

5.6 Conclusion

Fluorescence microscopy only show a very small frame of the nanocomposite because of the nano-scale of the chnw within the HiPP matrix. The images show good dispersion of chnw inside the nanocomposites. Some agglomeration could be seen in some of the fluorescence microscopy imaging frames. These images indicate how difficult achieving good dispersion of chnw within the nanocomposite can be. Fluorescence appears to be a good option for investigating chnw dispersion within a nanocomposite. A fluorescence microscope that has a higher resolution can be more helpful in the investigation of chnw dispersion within the HiPP matrix. The results obtained are not yet conclusive but can be used as a basis for further studies. The infrared spectra showed the presence of the individual components (PPgMA, chnw and HiPP) within the nanocomposites. The peak intensity increased for chnw and the polypropylene fraction on the FTIR spectra as the loading for chnw and PPgMA were increased, respectively.

The DSC curves indicate a overall slight increase in crystallization for nanocomposites containing higher PPgMA loadings and lower chnw loadings. An increase in the crystallization can be seen for loadings containing low PPgMA and high chnw. Some thermal stability is observed with the TGA curves for the nanocomposites when the PPgMA content is increased. At higher chnw loadings the thermal stability becomes similar to that of a clean HiPP sample. This can be explained by the small dimensions of chnw within the HiPP matrix. The small diameter of chnw can cause an absence of chnw in some region of the nanocomposite when the chnw is added in small amounts. The strong hydrogen interactions between the chnw can also interfere with the interaction thereof within the nanocomposite.

It has been seen that the tensile properties of the HiPP matrix can be improved after the incorporation of chnw as nanofiller and PPgMA as compatibilizer. Chitin nanowhiskers can agglomerate and become poorly distributed when added to the HiPP without compatibilizer. As the concentration for PPgMA and chnw increased within the nanocomposite solution, the viscosity increased as could be measured with the naked eye. This caused agglomeration of chnw within the viscous solution and propagated defects inside the nanocomposite due to the poor distribution of chnw within the HiPP matrix. This leaves parts of the HiPP matrix free of chnw and therefore much more vulnerable to stress fractures [2]. The optimum conditions for mechanical improvement appear to be at a high chnw content combined with very low PPgMA loading, or a low chnw loading with a high PPgMA content.

References

- [1] M. Du Toit, "Incorporation of polysaccharide nanowhiskers into a poly (ethylene-co-vinyl alcohol) matrix," p. 1, 2013.
- [2] N. Basson, "The effect of molecular architecture on the properties of propylene impact copolymers." *University of Stellenbosch*, pp. 13–23, 2010.
- [3] H. Mahdavi and M. Nook, "Structure and morphology of a commercial high-impact polypropylene in-reactor alloy synthesized using a spherical ziegler-natta catalyst." *Polymer International*, vol. 59, pp. 1701–1708, 2010.
- [4] J. Karger-Kocsis, *Polypropylene structure, blends and composites: Structure and morphology*, 1st ed. Chapman and Hall, vol. 1.
- [5] M. Dezhu, L. Xiqiang, Z. Ruiyun, H. Kunlun, and L. Xiaolie, "Characteristics of structure of impact polypropylene copolymers of propylene with low ethylene contents," *Chinese Journal of Polymer Science*, vol. 12(2), pp. 169–170, 1994.
- [6] Y. Lu, L. Weng, and L. Zhang, "Morphology and properties of soy protein isolate thermoplastics reinforced with chitin whiskers," *Biomacromolecules*, vol. 5, pp. 1046–1051, 2004.
- [7] M. Rinaudo, *Progress in Polymer Science*, 2006.
- [8] Differential scanning calorimetry: First and second order transitions in polymers. [Online]. Available: www.colby.edu/chemistry/PChem/lab/DiffScanningCal.pdf
- [9] L. Danyadi, T. Janecska, Z. Szabo, G. Nagy, J. Moczo, and B. Pukanszky, "Wood flour filled pp composites: Compatibilization and adhesion," *Composites Science and Technology*, vol. 67(13), p. 2838, 2009.

Chapter 6

Results for HiPP/chnw nanocomposites with EVOH as compatibilizer

Poly(ethylene-co-vinyl alcohol) was used as a second type of compatibilizer to investigate the different effects that different types of compatibilizers can have on the interaction of chnw within the nanocomposites. There were some complications concerning the use of EVOH as a compatibilizer. Solvent casting and injection molding proved to be problematic due to the immiscibility of EVOH in xylene, which was the best solvent required for dissolving HiPP. The solvent that was used for the solution of EVOH and chnw was DMSO, and the use of this solvent also presented problems of its own. Dimethyl sulfoxide does not evaporate very easily from the composite after solvent casting and this effected results during thermal and mechanical analysis. This problem was overcome by choosing a second type of method of chnw incorporation into the HiPP matrix which is known as electrospinning combined with melt pressing. This technique proved much more effective for using EVOH as a compatibilizer during chnw incorporation, making it possible to sidestep the solvent immiscibility problems.

6.1 Solvent casting and injection molding

6.1.1 ATR-FTIR

Infrared spectra of the clean components (EVOH, chnw and HiPP) in the nanocomposite are presented in Figure 6.1. The infrared spectrum for chnw indicates the amide moieties that are the most characteristic peaks for identifying chnw within the nanocomposite. The peaks belonging to the chnw appear at 1580 cm^{-1} , 1625 cm^{-1} and 1662 cm^{-1} and are caused by carbonyl stretching of the amide moieties [1, 2, 3]. Two peaks are visible for HiPP between 1500 cm^{-1} and 1400 cm^{-1} that belong to the polypropylene fraction within HiPP. The polypropylene-portion of HiPP also shows peaks 720 cm^{-1} ascribed to the ethylene sequence [4, 5, 6].

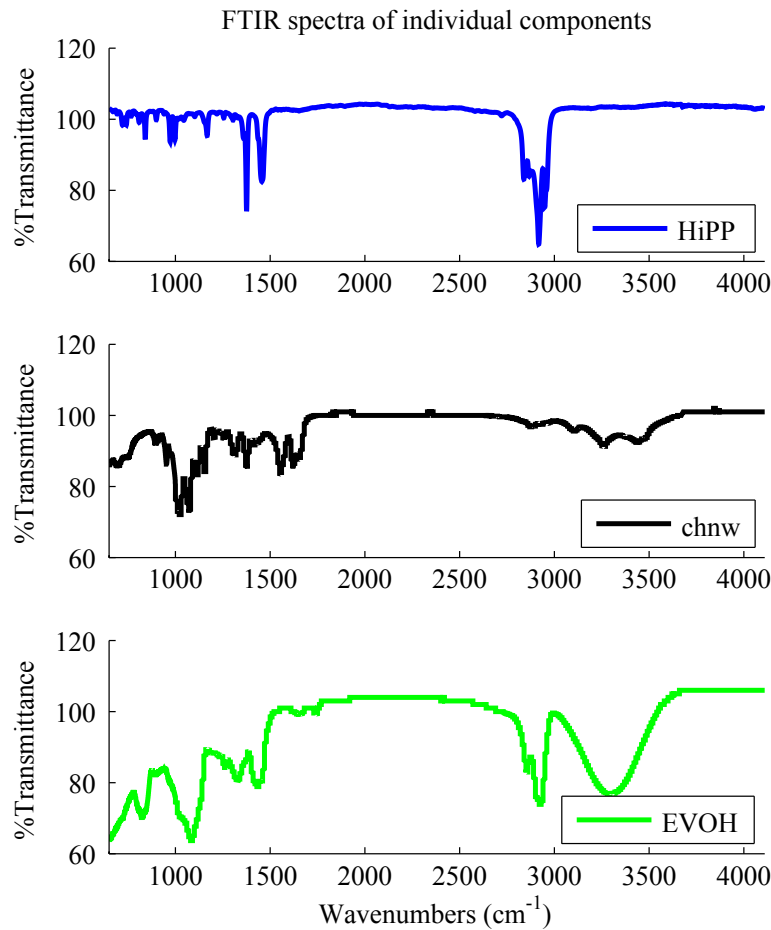


Figure 6.1: FTIR spectra of clean components.

The infrared spectra for EVOH show the absorption bands of the hydroxyl group at 3050 cm^{-1} to 3550 cm^{-1} [7]. Poly(ethylene-*co*-vinyl alcohol) shows peaks also correlating to the PVOH part at 230 cm^{-1} , corresponding to the C=C groups, and at 280 cm^{-1} , corresponding to the C=O groups [8]. The peak corresponding to the CH-stretching vibration within the EVOH can be seen at 2920 cm^{-1} [9]. The band found at 1420 cm^{-1} can both be attributed to saturated CH-groups from the PE component. Some of the peaks seen for HiPP at 2833 cm^{-1} and 2912 cm^{-1} overlap with EVOH making it a little bit more challenging to identify the peaks of HiPP within the nanocomposites.

The nanocomposites containing no EVOH as compatibilizer can be seen in Figure 6.2. The amide moiety peaks at 1580 cm^{-1} , 1625 cm^{-1} and 1662 cm^{-1} for chnw can be seen more clearly as the intensity increases when the chnw loadings are increased.

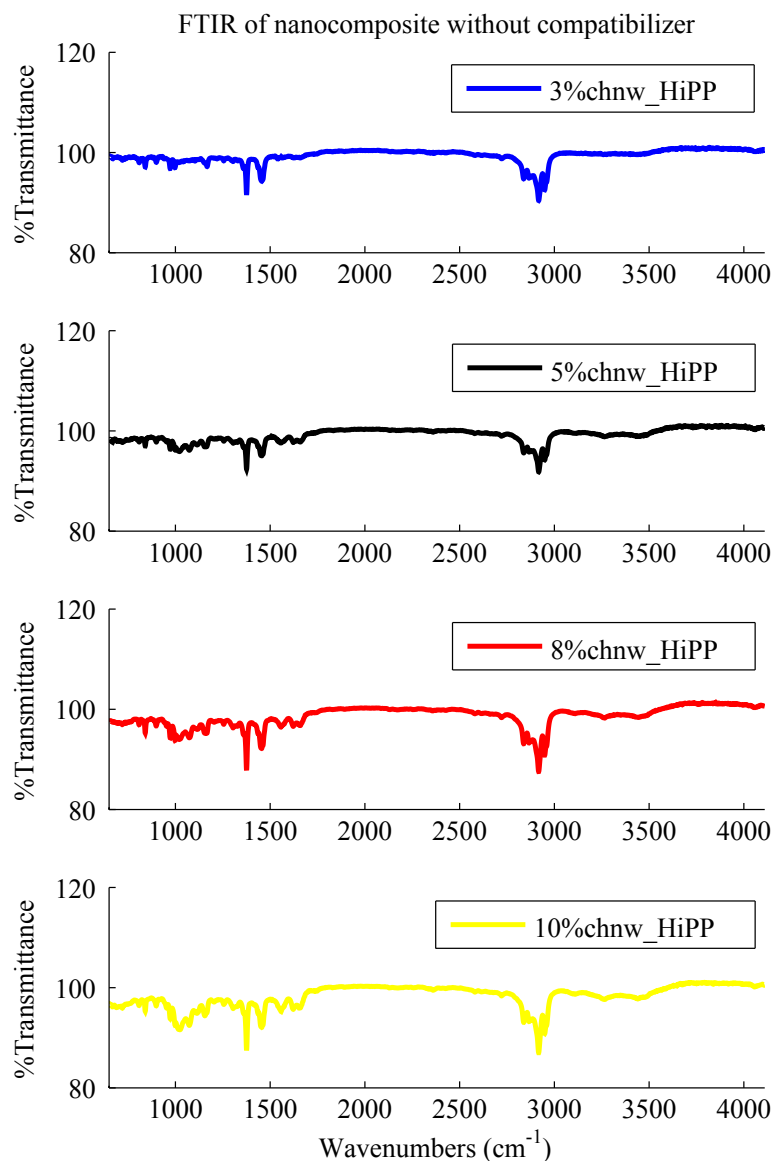


Figure 6.2: FTIR spectra of nanocomposite without compatibilizer.

The spectra of nanocomposites containing various chnw loadings along with 2 wt% EVOH in a HiPP matrix are presented in Figure 6.3. An increase in the chnw peak corresponding to the amide moieties can be seen as expected as the chnw content increases. An increase in the peaks belonging to EVOH can also be seen especially for the absorption band of the hydroxyl group at 3050 cm^{-1} to 3550 cm^{-1} . The increase in intensity can be seen for the higher chnw loading of 10 wt% with a low EVOH content of 2 wt%.

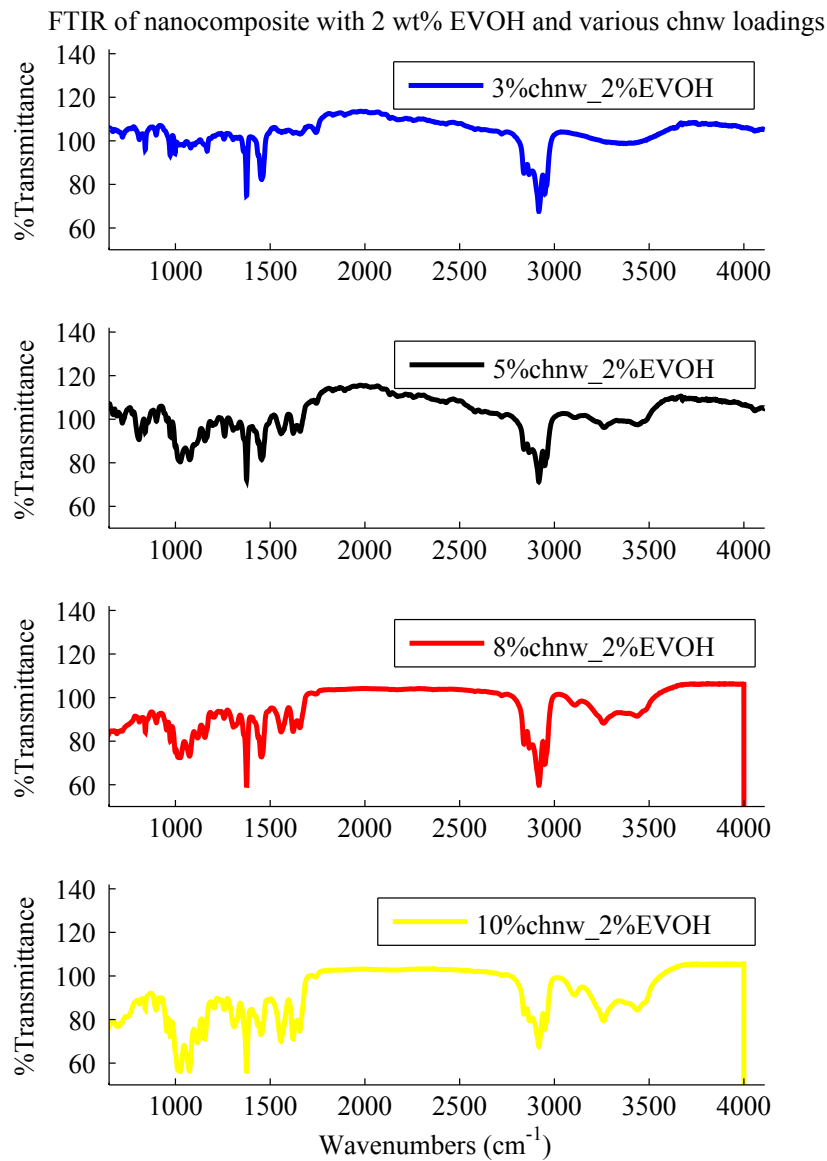


Figure 6.3: FTIR spectra of nanocomposites consisting of the HiPP matrix, 2 wt% EVOH and varying chnw loadings.

Figure 6.4 shows the possible agglomeration of EVOH within the nanocomposite due to the immiscibility that of EVOH in xylene. Irregular increase in the EVOH peak intensity can be seen throughout the nanocomposite samples containing 4 wt% EVOH. A slight increase in the peaks belonging to chnw can be seen, however this increase in the peak intensity also becomes irregular.

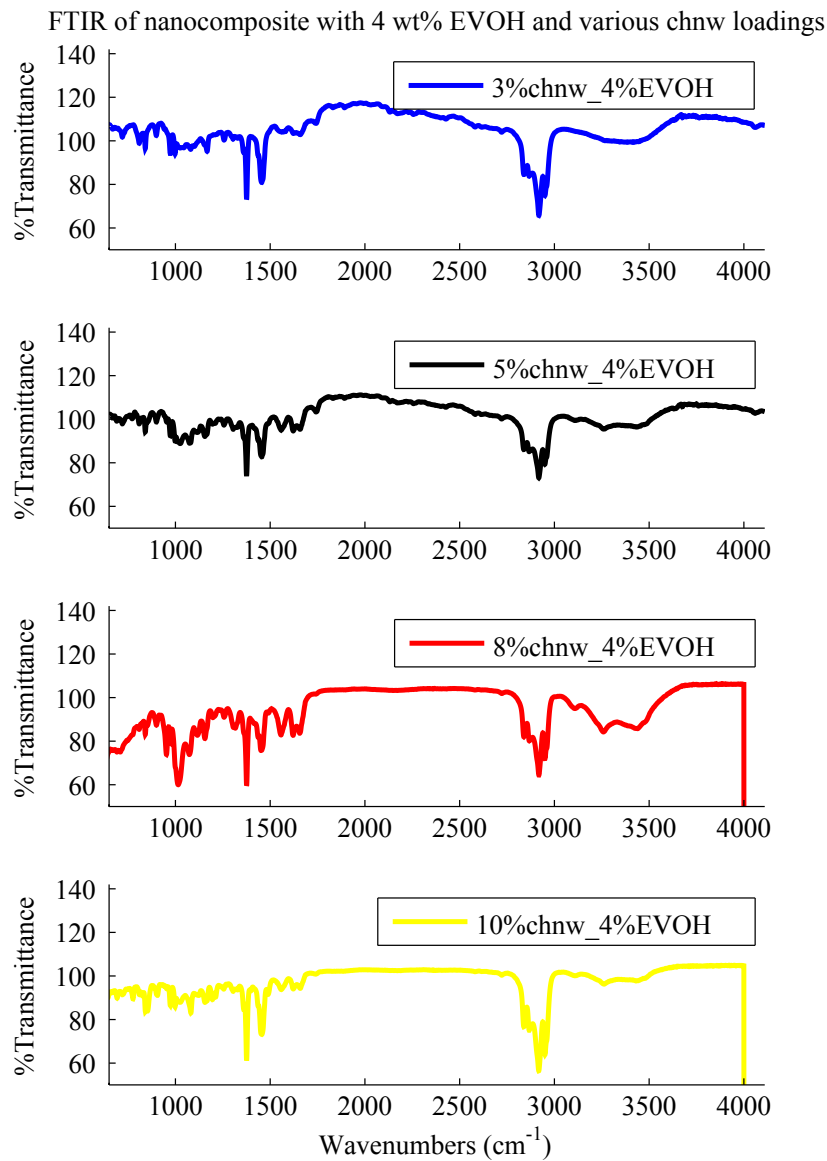


Figure 6.4: FTIR spectra of nanocomposites consisting of the HiPP matrix, 4 wt% EVOH and varying chnw loadings.

Figure 6.5 presents further irregularities and it can be assumed that this is caused by further aggregation of EVOH and chnw within the nanocomposite. The EVOH is clearly not uniformly distributed within the nanocomposite and causes the chnw to agglomerate as well thus lowering the overall interaction and distribution of the chnw with the HiPP matrix.

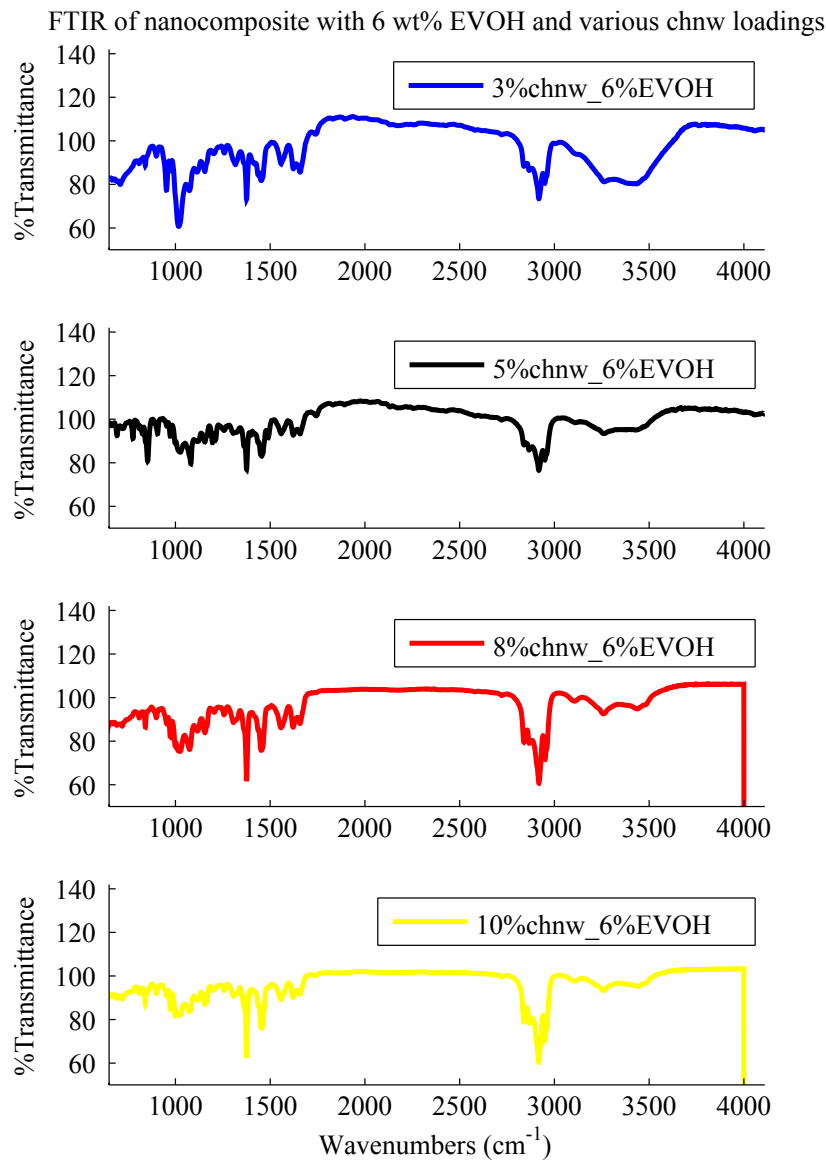


Figure 6.5: FTIR spectra of nanocomposites consisting of the HiPP matrix, 6 wt% EVOH and varying chnw loadings.

Figure 6.6 only further proves the immiscibility of EVOH that occurs in the nanocomposite solution due to the two different solvents that were used. The chnw and EVOH peaks appear slightly larger in intensity compared to the rest of the nanocomposite sample containing 8 wt% EVOH with varying chnw. This could be caused by the small amount of chnw that does not aggregate so much as compared to higher chnw content.

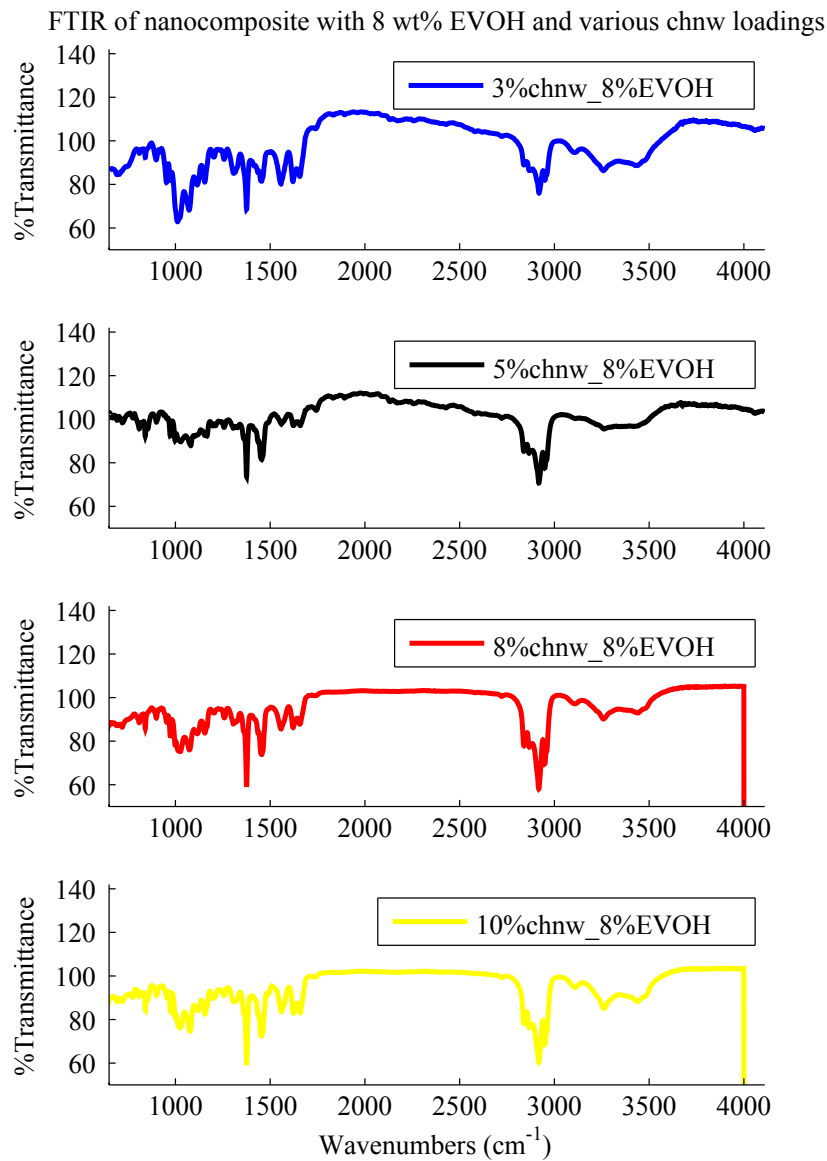


Figure 6.6: FTIR spectra of nanocomposites consisting of the HiPP matrix, 8 wt% EVOH and varying chnw loadings.

The peaks for EVOH seem to almost disappear completely for nanocomposites containing very high EVOH content of 10 wt% as seen in Figure 6.7. The agglomeration of EVOH is too much and very poor interaction between the chnw and HiPP matrix exists.

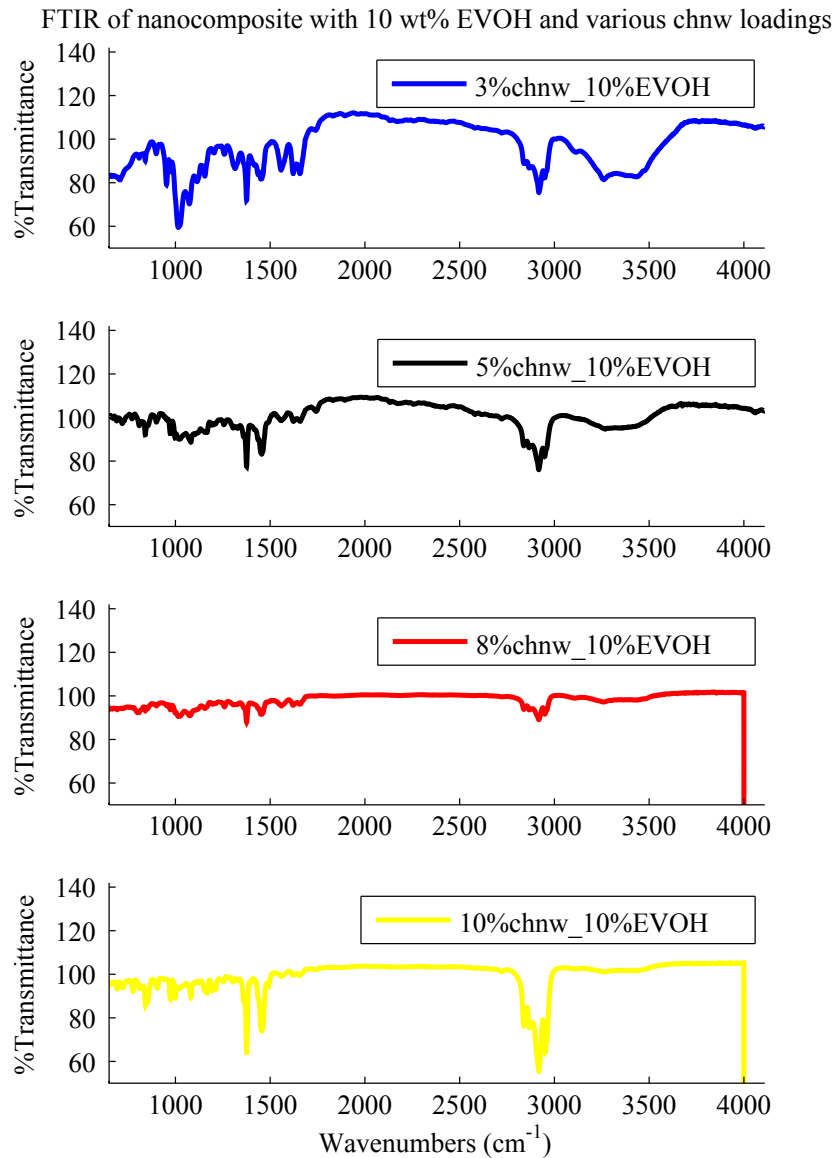


Figure 6.7: FTIR spectra of nanocomposites consisting of the HiPP matrix, 10 wt% EVOH and varying chnw loadings.

6.1.2 TGA

The TGA spectrum of the individual compound present in the nanocomposites are presented in Figure 6.8. The weight loss for EVOH appears to be small and gradual initially. This small loss of weight can be ascribed to moisture loss during heating [10]. The first significant weight loss peak for EVOH can be seen in a temperature range of 295 - 416°C. This is attributed to the major component within the copolymer that is PVOH (poly vinyl-alcohol) [11]. The second peak that follows directly after this weight loss is caused by the ethylene component at approximately 410 °C. Polyethylene acts as a thermal stabilizer in EVOH as found in studies done by Alvarez *et al* [11]. After the weight loss of the ethylene part, the weight loss increases rapidly to 100% at 500 °C[10].

As already mentioned in Chapter 4, weight loss of chnw appears to be immediate and is also caused by loss in moisture. The drop in the slope of the TGA curve belonging to loss of moisture continues up to approximately 60 °C and then stabilizes. Further weight loss commences at 280 °C and begin to even out at approximately 470 °C [3]. High impact polypropylene has weight loss occurring at about 288 °C which rapidly increases at 400 °C until it reaches complete degradation at 500 °C.

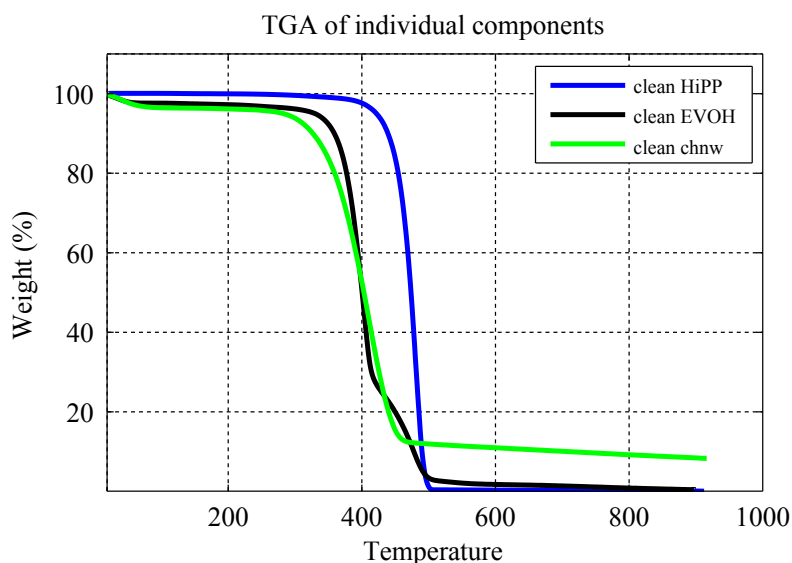


Figure 6.8: TGA curves of individual components used in the preparation of the nanocomposites.

The thermogravimetric analysis results for the nanocomposites containing chnw with EVOH in a HiPP matrix were shown in Figure 6.9 to 6.13. Figure 6.9 presents the TGA results for 2 wt% EVOH with various chnw loadings. The onset temperature does not seem to change significantly for the nanocomposites samples containing 2 wt% EVOH and low chnw loadings compared to the TGA curves of a clean HiPP sample. Only a slightly

more gradual weight loss can be seen for the nanocomposite sample containing 2 wt% EVOH and 3 wt% chnw. The curves for the nanocomposite sample containing higher chnw loadings with 2 wt% EVOH appear to have a slightly earlier onset in degradation than that for a clean HiPP sample. This is the opposite seen for nanocomposites that have PPgMA as a compatibilizer as seen in Section 5.4.

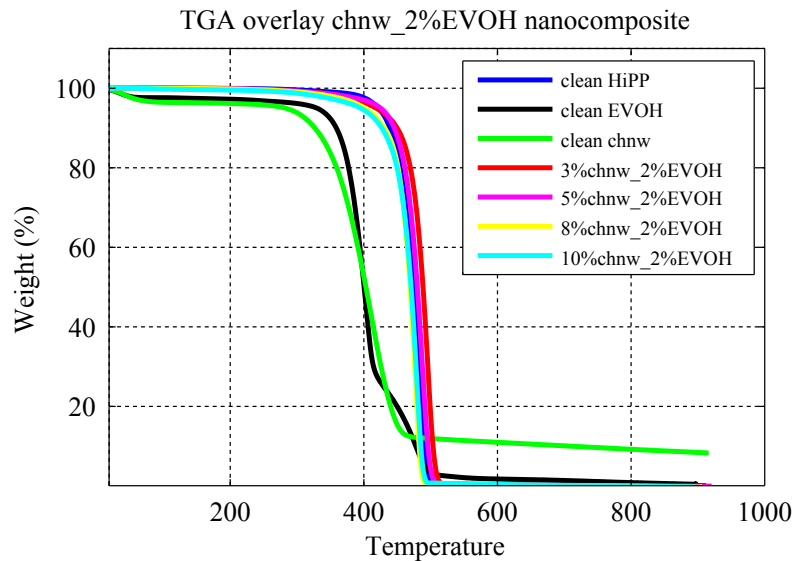


Figure 6.9: TGA curves overlaid to show the change in onset and maximum temperature during incorporation of various chnw loadings with 2 wt% EVOH into HiPP matrix compared with neat samples of HiPP, chnw and EVOH.

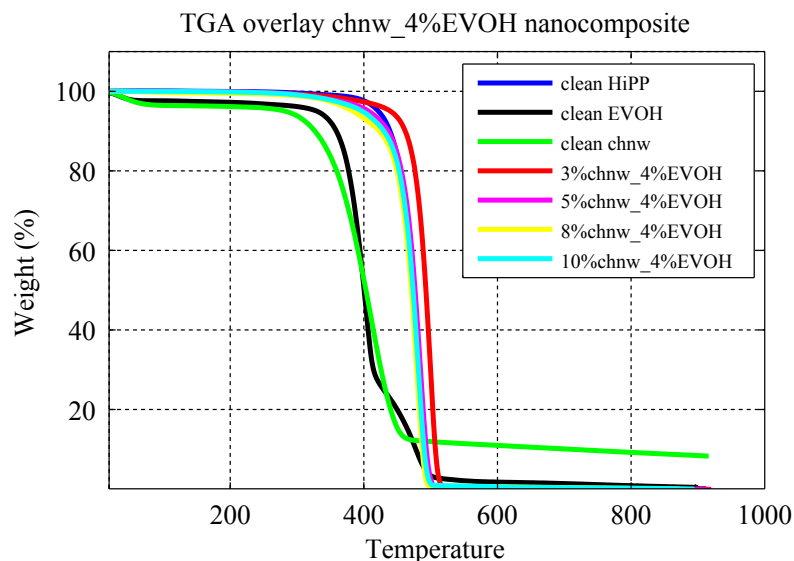


Figure 6.10: TGA curves overlaid to show the change in onset and maximum temperature during incorporation of various chnw loadings with 4 wt% EVOH into HiPP matrix compared with neat samples of HiPP, chnw and EVOH

Figure 6.10 shows a nanocomposite sample containing 3 wt% chnw with 4 wt% EVOH that presents a slightly more gradual onset of degradation temperature than a clean HiPP sample. The nanocomposite sample containing chnw loading of 8 and 10 wt% shows a slight lowering in the onset of the degradation temperature as compared to the clean HiPP sample.

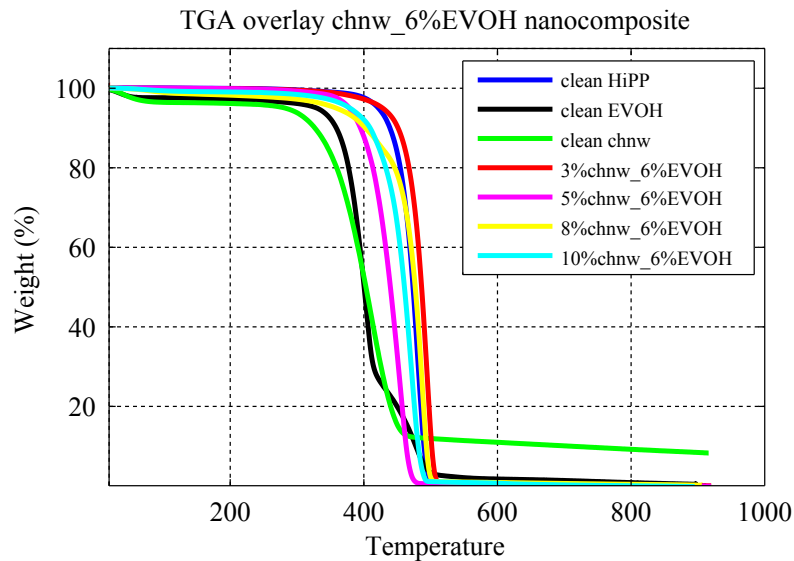


Figure 6.11: TGA curves overlayed to show the change in onset and maximum temperature during incorporation of various chnw loadings with 6 wt% EVOH into HiPP matrix compared with neat samples of HiPP, chnw and EVOH

The nanocomposites containing 6 wt% EVOH are illustrated in Figure 6.11. An improvement in thermal stability of the nanocomposite containing 3 wt% chnw and 6 wt% EVOH was seen. Complete weight loss for only this specific nanocomposite sample was seen at a higher temperature as that for a clean HiPP matrix. The opposite can be seen for nanocomposite samples containing any loading of chnw higher than 3 wt%. The major decline in thermal stability seen for the nanocomposite sample of 5 wt% chnw and 6 wt% EVOH indicates the poor distribution of chnw within the HiPP matrix and how the agglomeration of the EVOH combined with the chnw aggregation effects the thermal properties of the nanocomposite negatively.

Figure 6.12 presents the nanocomposites containing 8 wt% EVOH and varying chnw loading. Once again a decline in the thermal stability can be seen for the nanocomposite samples containing high chnw loadings combined with the high EVOH content. In fact, the increasing EVOH content indicates a overall decline in thermal stability of the nanocomposites even with little chnw present within the HiPP matrix. Aggregation of chnw within the nanocomposite along with the poor distribution of the EVOH within the HiPP matrix causes the thermal stability deterioration. Agglomeration of the chnw can cause the interaction between the EVOH and the HiPP matrix to be hindered and because of the solvent immiscibility that occurs during mixing the interaction between EVOH and the HiPP matrix is hindered even more.

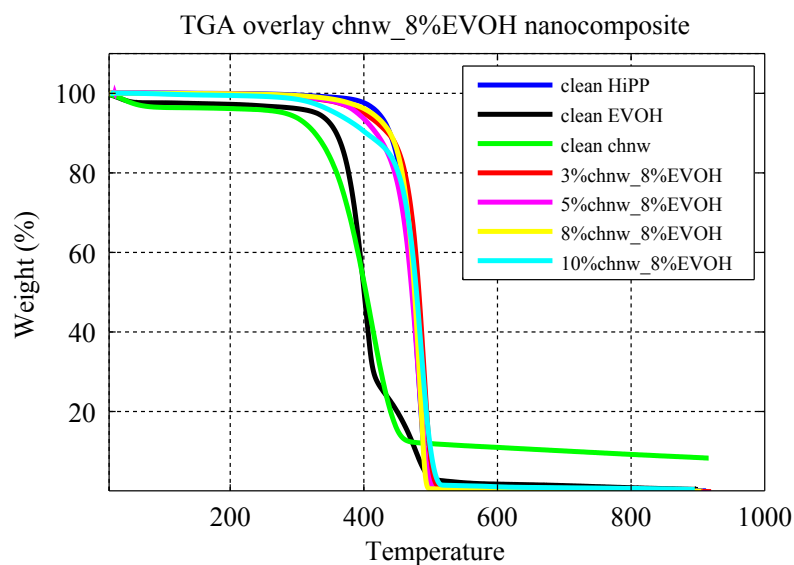


Figure 6.12: TGA curves overlaid to show the change in onset and maximum temperature during incorporation of various chnw loadings with 8 wt% EVOH into HiPP matrix compared with neat samples of HiPP, chnw and EVOH

Figure 6.13 presents the nanocomposites containing 10 wt% EVOH and varying chnw loading. Similar weakening of the thermal stability can be seen as in Figure 6.12. The nanocomposite sample containing 3 wt% chnw loadings combined with 10 wt% EVOH shows a major decline in the onset of degradation temperature which is the complete opposite seen for the nanocomposites containing PPgMA as compatibilizer in Section 5.4.

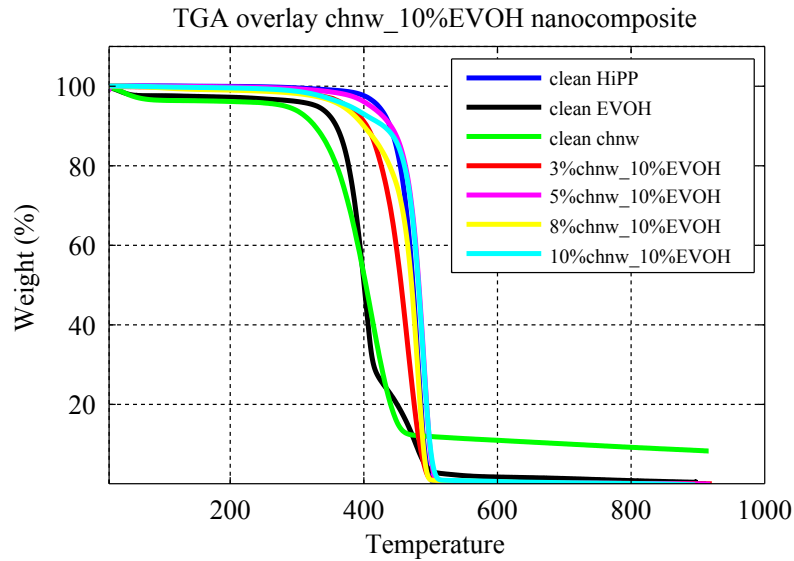


Figure 6.13: TGA curves overlayed to show the change in onset and maximum temperature during incorporation of various chnw loadings with 10 wt% EVOH into HiPP matrix compared with neat samples of HiPP, chnw and EVOH

6.1.3 DSC

The thermal data does not change drastically compared to that of the clean HiPP sample other than the melting temperature that is lowered slightly and there is a variation of the crystallization percentage as seen in Tables 6.1 and 6.2. As mentioned earlier due to poor dispersion of chnw and EVOH within the HiPP matrix the changes in the percentage crystallinity are unpredictable. This is because of the interference that agglomerated EVOH and chnw have on the ability of the polymer chains to crystallize. The nanocomposites was calculated using the same method mentioned in Section 5.3, where the $\Delta H_{100\%}$ of polypropylene was used, 207 J/g.

Table 6.1: Melting points ($^{\circ}\text{C}$) of HiPP/chnw (EVOH) nanocomposites where 0 wt% chnw and 0 wt% EVOH indicates clean HiPP

wt% chnw	T_m ($^{\circ}\text{C}$)					
	0% EVOH	2% EVOH	4% EVOH	6% EVOH	8% EVOH	10% EVOH
0	165.8					
3	163.7	164.6	164.1	164.2	163.1	164.3
5	163.6	164.0	163.4	164.0	164.0	159.2
8	164.0	164.9	164.5	164.4	163.8	164.5
10	164.0	163.6	164.7	164.8	164.7	164.3

Table 6.2: Percentage crystallization (%) of HiPP/chnw (EVOH) nanocomposites where 0 wt% chnw and 0 wt% EVOH indicates clean HiPP

wt% chnw	% Crystallization					
	0% EVOH	2% EVOH	4% EVOH	6% EVOH	8% EVOH	10% EVOH
0	42.48					
3	40.04	39.13	43.96	35.27	37.51	30.75
5	37.03	40.28	38.87	54.01	38.82	46.04
8	37.14	42.40	43.34	28.59	44.35	37.28
10	37.06	38.67	41.38	43.60	40.22	37.89

Figure 6.14 shows that the nanocomposites with low chnw loadings and high EVOH content, as seen for the nanocomposite sample containing 3 wt% chnw with 2 and 4 wt% EVOH, have a slightly higher crystallization peaks compared to the nanocomposites samples with low chnw loadings and higher EVOH loadings.

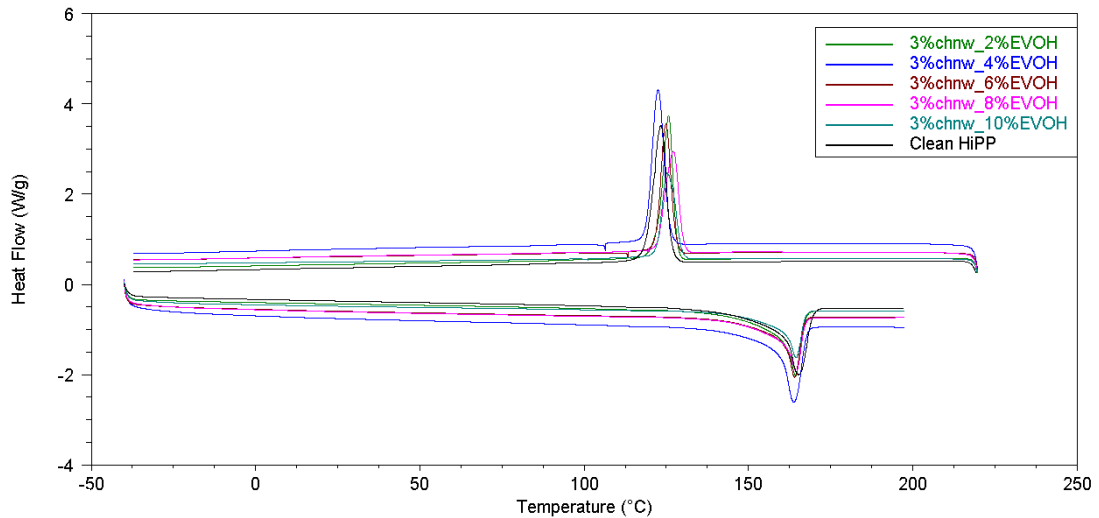


Figure 6.14: DSC curves showing the effect that various wt% EVOH and 3 wt% chnw have on the HiPP matrix.

A increase in the crystallization peak can be seen for nanocomposite sample containing 6 wt% EVOH and a chnw loading of 5 wt% as presented in Figure 6.15. The rest of the nanocomposites containing EVOH have a crystallization peak similar to a clean HiPP sample.

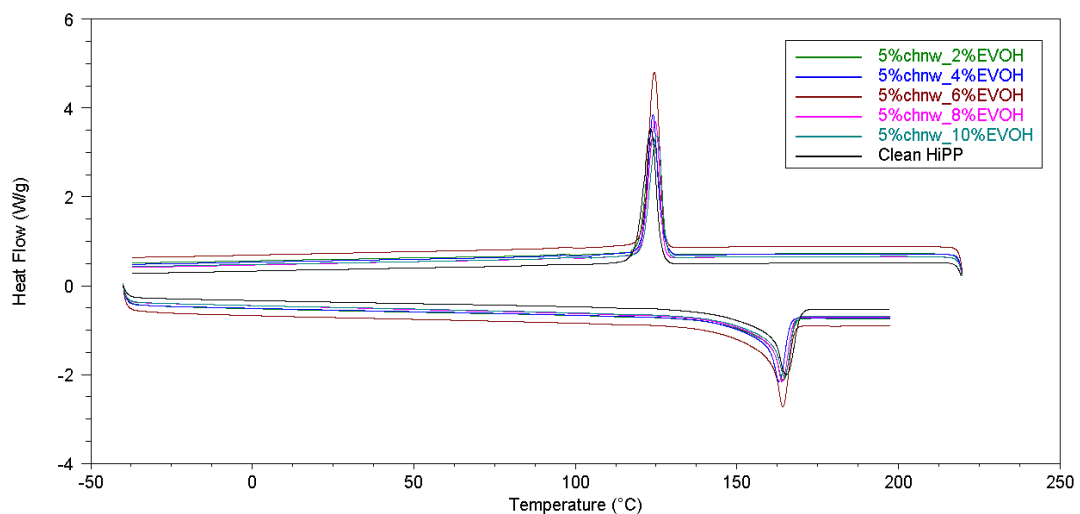


Figure 6.15: DSC curves showing the effect that various wt% EVOH and 5 wt% chnw have on the HiPP matrix.

Similar results can be seen for the DSC curves in 6.16. Nanocomposites containing large amounts of chnw combined with low loadings of EVOH, such as seen for the nanocomposite sample containing 8 wt% chnw and 4 wt% EVOH, show a decrease in the crystallization peak compared to a clean HiPP sample. The nanocomposite sample containing 8 wt% chnw and 8 wt% EVOH shows a higher increase in percentage crystallization compared to a clean HiPP sample. It was possible that the samples used for the DSC analysis of the nanocomposite containing 8 wt% EVOH and 8 wt% chnw consist of irregular distributed regions containing chnw that caused the increase in the crystallization peak.

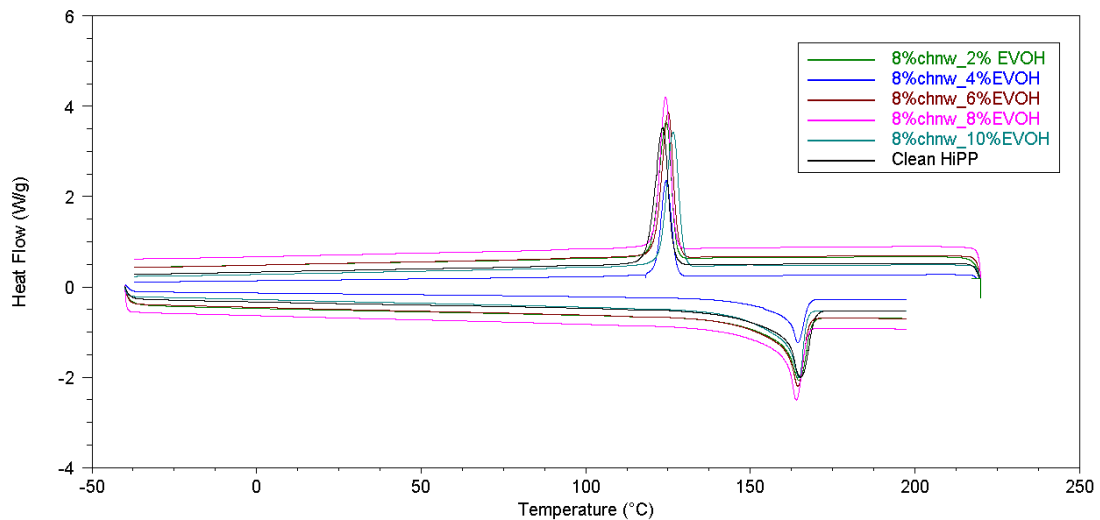


Figure 6.16: DSC curves showing the effect that various wt% EVOH and 8 wt% chnw have on the HiPP matrix.

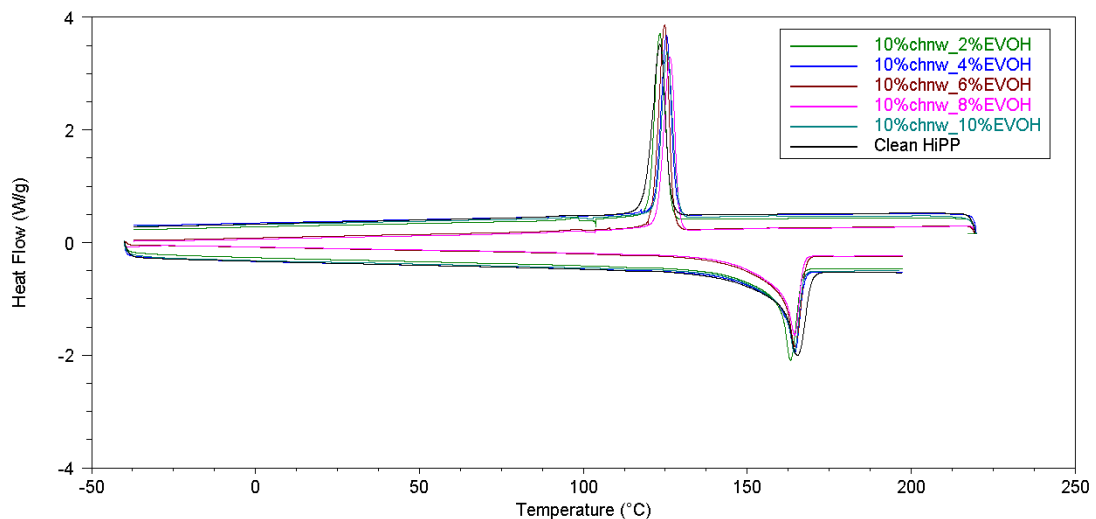


Figure 6.17: DSC curves showing the effect that various wt% EVOH and 10 wt% chnw have on the HiPP matrix.

Figure 6.17 presented crystallization peaks for nanocomposites that are similar to that of a clean HiPP. The poor distribution of EVOH and chnw can be seen in these DSC curves. The irregular dispersion of EVOH and the poor interaction of chnw with the HiPP matrix cause irregular increase and decreases in crystallinity within the nanocomposites. The overall lack in change in the crystallinity and melting temperature proves the poor interaction of chnw and a clean HiPP matrix with EVOH as compatibilizer [10].

6.1.4 Tensile Testing

Figure 6.18 presents the nanocomposite containing no compatibilizer. The chnw seem to have a small effect on the Young's modulus, increasing it slightly. The presence of chnw causes the HiPP matrix to become less ductile thus lowering the elongation at break as mentioned in Section 5.5. The interaction between the chnw and HiPP matrix is very poor with no compatibilizer present.

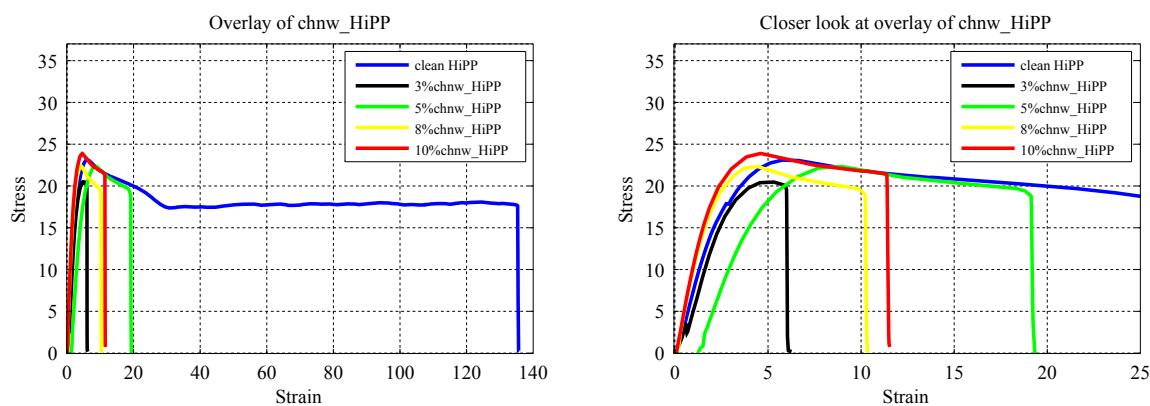


Figure 6.18: Stress-strain curves showing composites containing no compatibilizer and only HiPP and chnw

The results presented in Figure 6.19 show an decrease in the Young's modulus as soon as EVOH is added. The Young's modulus clearly becomes worse as the EVOH loadings are increased within the nanocomposite while the chnw content remains at 3 wt%. The lowest value for the Young's modulus can be seen for the nanocomposite that contains 10 wt% EVOH and 3 wt% chnw within the HiPP matrix which is the opposite seen for the nanocomposites that contain PPgMA as compatibilizer. The maximum tensile strength is much higher compared to the nanocomposite sample containing PPgMA and a clean sample of HiPP. The poor Young's modulus indicated the very unsatisfactory dispersion of chnw and EVOH within the nanocomposite. The elongation at break is slightly higher for the nanocomposite containing 3 wt% chnw and various EVOH loadings. This is also an indication that the tensile strength is mostly withstood by the HiPP matrix. This

shows poor stress transfer between the chnw and the HiPP matrix.

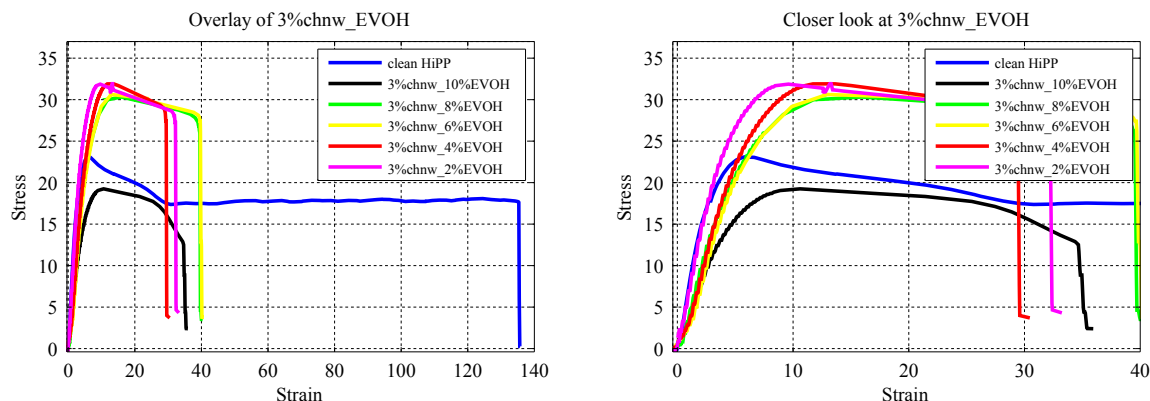


Figure 6.19: Stress-strain curves of 3 wt% chnw with varying EVOH content

Figure 6.20 shows the nanocomposites with 5 wt% chnw content and varying EVOH content. The maximum tensile strength is high for a nanocomposite samples with EVOH although it is difficult to see a trend because of the irregular distribution of EVOH within the HiPP matrix. This uneven dispersion of EVOH in the nanocomposite causes poor interaction of chnw with the HiPP matrix which in turn interferes with the tensile properties of the nanocomposite.

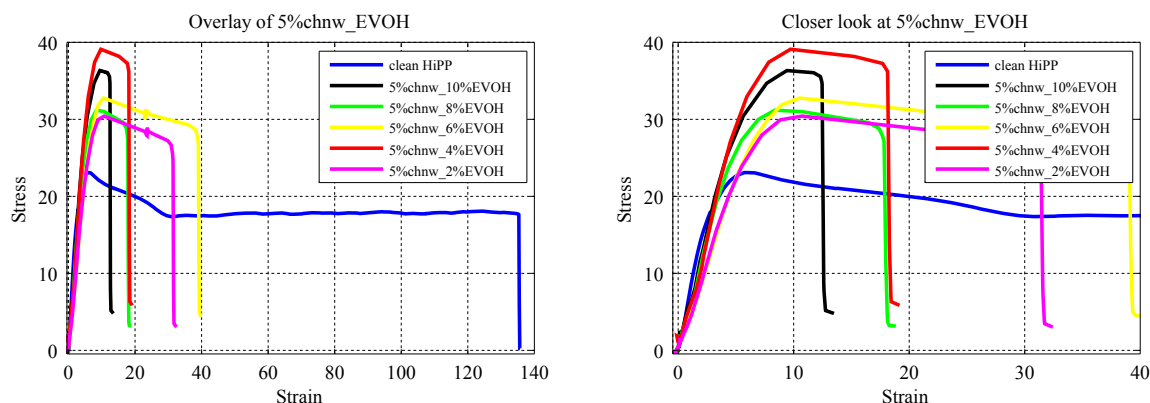


Figure 6.20: Stress-strain curves of 5 wt% chnw with varying EVOH content

The composite sample containing 8 wt% chnw and various loading of EVOH can be seen in Figure 6.21. The maximum tensile strength for this composite containing a chnw loading of 8 wt% is also higher than a clean sample of HiPP and for the nanocomposites containing PPgMA as compatibilizer. The Young's modulus for all the composite samples is much lower than a clean HiPP sample. No improvement in the Young's modulus can be seen especially if the EVOH content is increased.

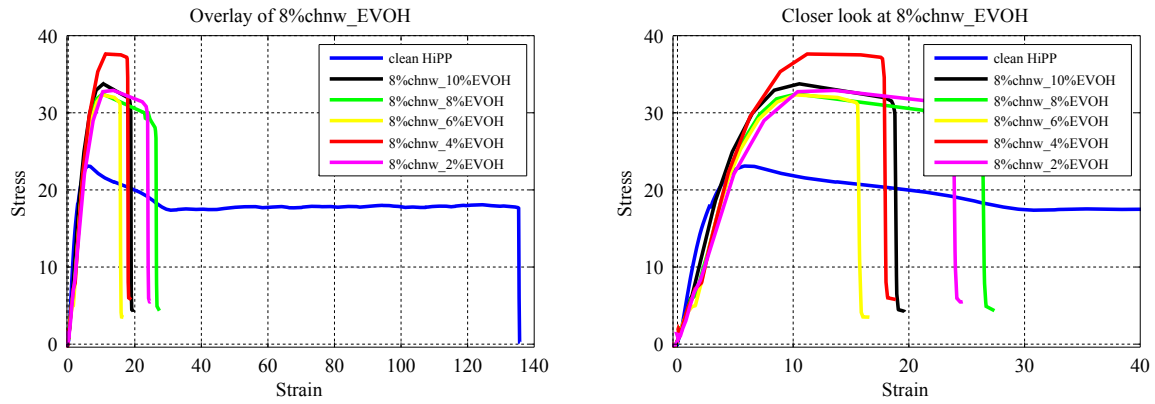


Figure 6.21: Stress-strain curves of 8 wt% chnw with varying EVOH content

Figures 6.22 to 6.23 indicates the effect on the tensile properties of the nanocomposite when EVOH was used as a compatibilizer between chnw and HiPP matrix. Figure 6.22 illustrate the slight increase in Young's modulus as the chnw content is increase. The Young's modulus is closer to the Young's modulus found for a clean HiPP sample although not higher. This increase can specifically be seen for nanocomposite containing 10 wt% chnw and low EVOH content of 2 wt%. Although the high chnw content of 10 wt% tend to agglomerate more (because the increase interaction between the chnw chains), the high amount of chnw in the nanocomposite, even without proper EVOH compatibilization, affords some support to the HiPP matrix.

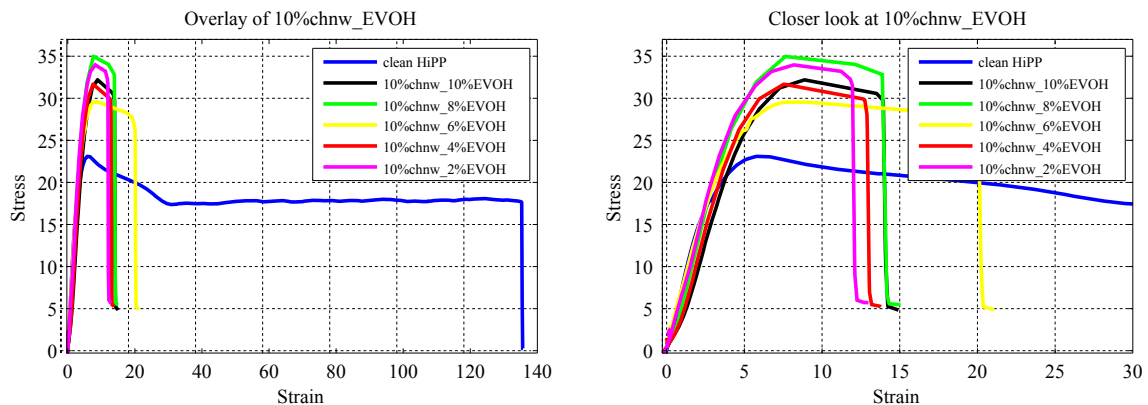


Figure 6.22: Stress-strain curves of 10 wt% chnw with varying EVOH content

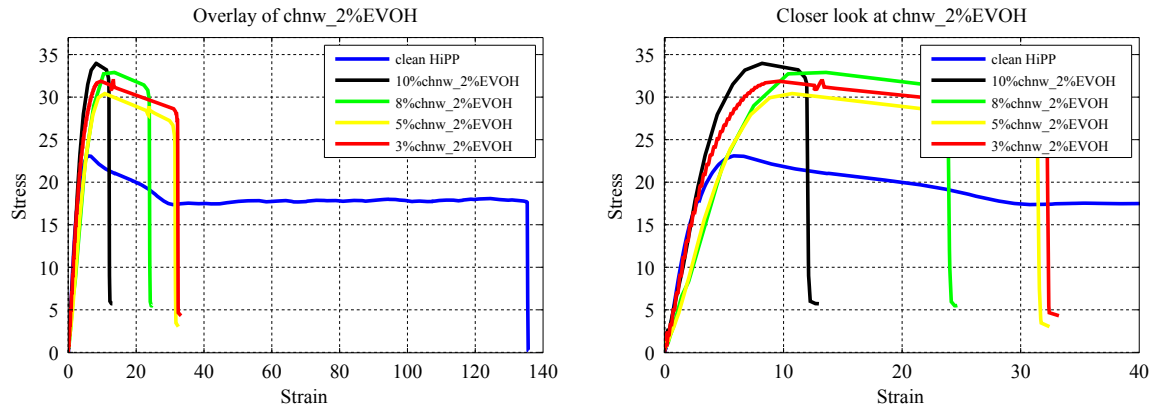


Figure 6.23: Stress-strain curves of 2 wt% EVOH with varying chnw content

All the nanocomposite samples in Figure 6.23 showed a lower Young's modulus than that for a clean HiPP sample. The elongation at break increases for the nanocomposites containing lower chnw loadings combined with 2 wt% EVOH. This is higher than that seen for nanocomposites with PPgMA as compatibilizer.

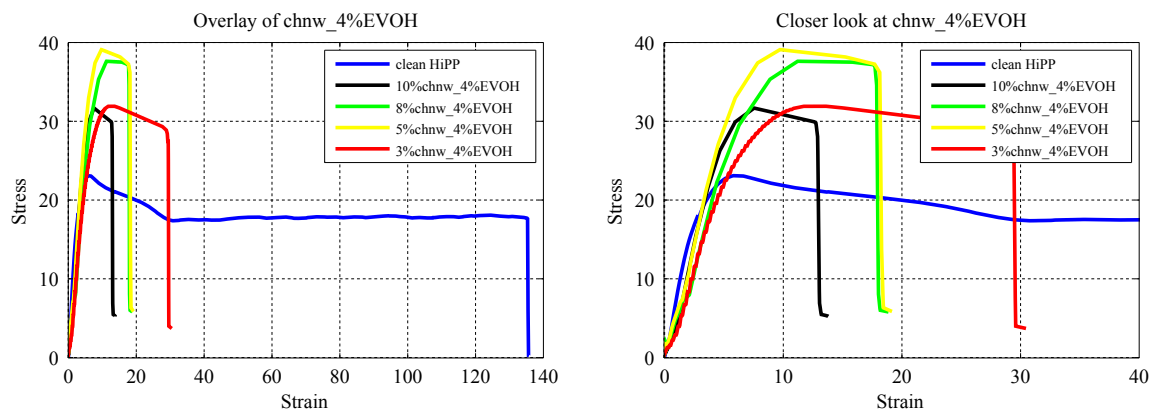


Figure 6.24: Stress-strain curves of 4 wt% EVOH with varying chnw content

Figure 6.24 shows an overall decrease of the Young's modulus for all the nanocomposites. The nanocomposite samples containing 5 wt% and 8 wt% chnw with 4 wt% EVOH show the very high maximum tensile strength. The elongation at break for the nanocomposite with 3 wt% chnw and 4 wt% EVOH shows a higher elongation at break.

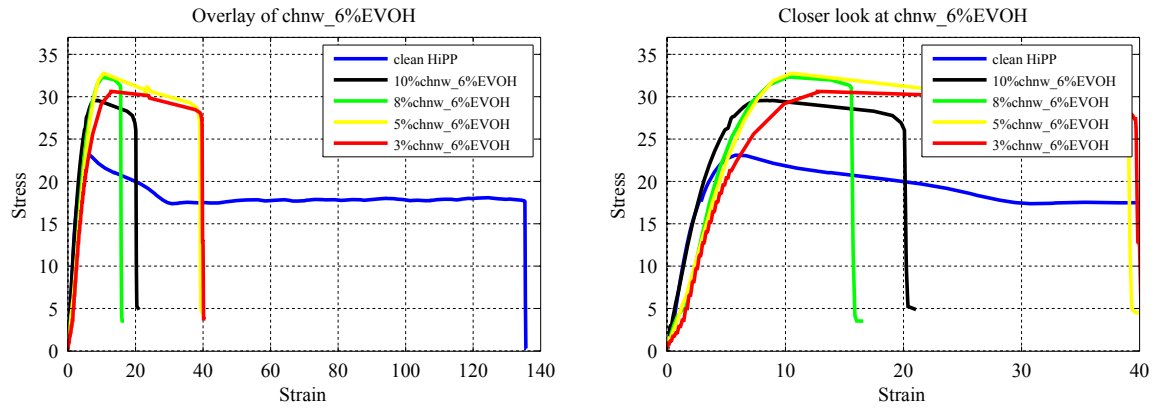


Figure 6.25: Stress-strain curves of 6 wt% EVOH with varying chnw content

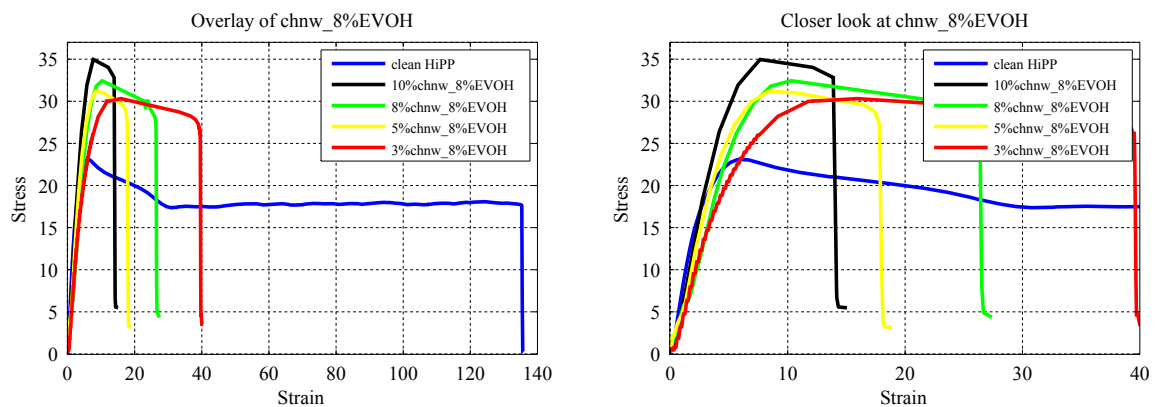


Figure 6.26: Stress-strain curves of 8 wt% EVOH with varying chnw content

Figures 6.25, 6.26 and 6.27 show a poor Young's modulus for all the nanocomposites containing 6 wt%, 8 wt% and 10 wt% EVOH loadings. The elongation at break for the nanocomposites with very low chnw loadings and higher EVOH content are higher than the elongation at break found for nanocomposites with PPgMA as compatibilizer. The maximum tensile strength is higher than that for a clean HiPP sample although not as high as the maximum tensile strength seen for the nanocomposite samples containing 4 wt% EVOH and 4 and 8 wt% chnw.

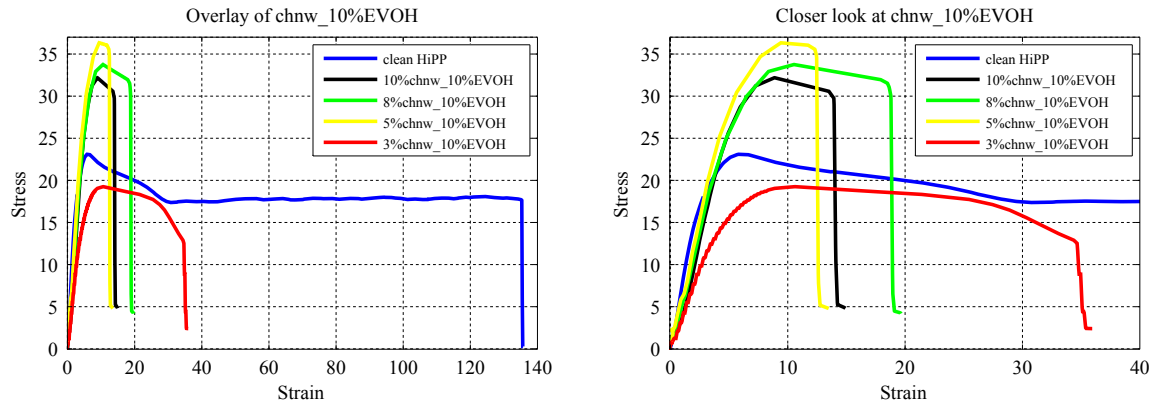


Figure 6.27: Stress-strain curves of 10 wt% EVOH with varying chnw content

The Young's modulus values that are presented in Tables 6.4 and 6.5 are very close to the values seen in Table 6.3 that present the Young's modulus values for nanocomposites containing no compatibilizer but only HiPP and chnw. The drastic drop in the Young's modulus seen for the sample that contains 3% chnw and 10% EVOH is indicative of how the dispersion is affected due to the agglomeration that occurs during the solvent casting process. An increase in the chnw content allows for more regions within the nanocomposite to contain chnw but the compatibility between the matrix and the filler remains poor since EVOH does not function effectively within the nanocomposite.

Table 6.3: Tensile testing data of clean sample HiPP as well as HiPP containing chnw with no compatibilizer

Sample Name	Young's Modulus (MPa)
Clean_HiPP	4.7
3%chnw_HiPP	4.6
5%chnw_HiPP	4.4
8%chnw_HiPP	4.7
10%chnw_HiPP	4.5

Only the combinations for the nanocomposites with EVOH as compatibilizer that compare directly with the results for the nanocomposites containing PPgMA as compatibilizer were shown. The combination that were presented in Section 5.5 showed ideal improvement in tensile properties for the nanocomposites containing PPgMA as compatibilizer. The opposite can be seen for the nanocomposites with EVOH as compatibilizer in Tables 6.4 and 6.5.

Table 6.4: Tensile testing data of 2 wt% EVOH with various wt% chnw in HiPP matrix

Sample	Young's Modulus (MPa)
3%chnw_2%EVOH	5.8
5%chnw_2%EVOH	5.8
8%chnw_2%EVOH	4.2
10%chnw_2%EVOH	5.7

There appears to be no optimum conditions for overall mechanical improvement with the nanocomposites containing EVOH as compatibilizer. The maximum tensile strength is increased due to some EVOH/chnw interaction within the nanocomposite. The fact that the ductility of the HiPP matrix is only slightly affected proves that the interaction between the HiPP matrix and chnw are unsatisfactory.

Table 6.5: Tensile testing data of 10 wt% EVOH with various wt% chnw in HiPP matrix

Sample	Young's Modulus (MPa)
3%chnw_10%EVOH	2.9
5%chnw_10%EVOH	5.6
8%chnw_10%EVOH	6.1
10%chnw_10%EVOH	6.2

The maximum extension for a clean sample of HiPP before compensation is 63.33 mm, whereas for 3%chnw_2%EVOH as seen in Figure 6.19, the extension before compensation is 4.86 mm. Overall the amount of load that can be supported by the nanocomposites are lower than that for clean HiPP. Clean HiPP supports a load up to approximately 185 N but 3%chnw_10% EVOH can only support a load up to 439 N. A slight increase in the load support can be seen for the nanocomposite with high chnw loading in the presence of low EVOH content, but the load support is still lower than that for a clean HiPP sample.

6.2 Electrospinning and melt-pressing

6.2.1 SEM

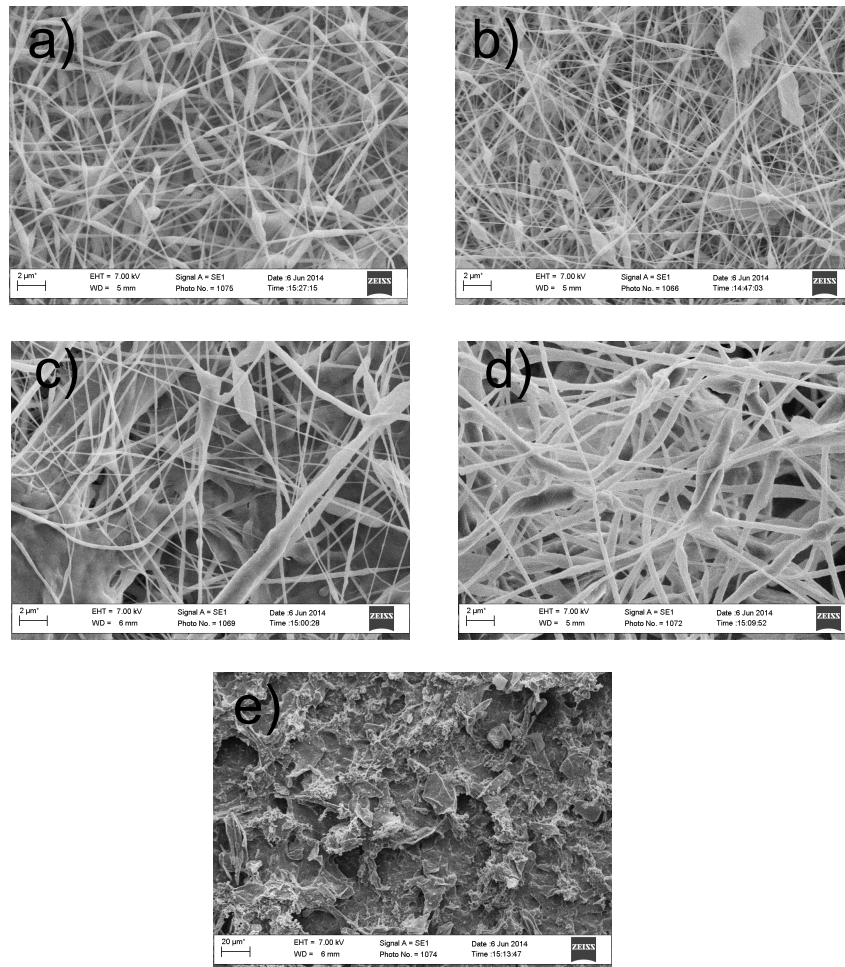


Figure 6.28: SEM images of chnw_EVOH electrospun fiber mats containing (a) clean 5% EVOH, (b) 3% chnw_5% EVOH, (c) 5% chnw_5% EVOH, (d) 8% chnw_5% EVOH and (e) 10% chnw_2% EVOH

The SEM images in Figure 6.28 show electrospun fiber mats. EVOH was electrospun without chnw and 5wt% EVOH was chosen as the optimum concentration for a electrospinning solution, showing good clean fibers. There was some beading that occurred as seen in the Figure 6.28(a). The atmospheric conditions of the laboratory during electrospinning can have a influence in the polymer solution. It has been found that, at high humidity, water condenses on the surface of the fiber which can have a effect on the fiber morphology [12]. The increase in humidity will also affect the rate of evaporation of the solvent during the electrospinning process. At low humidity clogging at the needle tip can occur due to rapid evaporation of the solvent [12].

It can be seen that the fibers became less optimal as the chnw content increased. The flow rate became difficult to control due to the increase in viscosity. The dispersion of chnw within the electrospinning solution became challenging also as an effect of the agglomeration that coincided with the increase in nanowhisker content. Some of the chnw may remain in the syringe after electrospinning due to agglomeration of chnw and this means that a lower concentration of chnw could be incorporated into the electrospun fibers than expected, especially for higher loading of chnw.

It became necessary to lower the concentration of EVOH within the electrospinning solution in order to compensate for the increase viscosity of the solution specifically for a high chnw loading of 10wt%. The high chnw content caused the electrospinning solution to become extremely viscous. The attempt to lower the viscosity of the electrospinning solution with such a high chnw loading proved to be futile as seen in figure 6.28 (e) since no fibers could be produced. The dispersion of chnw is not ideal and the electrospinning solution is still too viscous. This can also be ascribed to the fact that the parameters of electrospinning such as the flow rate, dispersion of chnw, the charge and also the interaction between the EVOH and the chnw became significantly more challenging to control with such a highly viscous solution.

After the incorporation of the fiber mat into HiPP via melt-pressing the nanocomposite was investigated with SEM once more. It was seen in figure 6.29 that there was some melting of the fibers within the HiPP films. Even though the melting point of EVOH (32wt%) is 183°C and the melt-pressing was done approximately 3°C below this melting temperature, it could not prevent some melting of the electrospun fibers to take place. Lowering the temperature during the melt pressing process was unfortunately not an option because of the high melting temperature of HiPP [13].

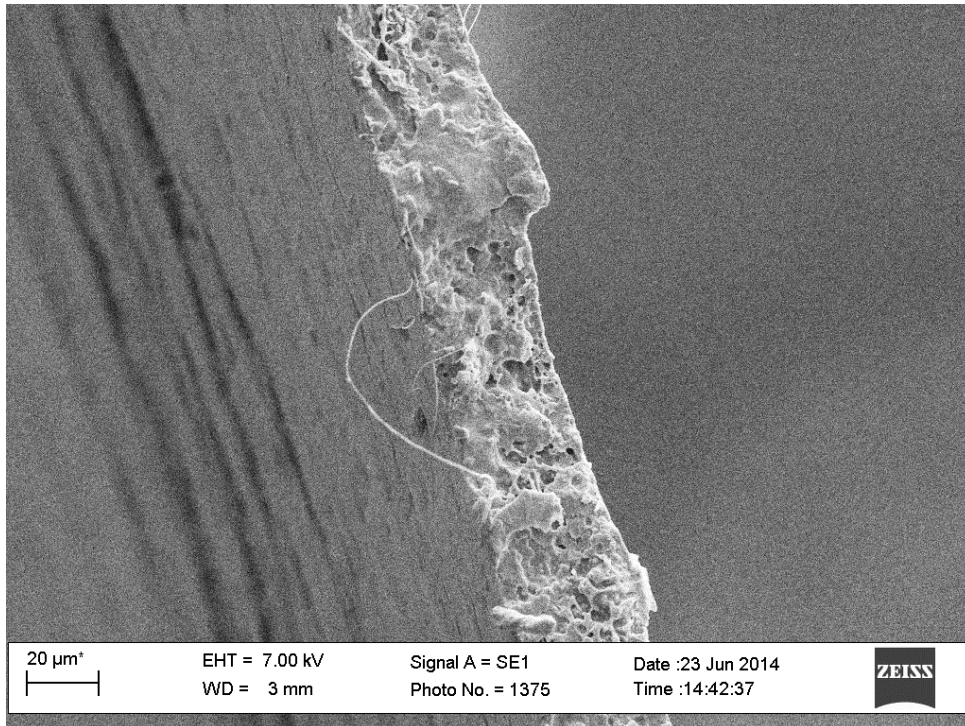


Figure 6.29: SEM images of electrospun fiber mat consisting of 3 wt% chnw and 5 wt% EVOH in HiPP.

6.2.2 ATR-FTIR

The FTIR spectra as seen in Figures 6.30 and 6.31 indicate electrospun fibers consisting of EVOH and chnw before incorporation into HiPP and after incorporation into HiPP respectively. The irregularities that exist in the previous section are no longer present for the nanocomposites containing an electrospun EVOH and chnw fiber mat with good fiber morphology. In the Clear peaks can be identified for the FTIR spectra of electrospun fibers containing chnw and EVOH in Figure 6.30. As discussed in Section 6.1.1, the infrared spectra for EVOH shows the absorption band of the hydroxyl group at 3050 cm^{-1} to 3550 cm^{-1} [7]. Peaks correlating to the PVOH part is seen at 230 cm^{-1} and 280 cm^{-1} [8]. There appears to be a slight increase in the intensity for the peaks corresponding to the amide moiety, at 1580 cm^{-1} , 1625 cm^{-1} and 1662 cm^{-1} , as the chnw content increases.

The peaks of chnw, HiPP and EVOH appear to overlap creating some difficulty in identifying peaks after the incorporation of the electrospun fiber mat into HiPP. Peaks belonging to the PVOH part of EVOH can be seen at 230 cm^{-1} and 280 cm^{-1} corresponding to the C=O groups. Figure 6.31 illustrates the nanocomposites containing electrospun fiber mats consisting of varying chnw loading and EVOH in a HiPP matrix. The optimal EVOH concentration for electrospinning was chosen as 5 wt% based on the good fiber morphology that were produced by a clean solution of EVOH at this concentration. The concentration needed to be changed to 2 wt% EVOH in the electrospinning solution for 10 wt% chnw in an attempt to lower the electrospinning solution to a more optimal viscosity.

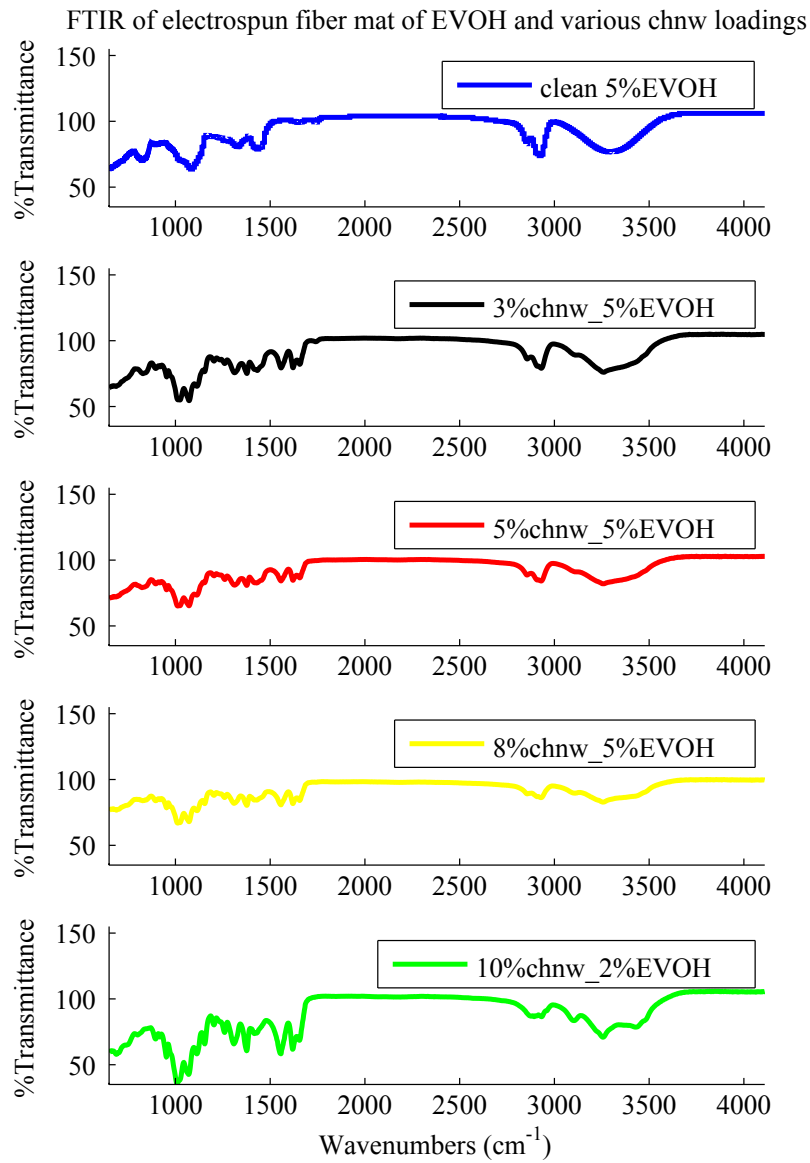


Figure 6.30: FTIR of EVOH/chnw electrospun fiber mats.

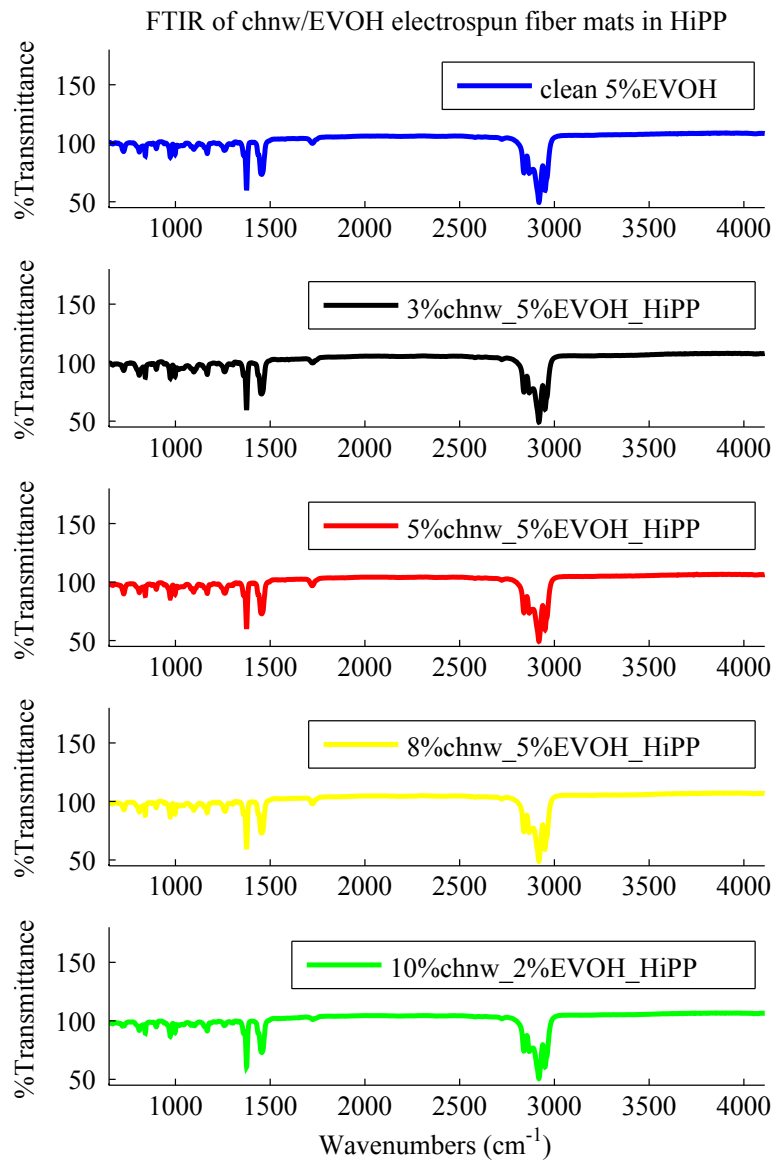


Figure 6.31: FTIR of EVOH/chnw electrospun fiber mats melt pressed into a HiPP matrix.

6.2.3 TGA

The TGA curves for the electrospun fiber mats show that the chnw and EVOH have similar maximum onset degradation temperatures. The chnw improves the overall thermal properties of EVOH slightly. The thermogravimetric analysis for EVOH and chnw is described completely in Section 6.1.2.

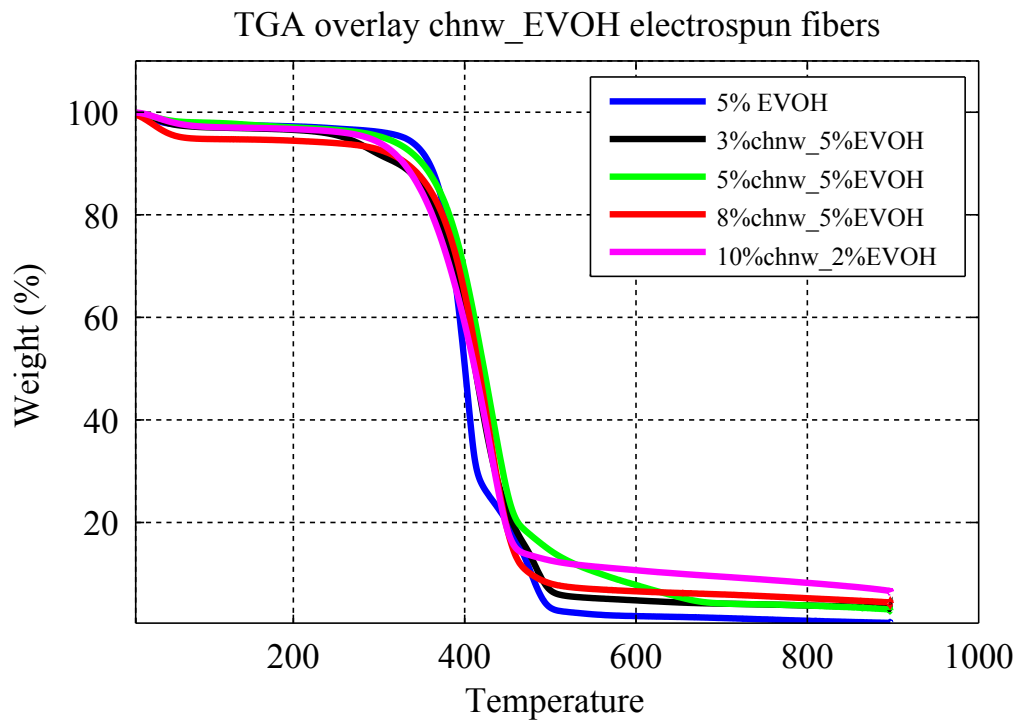


Figure 6.32: TGA overlay of electrospun chnw/EVOH fiber mats.

Once the fiber mats were incorporated into HiPP, a larger shift in the onset degradation temperature could be seen. The nanocomposite sample containing 10 wt% chnw and 2 wt% EVOH electrospun fibers shows a decrease in the onset of degradation temperature compared to a clean HiPP matrix. Agglomeration inside the syringe may cause some of the nanowhiskers to remain in the syringe after electrospinning and therefore lead to the incorporation of less chnw into the electrospun fibers than expected. The thermal stability of the nanocomposites containing electrospun fiber mats is not as good as that seen in Section 5.4 for the nanocomposites containing PPgMA as compatibilizer.

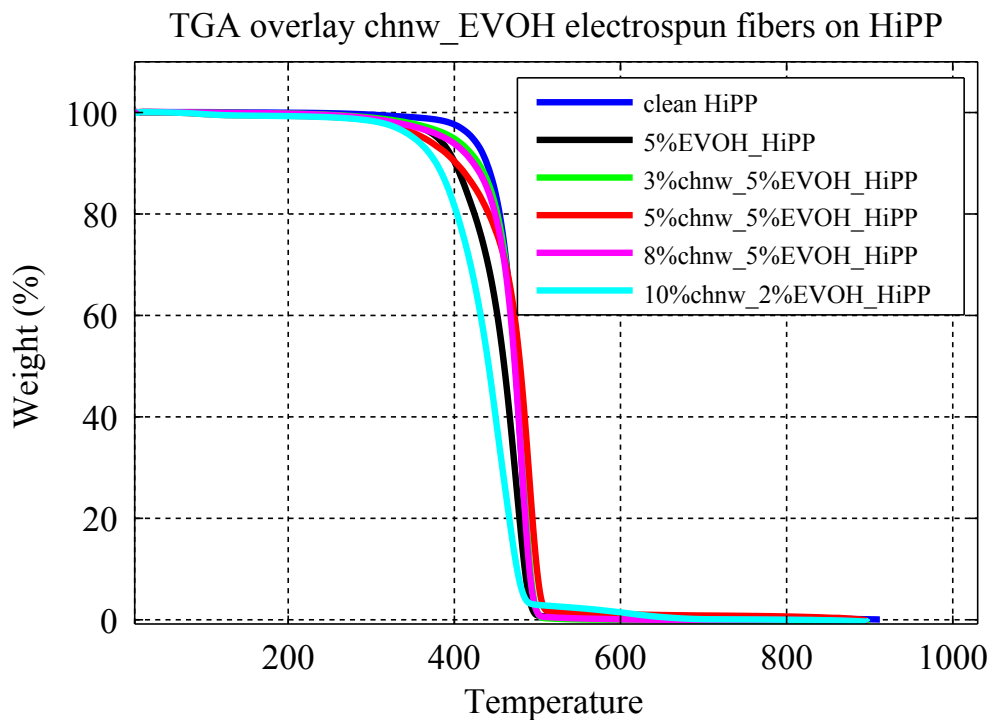


Figure 6.33: TGA overlay of electrospun chnw/EVOH fiber mats that were sandwiched between two HiPP films and meltpressed.

6.2.4 DSC

The $\Delta H_{100\%}$ for PVOH (which is the most abundant component within EVOH) of 138.6 J/g was used to calculate the percentage crystallization for the clean electrospun fibers. The percentage crystallization for the meltpressed nanocomposites was calculated using the Equation 5.1 mentioned in Section 5.3, where the $\Delta H_{100\%}$ of polypropylene was used, 207 J/g.

There is a large decrease in the crystallization percentage for the electrospun fibers compared to the clean EVOH electrospun fibers as seen in Table 6.6. The thermal properties remain mostly unchanged for the fiber mat containing 3 wt% chnw and 5 wt% EVOH compared to a clean EVOH sample. A drastic decrease in crystallization can be seen as the chnw content increases in the electrospun fiber mat. The fiber mat consisting of 10 wt% chnw and 2 wt% EVOH has no fibers and this can be clearly effected the percentage crystallization. The melting temperature for the fiber mats does not change significantly compared to a clean EVOH sample except for the fiber mat containing 10 wt% chnw and 2 wt% EVOH which is once again due to the non-existent fibers.

Table 6.6: DSC data of electrospun fibers consisting of EVOH and chnw

Sample name	Melting Temperature (°C)	Percentage Crystallization (%)
clean EVOH	180.47	48.95
3%chnw_5%EVOH	180.91	43.52
5%chnw_5%EVOH	181.14	29.32
8%chnw_5%EVOH	180.67	12.73
10%chnw_2%EVOH	143.31	1.523

Table 6.7 shows the crystallization percentage and melting temperature for the nanocomposites containing electrospun fiber mats incorporated into a clean HiPP matrix. Agglomeration of chnw can occur inside the syringe. This may cause some of the chnw to stay behind inside the electrospinning needle after electrospinning. This can lead to a lower chnw concentration incorporated into the nanocomposite than was expected [3]. This can especially be expected for high chnw loading where agglomeration is more prominent. The ability for EVOH molecules to crystallize is less hindered and this can lead to a higher percentage crystallization than expected [3]. This can be seen for the nanocomposite containing electrospun fiber mat consisting of 8 wt% chnw and 5 wt% EVOH. The melting temperature and crystallization percentage for the fiber mat nanocomposites are slightly lower than for a clean HiPP sample.

Table 6.7: DSC data of nanocomposite consisting of electrospun EVOH, chnw and HiPP

Sample name	Melting Temperature (°C)	Percentage Crystallization (%)
Clean HiPP	165.83	42.48
5%EVOH	162.09	33.83
3%chnw_5%EVOH	162.45	39.45
5%chnw_5%EVOH	161.80	33.56
8%chnw_5%EVOH	161.92	36.36
10%chnw_2%EVOH	162.39	30.87

Figure 6.34 illustrates the drop in crystallization percentage of the electron fiber mats as the chnw loading increases. The increase of the chnw content becomes aggregated due to strong hydrogen bonding between the amide moieties of the chnw. The crystallization of the EVOH fibers become hindered because of the agglomerated chnw.

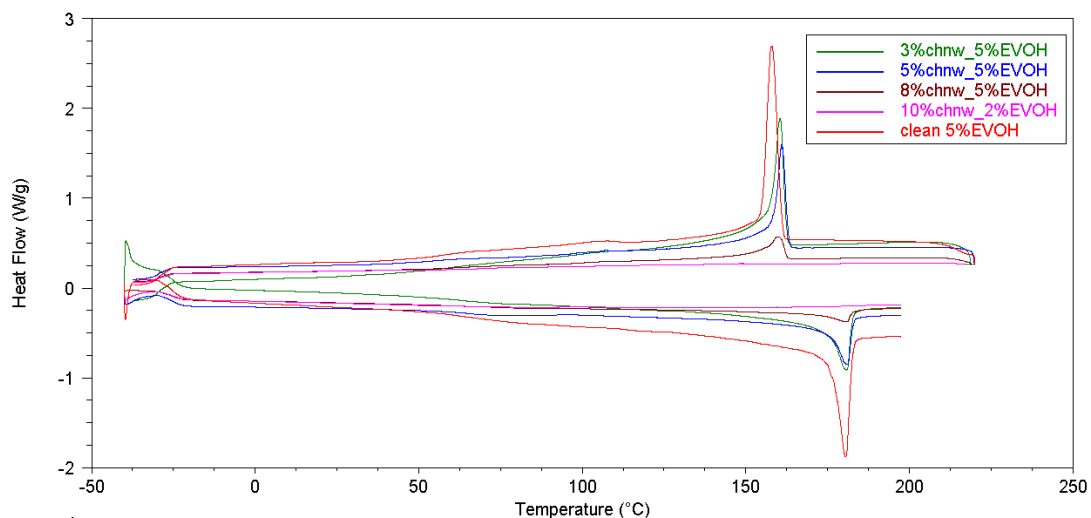


Figure 6.34: DSC thermograms of chnw/EVOH electrospun fibers.

Figure 6.35 presents the DSC thermograms for the nanocomposite containing the electron fiber mats. The crystallization percentage and melting temperature appear relatively similar to a clean HiPP sample. The nanocomposite sample containing 3 wt% chnw and 5 wt% EVOH electrospun fiber mat show better percentage crystallization compared to the rest of the nanocomposites.

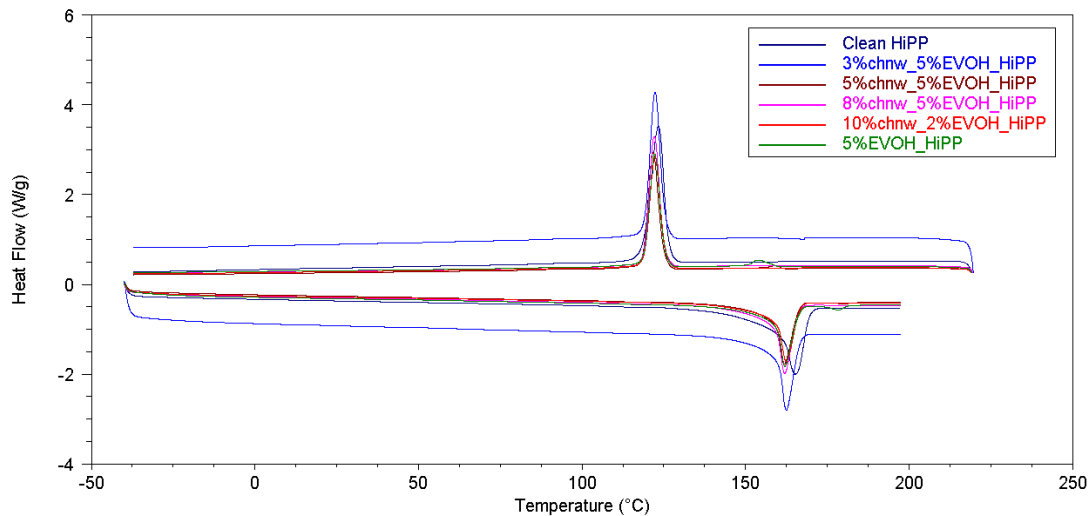


Figure 6.35: DSC thermograms of chnw/EVOH electrospun fibers meltpressed into a HiPP matrix.

6.2.5 Tensile Testing

The Young's modulus showed greater improvement for the nanocomposites containing electrospun fiber mats compared to the nanocomposites that were made using the first technique mentioned in Section 6.1. The Young's modulus results shown in Figure 6.36 appear to be consistent with what can be seen from the fiber morphology in the SEM images. The maximum stress that the nanocomposite can withstand became diminished as the loading of chnw were increased. As expected the only sample that presented good mechanical properties was the nanocomposite containing a loading of 3 wt% chnw.

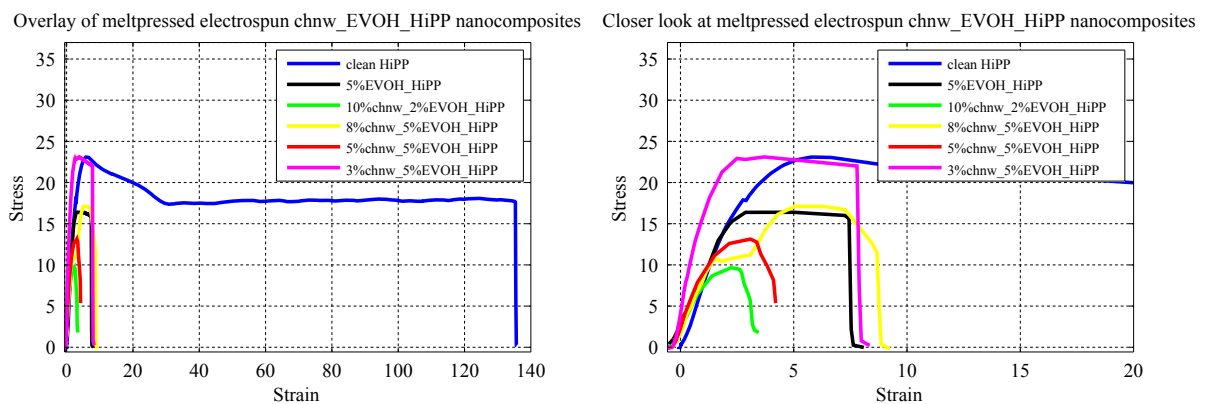


Figure 6.36: Tensile overlay of electrospun chnw_EVOH fiber mats that were sandwiched between two HiPP films and then melt-pressed.

It can be seen in Table 6.8 that the stress transfer is very good for the nanocomposite that contains 3%chnw_5% EVOH. Effective dispersion was accomplished during electrospinning for low chnw loadings. The Young's modulus decreases slightly as the chnw content

increases. This is due to the declining fiber morphology that is caused by the increase in viscosity and pessimal parameter effects.

Table 6.8: Tensile testing data of electrospun chnw_EVOH in HiPP

Sample Name	Young's Modulus (MPa)
Clean_HiPP	4.685
5%EVOH_HiPP	6.207
3%chnw_EVOH_HiPP	10.046
5%chnw_EVOH_HiPP	7.043
8%chnw_EVOH_HiPP	8.043
10%chnw_EVOH_HiPP	6.910

The stress transfer becomes less effective between the fibers and the matrix due to the poor electrospinning conditions. As mentioned in Section 6.2.1 the tensile properties can also be affected by the partial melting of the chnw/EVOH fibers that took place during the meltpressing process. The optimal chnw and EVOH content were chosen as 3%chnw_5%EVOH. It showed the highest increase for the Young's modulus after incorporation into the HiPP matrix and the best fiber morphology after electrospinning.

6.3 Conclusion

6.3.1 Solvent casting and injection molding

The infrared spectra showed the presence of the individual components (EVOH, chnw and HiPP) within the nanocomposites. Some increase in the peak intensity could be seen for higher chnw loadings but the poor distribution and agglomeration that occurred because of the immiscibility of the EVOH in xylene mostly caused poor peak intensities for the IR spectra of chnw and EVOH. The thermal gravimetric analysis showed a decline in the thermal stability (compared to a clean HiPP sample) as the EVOH content increased within the nanocomposite. This can be explained by the fact that the dispersion of the chnw within the matrix is very poor because of the immiscibility of the EVOH in xylene. This immiscibility of EVOH in the xylene caused the EVOH to form a separated interface between the HiPP and the chnw causing irregular distribution of EVOH in the nanocomposite as well as poor interaction between the chnw and the HiPP matrix. The thermal data does not change drastically compared to that of the clean HiPP sample other than the melting temperature that is lowered slightly and there is a variation of the crystallization percentage. Due to the poor dispersion of chnw and EVOH within the HiPP matrix, the changes in the percentage crystallization are unpredictable. The

tensile properties for the nanocomposites with EVOH as compatibilizer show overall deterioration compared to the nanocomposites that contained PPgMA as a compatibilizer. The maximum tensile strength, however for both types of nanocomposites (containing PPgMA or EVOH as compatibilizer) are much higher overall compared to a clean HiPP sample. The Young's modulus clearly becomes worse as the EVOH loadings are increased within the nanocomposite. This is caused by the poor distribution and interaction of the EVOH and chnw in the HiPP matrix.

6.3.2 Electrospinning and meltpressing

SEM images shows good fibers for electrospinning solutions consisting of 3 wt% chnw and 5 wt% EVOH. Beading can be caused by an increase in the humidity that cause the EVOH electrospinning solution to agglomerate on the collector base. The increasing viscosity of the electrospinning solution caused problems with the fiber formation. The infrared peak for the individual compounds can be detected using FTIR. The peaks of chnw, HiPP and EVOH within the nanocomposites appear to overlap creating some difficulty in identifying peaks after the incorporation of the electrospun fiber mat into the HiPP matrix. The chnw improves the overall thermal stability of EVOH slightly as seen in the TGA thermograms for the nanofibers. Once the fiber mats were incorporated into HiPP, a larger shift in the onset of degradation temperature could be seen for the TGA thermograms of the nanocomposites. The Young's modulus showed greater improvement for the nanocomposites containing electrospun fibermats. Effective dispersion within the electrospun fiber mat was accomplished during electrospinning for low chnw loadings.

References

- [1] Y. Lu, L. Weng, and L. Zhang, "Morphology and properties of soy protein isolate thermoplastics reinforced with chitin whiskers," *Biomacromolecules*, vol. 5, pp. 1046–1051, 2004.
- [2] M. Rinaudo, *Progress in Polymer Science*, 2006.
- [3] M. Du Toit, "Incorporation of polysaccharide nanowhiskers into a poly (ethylene-co-vinyl alcohol) matrix," p. 1, 2013.
- [4] H. Mahdavi and M. Nook, "Structure and morphology of a commercial high-impact polypropylene in-reactor alloy synthesized using a spherical ziegler-natta catalyst." *Polymer International*, vol. 59, pp. 1701–1708, 2010.
- [5] J. Karger-Kocsis, *Polypropylene structure, blends and composites: Structure and morphology*, 1st ed. Chapman and Hall, vol. 1.
- [6] M. Dezhu, L. Xiqiang, Z. Ruiyun, H. Kunlun, and L. Xiaolie, "Characteristics of structure of impact polypropylene copolymers of propylene with low ethylene contents," *Chinese Journal of Polymer Science*, vol. 12(2), pp. 169–170, 1994.
- [7] H. Jiang, J. He, J. Liu, and Y. Yang, "Synthesis and characterization of poly(ethylene-co-vinyl alcohol)-graft-poly(caprolactone)," *Polymer Journal*, vol. 34(9), pp. 682–686, 2002.
- [8] A. Mejia, F. Segura, and C. Arboleda, "Enzymatic transformation of crystalline structure of copolymer poly(ethylene-co-vinyl alcohol) (evoh)," *Vitae*, vol. 14(1), pp. 25–30, 2007.
- [9] C. Arboleda, A. Mejia, and B. Lopez, "Poly(vinyl alcohol-co-ethylene) biodegradation on semi solid fermentation by *Phanerochaete chrysosporium*," *Acta Farmacológica Bonaerense*, vol. 23(2), pp. 123–128, 2004.
- [10] N. Basson, "The effect of molecular architecture on the properties of propylene impact copolymers." *University of Stellenbosch*, pp. 13–23, 2010.

- [11] V. Alvarez, R. Ruseckaite, and A. Vasquez, “Kinetic analysis of thermal degradation in poly(ethylene-vinyl alcohol)copolymers.” *Journal Applied Polymer Science*, vol. 90, pp. 3157–3163, 2002.
- [12] S. Ramakrishna, K. Fujihara, T. Wee-Eong, L. Teik-Cheng, and Z. Ma, “An introduction to electrospinning and nanofibers,” *World scientific Publishing Co. Pte. Ltd*, pp. 114–116, 2005.
- [13] R. Armstrong, “New eval® evoh resin for flexible packaging,” *EVAL Americas (USA)*.

Chapter 7

Conclusions and Recommendations for Future Work

7.1 Conclusion

The results found for the tensile properties of the nanocomposites containing PPgMA as compatibilizer are consistent with that found in literature studies. HiPP matrix containing chnw as a filler alone is not effective enough to improve any mechanical properties of the nanocomposites as a whole. A compatibilizer is needed for better interaction between the filler and the matrix. PPgMA was chosen to be a very good compatibilizer for chnw and HiPP. The tensile properties of the nanocomposites are greatly improved. The maximum tensile stress of all the nanocomposites containing chnw with compatibilizer is higher than a clean sample of HiPP. The Young's modulus for the nanocomposites containing PPgMA are also higher than a clean sample of HiPP. The optimum for this appears to be 3%chnw_10%PPgMA and 10%chnw_2%PPgMA due to better interaction and less agglomeration of the chnw. The thermal properties such as melting temperature and percentage crystallization of the nanocomposites remain mostly the same compared to a clean HiPP sample. The onset of degradation temperature belonging to the nanocomposites seems slightly higher than that for a clean sample of HiPP.

The nanocomposites with EVOH as a compatibilizer showed no improvement of the tensile properties and only the maximum tensile strength of the composite increased. The elongation at break for the nanocomposite containing EVOH as compatibilizer was slightly more than that for the nanocomposite with PPgMA as compatibilizer. This ductility indicated that the crystallinity of the nanocomposite was not greatly improved which proves that there was poor interaction between the chnw and HiPP matrix. The Young's modulus and thermal stability were slightly more enhanced when the EVOH was incorporated as a compatibilizer into the HiPP matrix via electrospinning along with the chnw. The dispersion of the chnw with low loadings were favorable and presented

improved tensile properties.

7.2 Future work

The study could be expanded to incorporate other impact copolymers. Dynamic mechanical analysis can be used to investigate the storage modulus and other mechanical properties of the nanocomposites in future studies. The effect that the presence of chnw within the HiPP matrix have on the biodegradability of the nanocomposite should also be investigated. It has been mentioned that EVOH is commonly used in film packaging industry for its barrier properties. The nanocomposites containing EVOH/chnw electron fibers can therefore be investigated for water absorption and gas permeability in future work. Measuring the viscosity of the increase in PPgMA or chnw content in solution is a good idea in order to investigate how this also can effect the distribution of chnw within the HiPP matrix.

Appendix A

FTIR data

A.1 FTIR spectra of nanocomposites containing EVOH as compatibilizer

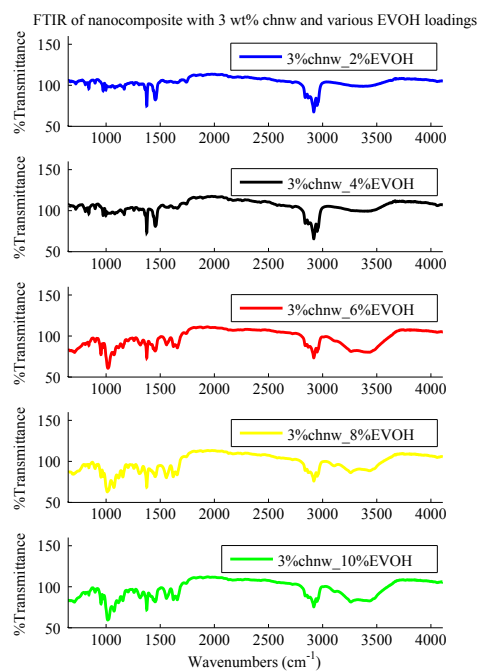


Figure A.1: FTIR spectra of 3 wt% chnw and varying EVOH.

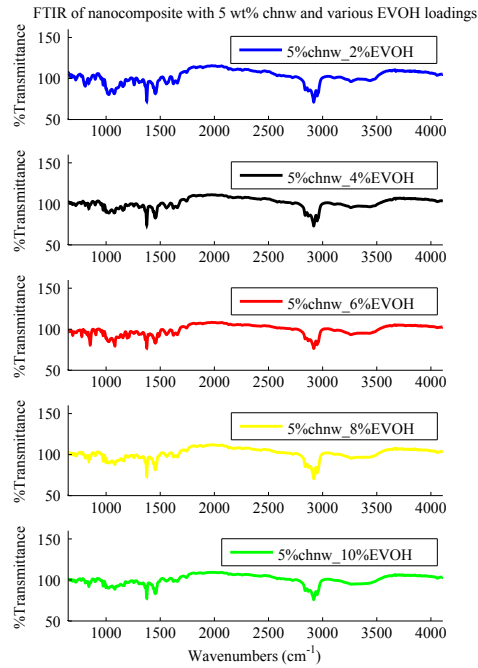


Figure A.2: FTIR spectra of 5 wt% chnw and varying EVOH.

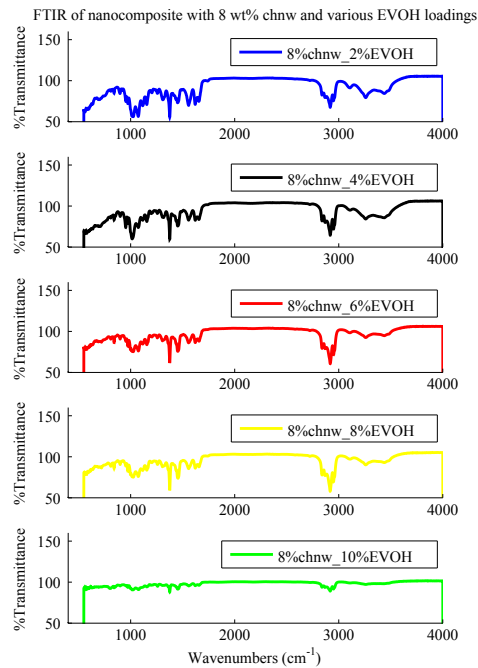


Figure A.3: FTIR spectra of 8 wt% chnw and varying EVOH.

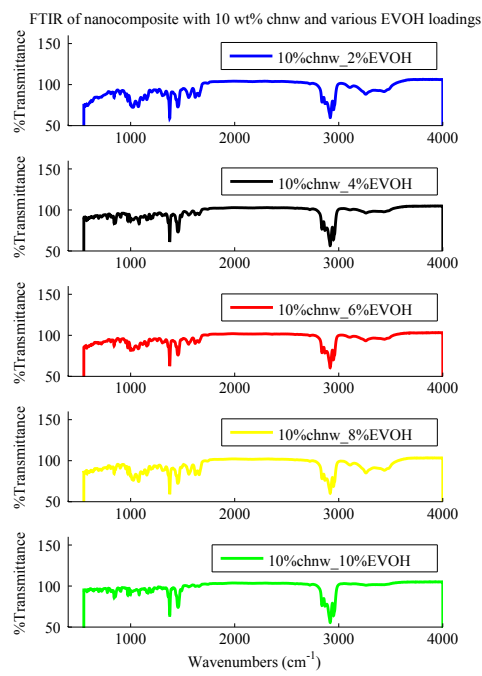


Figure A.4: FTIR spectra of 10 wt% chnw and varying EVOH.

Appendix B

DSC Data

B.1 DSC results for HiPP/chnw nanocomposites with PPgMA as compatibilizer

The changes that was illustrated in 2.9 the Tables 5.1 and 5.2 for the nanocomposites containing various loadings of PPgMA and chnw are also presented in Figure B.1 to B.5. The peaks crystallization percentage shows a significant shifting compared to the peaks for a clean HiPP sample as can be seen in all the DSC thermograms. The melting temperature peaks remains relatively the same for the nanocomposites compared to a clean HiPP sample.

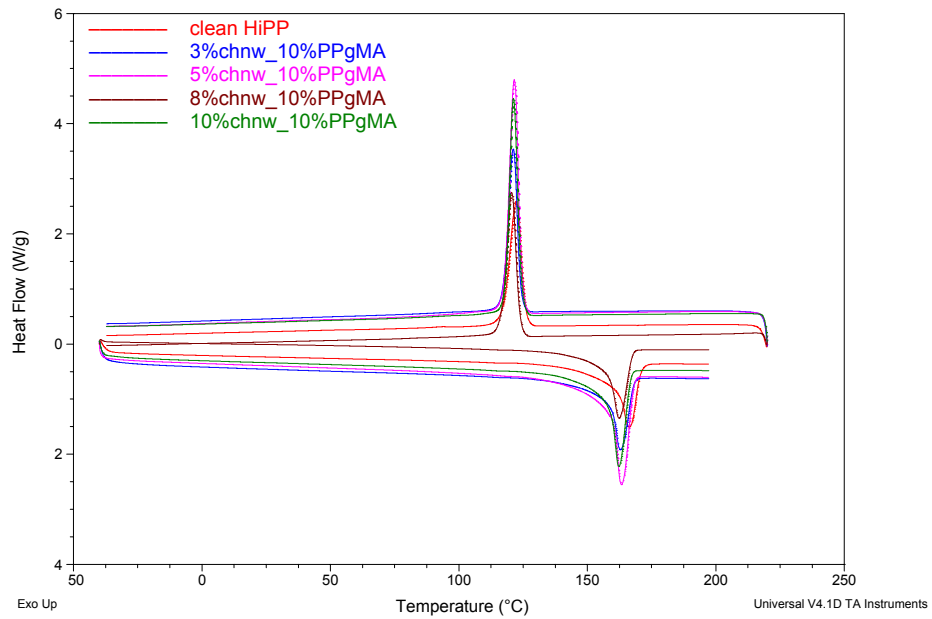


Figure B.1: DSC thermograms showing the effect that 10 wt% PPgMA and various wt% chnw have on the HiPP matrix.

A general increase in the crystallization peak seen in the figures presented above shows that a increase in chnw combined with a low loading of PPgMA can enhance crystallinity within the composite. The same can be seen for low chnw loading and higher loadings of PPgMA.

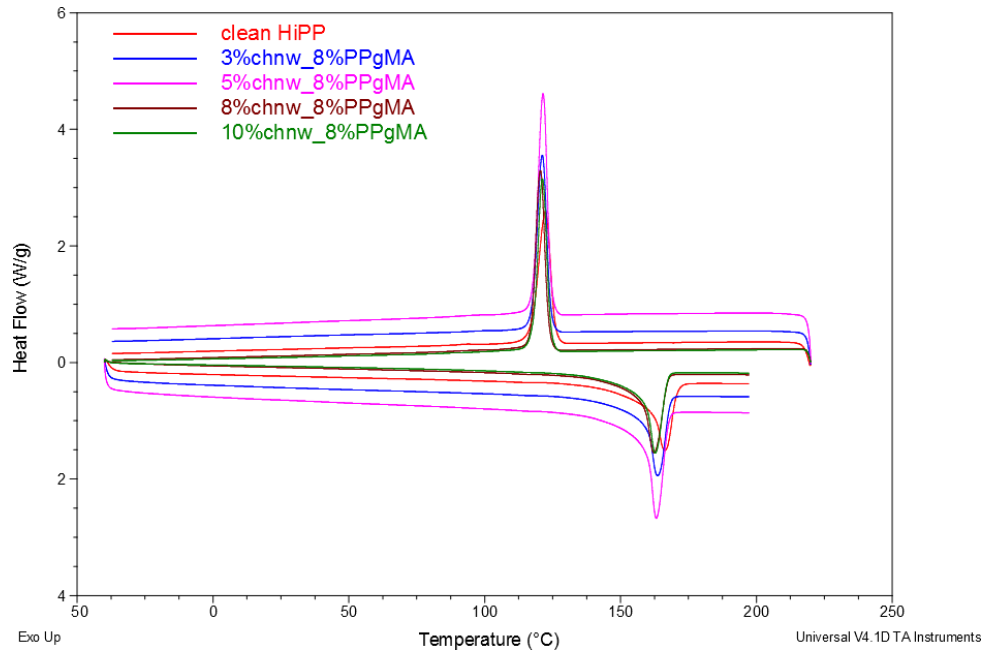


Figure B.2: DSC thermograms showing the effect that 8 wt% PPgMA and various wt% chnw have on the HiPP matrix.

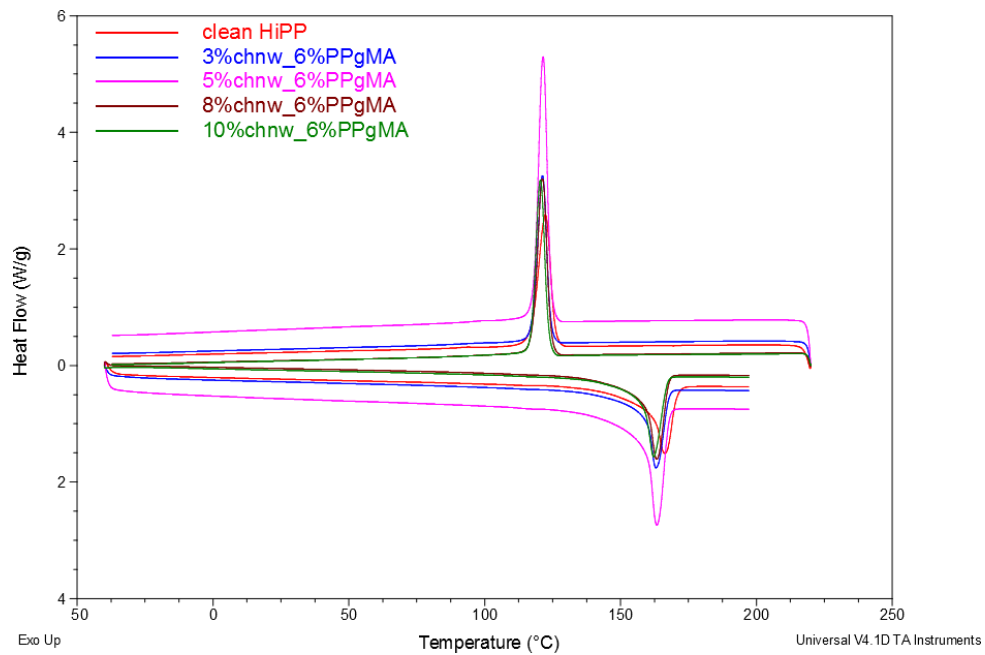


Figure B.3: DSC thermograms showing the effect that 6 wt% PPgMA and various wt% chnw have on the HiPP matrix.

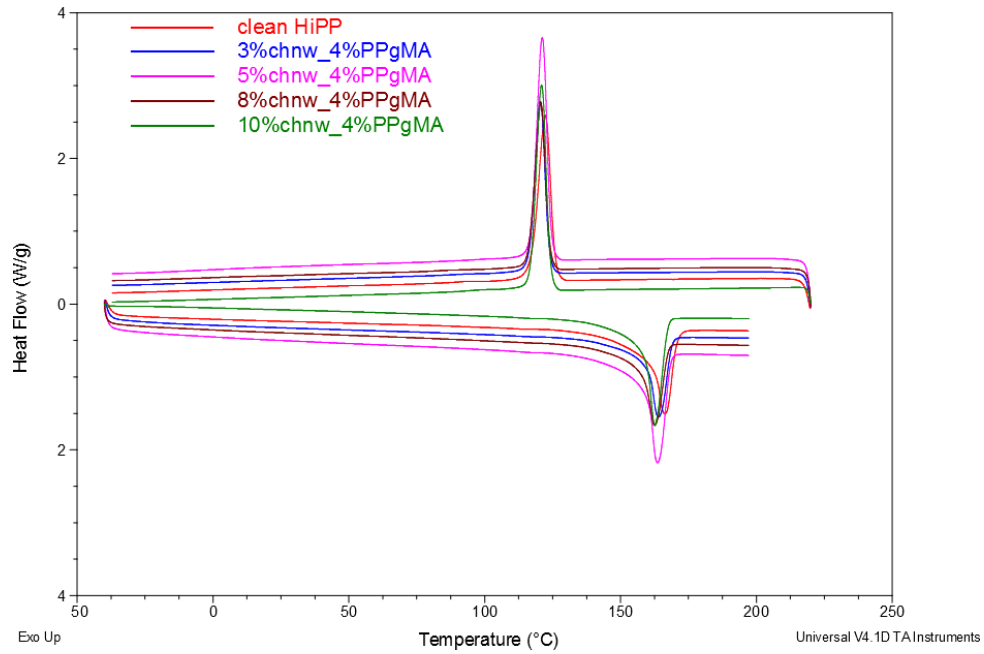


Figure B.4: DSC thermograms showing the effect that 4 wt% PPgMA and various wt% chnw have on the HiPP matrix.

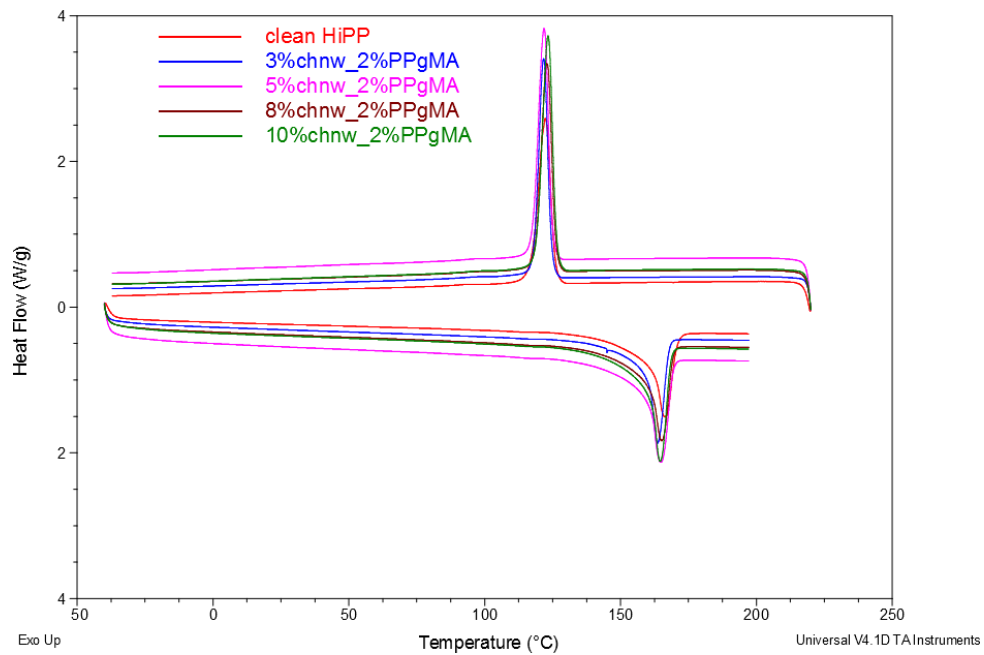


Figure B.5: DSC thermograms showing the effect that 2 wt% PPgMA and various wt% chnw have on the HiPP matrix.

Appendix C

SEM images of nanocomposites

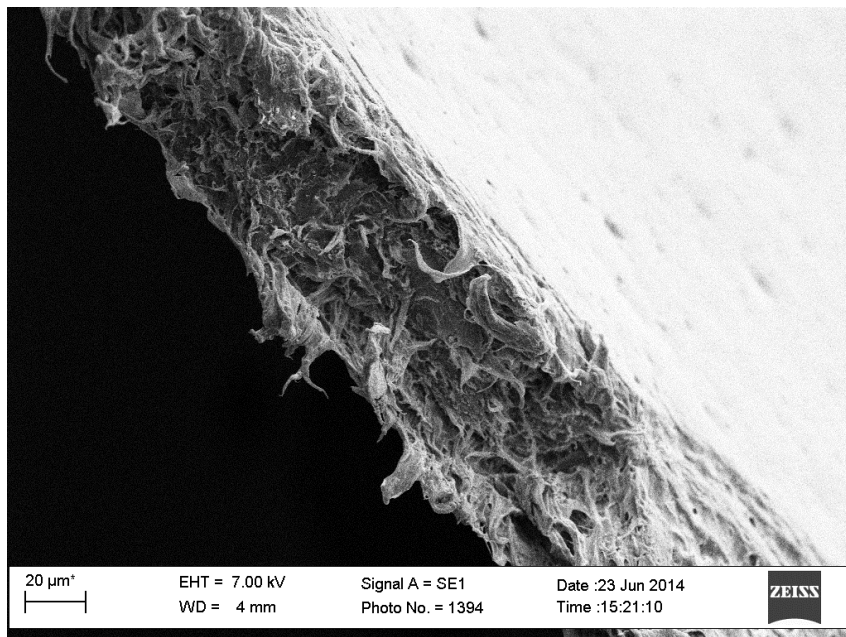


Figure C.1: SEM images of 5 wt% chnw and 5 wt% EVOH indicating the layers of HiPP with electrospun chnw_EVOH fiber mat.

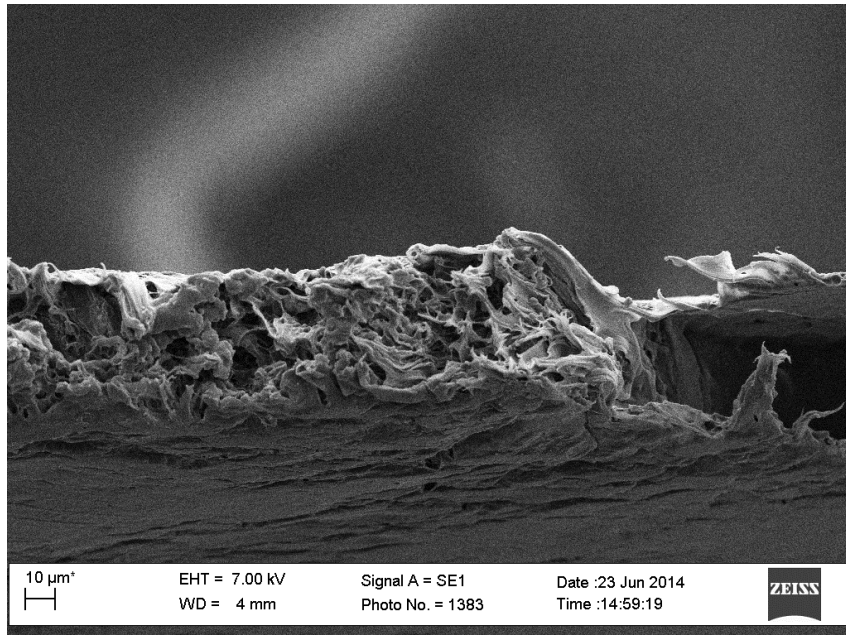


Figure C.2: SEM images of 8 wt% chnw and 5 wt % EVOH in HiPP.

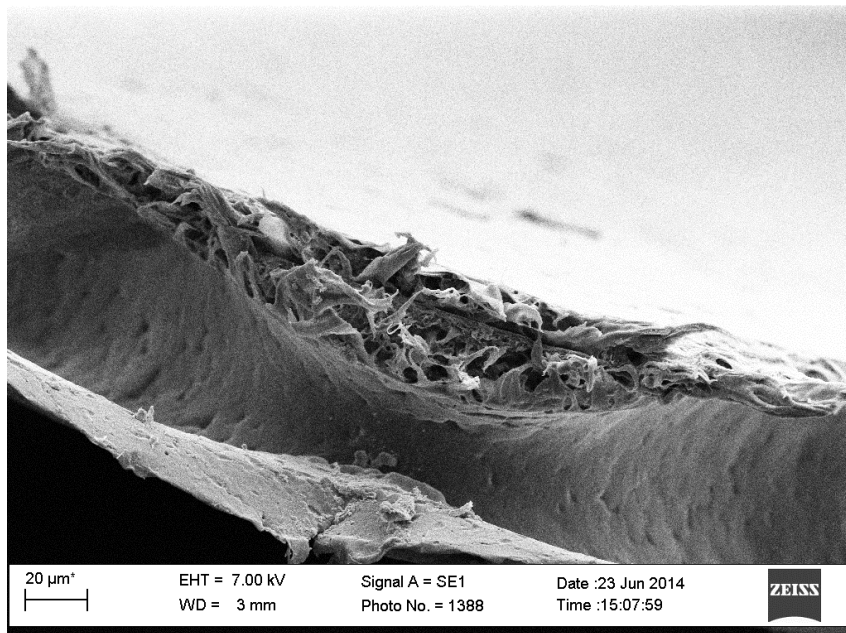


Figure C.3: SEM images of 10 wt% chnw and 2 wt% EVOH in HiPP.